

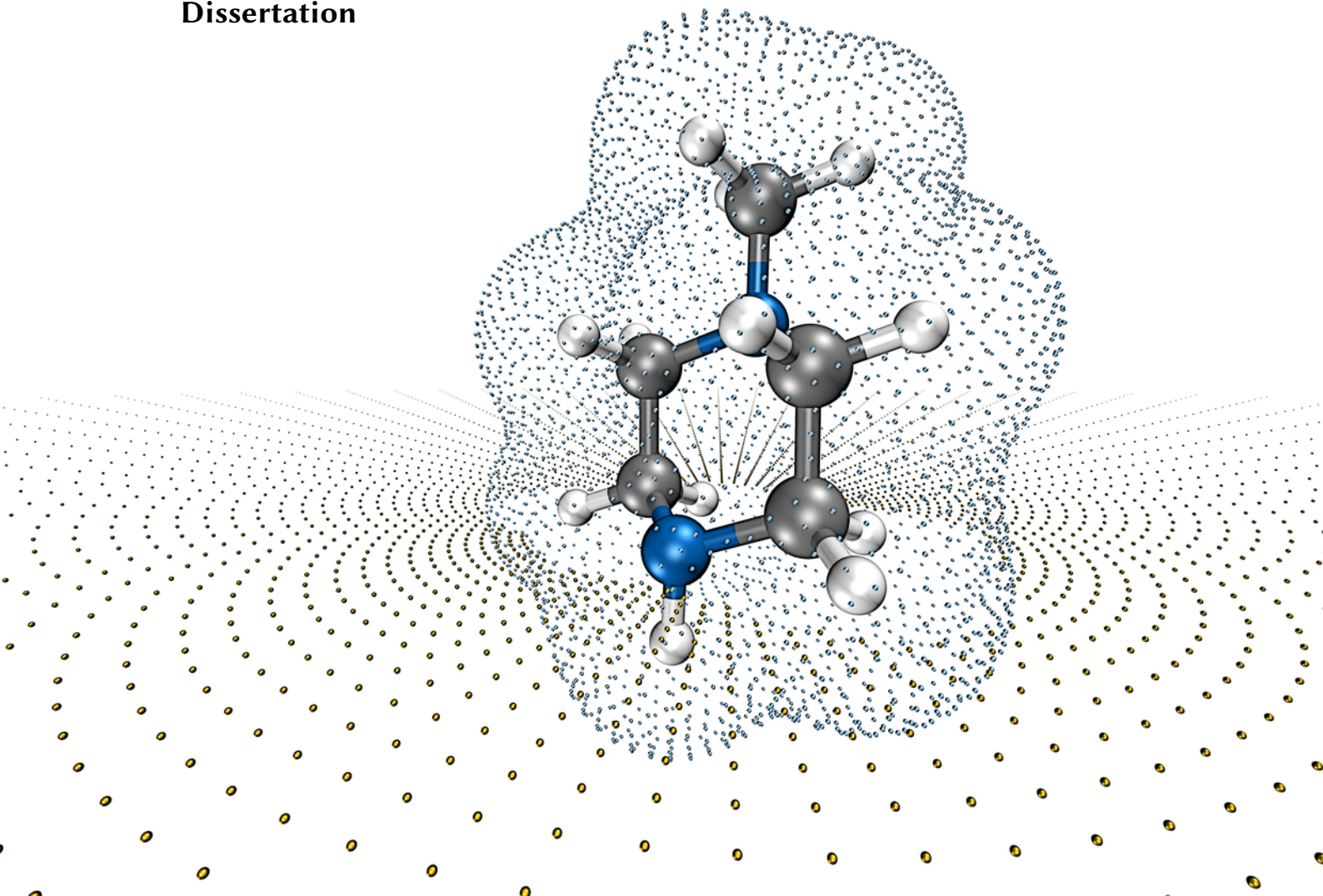


**Technische Universität München**  
Fakultät für Chemie  
Lehrstuhl für Theoretische Chemie

# Multipole Expansion Implicit Solvation Model in Full Potential DFT

**Markus Sinstein**

**Dissertation**





**Technische Universität München**  
Fakultät für Chemie  
Lehrstuhl für Theoretische Chemie

---

# **Multipole Expansion Implicit Solvation Model in Full Potential DFT**

---

**Markus Sinstein**

Vollständiger Abdruck der von der  
Fakultät für Chemie der Technischen Universität München  
zur Erlangung des akademischen Grades eines

**Doktors der Naturwissenschaften (Dr. rer. nat.)**

genehmigten Dissertation.

Vorsitzender: Priv.-Doz. Dr. Friedrich Esch

Prüfer der Dissertation:

1. Prof. Dr. Karsten Reuter
2. Prof. Dr. Ville Kaila

Die Dissertation wurde am 17. Januar 2018 bei der Technischen Universität München  
eingereicht und durch die Fakultät für Chemie am 15. Februar 2018 angenommen.



THERE ARE NO CHOICES.  
NOTHING BUT A STRAIGHT LINE.

THE ILLUSION COMES AFTERWARDS,  
WHEN YOU ASK 'WHY ME?' AND 'WHAT  
IF?' WHEN YOU LOOK BACK, SEE THE  
BRANCHES, LIKE A PRUNED BONSAI  
TREE, OR A FORKED LIGHTNING.

IF YOU HAD DONE SOMETHING  
DIFFERENTLY, IT WOULDN'T BE  
YOU, IT WOULD BE SOMEONE  
ELSE LOOKING BACK, ASKING  
A DIFFERENT SET OF QUESTIONS.

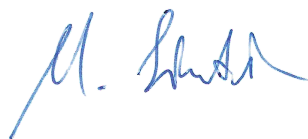
- Max Payne, *The Fall of Max Payne*



## ***Preface***

All work presented in this doctoral thesis was performed between January 2014 and December 2017 at the Chair of Theoretical Chemistry of the Technical University of Munich (TUM), under the supervision of Prof. Dr. Karsten Reuter. Research stays hosted by Prof. Dr. Volker Blum at the Department of Mechanical Engineering and Materials Science at Duke University complemented the work performed locally at TUM. Parts of this dissertation have been published before in Ref. [1].

Ismaning, January 2018

A handwritten signature in blue ink, appearing to read 'M. Schuster', is written in a cursive style.



## **Abstract**

The development of efficient numerical algorithms and the rapidly increasing availability of computational power over the last decades has fueled the development of more accurate electronic structure methods and allowed the simulation of steadily growing model systems. This continuously leads to the invention of new methods and approaches. Furthermore, aspects that have previously been neglected or extremely simplified due to a lack of appropriate computational methods need to be re-evaluated periodically and, when found to be treated with insufficient accuracy, improved. A prominent example of such an aspect is the effect of a solvent on a solute and its reactivity. For this purpose, implicit solvation models were introduced a century ago to calculate the hydration energy of ions and dipoles in spherical symmetry. With solvent effects being central to several scientific disciplines like biology or (electro-)chemistry, it is not surprising that especially those models have received countless revisions and extensions over time.

Even nowadays when an explicit modeling of the solute including a large part of the surrounding is within reach, implicit solvation methods do not yet suffer the loss of popularity, quite the contrary. This is attributed on the one hand to the rather involved and computationally expensive thermodynamical sampling of the solvent's vast phase space, and on the other hand to many unresolved issues concerning shortcomings of most current theoretical methods in the prediction of physical properties of liquid water. As an alternative, modern continuum solvation models emerged that allow for a direct coupling to the quantum mechanical description of the solute, usually *via* the introduction of an additional external potential, commonly referred to as the reaction field. One of those is the multipole expansion (MPE) model which offers a particularly cheap way of determining the reaction field in electronic structure calculations given an efficient evaluation method for the electrostatic potential *in vacuo* at arbitrary points in real space. Employing an iso-surface definition of the solvation cavity, this model furthermore reaches a minimal number of free parameters which makes it perfectly suited for an implementation into the *ab-initio* all-electron, localized numerical atomic orbital electronic structure code FHI-aims.

In this work, we elucidate the theoretical foundations of modern continuum solvation methods. The existing homogeneous MPE model is recast into a completely outlying charge error-free formulation and an efficient way of solving the resulting equations relying on well-established linear algebra methods is illustrated. We describe novel algorithms for finding equi-distributed points on the solvation cavity and for calculating the cavity's surface area and volume from just this collection of points and their local density gradients. The efficacy of the developed methods is demonstrated through comparison to analytically solvable test-cases, high-accuracy finite element calculations for a set of around 140000 2D model systems, and experimental solvation free energies of a number of neutral and singly charged molecular test-sets. In all test-cases very good agreement is found with the corresponding references. For the molecular test systems, computational overheads of the (not yet fully optimized) MPE approach of less or sometimes much less than 20% compared to the corresponding plain self-consistency cycle are observed, underlining the computational efficiency of the method. Finally, a novel heterogeneous MPE model is developed which, in model setups, reaches again very good agreement with analytical and finite element calculations.





## **Zusammenfassung**

Über die letzten Jahrzehnte beschleunigten die Entwicklung effizienter numerischer Methoden und der rapide Anstieg an verfügbarer Rechenleistung die Entwicklung exakterer Elektronenstrukturmethoden in besonderem Maße. Neben der Erfindung neuer Ansätze werden auch bestehende Methoden stetig verbessert, wenn sich die darin bisher getroffenen Approximationen als unzureichend herausstellen. Aufgrund der Relevanz von Lösungsmittelleffekten in vielen Bereichen der Wissenschaft, z. B. Biologie oder Elektrochemie, überrascht es nicht, dass die zu diesem Zweck etablierten und zum Teil bereits rund einhundert Jahre alten theoretischen Methoden unzählige Male weiterentwickelt wurden. Selbst in der heutigen Zeit, in der die atomistische Modellierung des gesamten Solvats zum Greifen nahe ist, verlieren Kontinuumseinbettungsmethoden nicht an Beliebtheit. Eher das Gegenteil trifft zu. Verantwortlich dafür ist zum einen die aufwändige thermodynamische Integration über den riesigen Phasenraum der Lösungsmittelmoleküle. Zum anderen weisen die meisten bestehenden theoretischen Methoden zahlreiche Defizite auf, was ihre Vorhersagekraft zu physikalischen Eigenschaften von flüssigem Wasser betrifft.

Als Alternative wurden moderne Kontinuumseinbettungsmethoden entwickelt, die den Einfluss des Lösungsmittels indirekt durch die Einführung eines externen, elektrostatischen Potentials beschreiben, welches üblicherweise Reaktionsfeld genannt wird. Zu diesen Methoden gehört auch der Multipolentwicklungsansatz (MPE), der durch seine geringe Anzahl an Modellparametern, insbesondere in der hier gewählten Kombination mit einer Isofläche der Dichte als Grenzfläche zwischen gelöstem Stoff und Solvent, und seinen geringen Rechenaufwand heraussticht. Letzteres setzt dabei eine effiziente Auswertbarkeit des elektrostatischen Vakuumpotentials an beliebigen Punkten im Raum voraus. Aufgrund dieser Vorteile eignet sich der MPE-Ansatz ideal als Erweiterung zum Ab-initio-Elektronenstrukturprogramm FHI-aims.

In dieser Arbeit wird, nach Erarbeitung der theoretischen Grundlagen moderner Kontinuumseinbettungsmethoden, der bereits bestehende MPE-Ansatz derart überarbeitet, dass sich keinerlei Berechnungsfehler durch die Ausdehnung der Elektronendichte des gelösten Stoffes in das Solvent hinein ergeben. Des Weiteren wird die Anwendung von gängigen Methoden der numerischen linearen Algebra zur Lösung der resultierenden Gleichungen aufgezeigt. Wir stellen neuartige Algorithmen sowohl zur Bestimmung gleichverteilter Punkte auf der Grenzfläche zum Solvent, mit den jeweils zugehörigen Normalenvektoren, als auch zur Oberflächen- und Volumenberechnung dieser Punktwolke vor. Die Verifizierung des gesamten Modells erfolgt durch den Vergleich mit analytischen Lösungen für einfache Testmodelle, mit Ergebnissen einer hochgenauen Methode der finiten Elemente für rund 140000 zweidimensionale Modellsysteme und mit experimentellen Daten zur freien Lösungsenthalpie von neutralen und einfach geladenen, kleinen, organischen Molekülen. In allen Fällen ist eine sehr gute Übereinstimmung zu erkennen. Der Mehraufwand der (noch nicht vollständig optimierten) Methode, im Verhältnis zu einer einfachen Simulation im Vakuum, beläuft sich für die oben genannten organischen Moleküle auf (in vielen Fällen deutlich) weniger als 20%, was nochmals die Effizienz der Methode in Bezug auf den Rechenaufwand unterstreicht. Abschließend stellen wir die Entwicklung eines neuartigen, inhomogenen MPE-Ansatzes vor, der für Modellsysteme wiederum sehr gute Übereinstimmungen mit analytischen Berechnungen und Methoden der finiten Elemente liefert.



# Contents

---

|          |   |           |
|----------|---|-----------|
| <b>1</b> | <b>Introduction</b>   | <b>1</b>  |
| <b>2</b> | <b>Quantum Mechanics</b>  | <b>5</b>  |
| 2.1      | Schrödinger Equation and Born-Oppenheimer Approximation . . . . . | 5         |
| 2.2      | Variational Principle . . . . .                                   | 6         |
| 2.3      | Hartree-Fock Approximation . . . . .                              | 6         |
| 2.4      | Density Functional Theory . . . . .                               | 8         |
| 2.4.1    | Hohenberg-Kohn Theorems . . . . .                                 | 8         |
| 2.4.2    | Kohn-Sham Approach . . . . .                                      | 8         |
| 2.4.3    | Exchange-Correlation Functional Approximations . . . . .          | 9         |
| <b>3</b> | <b>Basic Ingredients for Implicit Solvation</b>                   | <b>11</b> |
| 3.1      | Electrostatic Model . . . . .                                     | 12        |
| 3.1.1    | Vacuum Electrostatic Potential . . . . .                          | 12        |
| 3.1.2    | Electrostatic Potential of the Solvated System . . . . .          | 12        |
| 3.1.3    | Electrostatic Energy . . . . .                                    | 14        |
| 3.2      | Model for the Dielectric Function . . . . .                       | 15        |
| 3.3      | Solution Approaches to the Electrostatic Model . . . . .          | 16        |
| 3.3.1    | Generalized Born Approach . . . . .                               | 17        |
| 3.3.2    | Apparent Surface Charge Method . . . . .                          | 18        |
| 3.3.3    | Multipole Expansion Model . . . . .                               | 20        |
| 3.4      | Non-Electrostatic Interactions . . . . .                          | 22        |
| 3.5      | Cavity Definition . . . . .                                       | 23        |
| <b>4</b> | <b>MPE Method</b>   | <b>27</b> |
| 4.1      | Discretization of the MPE Equations . . . . .                     | 27        |
| 4.1.1    | Truncated Multipole Expansion . . . . .                           | 27        |
| 4.1.2    | Cavity Discretization . . . . .                                   | 28        |
| 4.2      | Formulation as Linear Algebra Problem . . . . .                   | 32        |
| 4.2.1    | Matrix Factorization and Solution . . . . .                       | 33        |
| 4.2.2    | Solver Memory . . . . .   | 36        |
| 4.2.3    | Improving the Matrix Conditioning . . . . .                       | 36        |
| 4.3      | Benchmark Systems . . . . .                                       | 40        |
| 4.3.1    | Born Equation . . . . .   | 40        |
| 4.3.2    | 2D Model Systems: Comparison to FEM . . . . .                     | 40        |
| 4.4      | A Note on Previous MPE Models . . . . .                           | 45        |
| 4.4.1    | Hartree Potential Expansion . . . . .                             | 45        |
| 4.4.2    | Probe Charge Approach . . . . .                                   | 46        |
| 4.4.3    | Comparison to the Direct Approach . . . . .                       | 49        |

|          |   |            |
|----------|---|------------|
| <b>5</b> | <b><i>Isodensity Cavity Generation</i></b>                      | <b>51</b>  |
| 5.1      | Density-Walker Initialization . . . . .                         | 51         |
| 5.1.1    | Atomic Spherical Grids . . . . .                                | 52         |
| 5.1.2    | Overlapping the Atomic Spheres . . . . .                        | 53         |
| 5.2      | Walker Dynamics Simulation . . . . .                            | 55         |
| 5.2.1    | Forces . . . . .  | 55         |
| 5.2.2    | Walker Propagation . . . . .                                    | 56         |
| 5.2.3    | Walker Elimination and Neighbor Lists . . . . .                 | 58         |
| 5.2.4    | Parameters . . . . .  | 58         |
| 5.3      | Which Density? . . . . .  | 58         |
| 5.4      | Calculation of Surface Area and Volume . . . . .                | 59         |
| 5.4.1    | Local Coordinate System . . . . .                               | 60         |
| 5.4.2    | Voronoi Construction in Local Projection . . . . .              | 60         |
| 5.4.3    | Calculation of Area and Volume Elements . . . . .               | 62         |
| <b>6</b> | <b><i>MPE Model Parametrization</i></b>                         | <b>65</b>  |
| 6.1      | Test Sets . . . . .   | 65         |
| 6.2      | Fitting Procedure . . . . .                                     | 66         |
| 6.3      | Computational Details . . . . .                                 | 67         |
| 6.4      | Parametrization Results . . . . .                               | 67         |
| 6.4.1    | Cavity from Converged Vacuum Density . . . . .                  | 68         |
| 6.4.2    | Cavity from Superposition of Free Atom Densities . . . . .      | 72         |
| 6.5      | Complementary Statistical Analysis . . . . .                    | 76         |
| 6.6      | Timings . . . . .   | 78         |
| <b>7</b> | <b><i>Outlook: Extension to Two Dielectrics</i></b>             | <b>81</b>  |
| 7.1      | Definition of the Planar Interface . . . . .                    | 81         |
| 7.1.1    | Image Charge Ansatz for a Single Monopole . . . . .             | 82         |
| 7.1.2    | Return to Multipole Expansion . . . . .                         | 82         |
| 7.1.3    | Comparison to FEM for Higher Order Multipoles . . . . .         | 84         |
| 7.2      | Combination of Solvation Cavity with Planar Interface . . . . . | 86         |
| 7.2.1    | Multipole Expansion of Potentials . . . . .                     | 87         |
| 7.2.2    | Discretization of the Interfaces . . . . .                      | 87         |
| 7.2.3    | MPE Equations . . . . .   | 88         |
| 7.2.4    | Heterogeneous 2D Model Systems: Comparison to FEM . . . . .     | 88         |
| 7.2.5    | Final Remarks . . . . .   | 90         |
| <b>8</b> | <b><i>Conclusion</i></b>  | <b>93</b>  |
|          | <b><i>Acknowledgments / Danksagung</i></b>                      | <b>97</b>  |
|          | <b><i>Bibliography</i></b>                                      | <b>99</b>  |
|          | <b><i>Appendices</i></b>  | <b>103</b> |

# *List of Abbreviations*

---

- FHI-aims** Fritz Haber Institute *ab initio* molecular simulation
- ASC** apparent surface charge
- ASD** apparent surface dipole
- COSMO** conductor-like screening model
- DFT** density functional theory
- FEM** finite element method
- GB** generalized Born
- GGA** generalized gradient approximation
- HF** Hartree-Fock
- HK** Hohenberg-Kohn
- IEF** integral equation formalism
- KS** Kohn-Sham
- LAPACK** Linear Algebra Package
- LDA** local density approximation
- LL** Lebedev-Laikov
- MAE** mean absolute error
- MPE** multipole expansion
- PBE** Perdew, Burke and Ernzerhof
- PCM** polarizable continuum model
- QM** quantum mechanics
- RMSD** root-mean-square deviation
- SAS** solvent-accessible surface
- ScaLAPACK** Scalable Linear Algebra Package (LAPACK)
- SCAN** strongly constrained and appropriately normed (semilocal density functional)

**SCF** self-consistent field

**SES** solvent-excluded surface

**SLE** system of linear equations

**SPANC** solvation parameters for neutrals and cations

**SS(V)PE** surface and simulation of volume polarization for electrostatics

**SVD** singular value decomposition

**vdW** van der Waals

# 1 Introduction

---

Since the early days of alchemical experiments, chemical reactions have mostly been studied in solution. From a synthetic point of view, the fact that the solvent can severely alter the outcome of a reaction has long been recognized. Thus, in the search for the optimal reaction conditions, the choice of solvent is often considered as important as other parameters such as reactant combinations and concentrations, temperature, or pressure. In biology, the structures of enzymes that drive most processes of life are very sensitive to the aqueous environment and ions concentrations therein. Also in the emerging field of renewable energies, water plays a central role as a byproduct in the energy production of fuel cells or as a starting material for electro- or photolytic hydrogen production. These examples illustrate that theoretical studies of such processes—which can, e.g., help to identify the involved reaction mechanism—have to include the environment surrounding the reactants, i.e., the solvent, a fact that is more and more recognised in the community [2].

The computational modeling of a liquid phase, however, is challenging. First, the solvent contributes a large number of molecules to the simulation. This increase in system size may already prohibit a treatment with highly accurate quantum mechanical (QM) methods due to their unfavorable scaling, such as e.g.  $\mathcal{O}(N^7)$  for coupled cluster calculations with explicit single and double, and a perturbative treatment of triple excitations.

like coupled cluster calculations. Therefore, one usually resorts to methods that are, generally speaking, more approximate but less expensive such as density functional theory (DFT) in combination with one of the many functional approximation flavors [3–6] or, even one step further, classical force field methods [7]. While the latter have certainly demonstrated their usefulness in the description of the solvent bulk [8], we want to focus in this work on the solute and its QM description for which we introduce the central concepts in chapter 2. It is noteworthy here that in the case of liquid water, most otherwise established theoretical approaches fail to predict its physical properties. For example, it is a well known shortcoming of the DFT generalized gradient approximation (GGA) functional family to largely overestimate the melting temperature of ice [9]. Furthermore, most DFT studies wrongly predict ice to be denser than water—an issue which only the most recent advances in DFT seem to rectify [10] using the strongly constrained and appropriately normed (SCAN) semilocal density functional [11].

The second challenge arises due to the inherent structural disorder in the liquid phase which requires a statistical sampling of the solvent’s phase space in order to obtain thermodynamically meaningful observables. Due to the enormous amount of possible configurations, converging this sampling can become very hard or even unfeasible. Commonly, two different routes are taken to cut down the computational cost. One way is to treat the solvent on a molecular-mechanics level coupled to a QM core region, thus making the necessary sampling more affordable. This so-called QM/MM approach has been successfully applied not only for the embedding in a solvent [12–14]. It is, however, frequently fraught with boundary errors and numerical problems [15]. Another way is to completely circumvent the statistical averaging by replacing all explicit interactions between solute and solvent with a simple (electrostatic) response function. While the former is then still



treated explicitly at an atomistic level of detail, the latter is modeled as a polarizable continuum characterized solely by its dielectric permittivity function. One can think of this function in a way that it contains the essence of the thermodynamic integration in the solvent which has been conducted independently of a specific solute. Implicitly, this includes the assumption that thermodynamical equilibration between solute and solvent always happens instantaneously. The theoretical foundations of this so-called implicit or continuum solvation approach will be worked out in more detail in chapter 3. Said response function is not uniquely defined and the freedom in defining its shape has given rise to a large number of solvation models [16] of which we will only mention a few. The common pattern between those models is that, due to the exclusion of solvent molecules in the volume occupied by the solute and the self-screening of the charges in the QM zone, the relative permittivity very close to the solute equals 1, i.e. no screening, while far away from the solute the bulk value is assumed.

In the present work, we focus on a sharp, step-like transition of the permittivity function between the respective regions assigned to the solute and the solvent. This is obviously an effective model, since in nature there is no “hard boundary” of this exclusion zone—which delineates the so-called (solvation) cavity—and the dielectric response will probably show a not necessarily monotonous but rather smooth transition. The shape of this cavity therefore has to be viewed as an effective parameter to be adapted for the model to optimally agree with explicitly simulated or measured solvation results. In addition to the unavoidably introduced parameters of this purely electrostatic treatment, more come into play when correction terms are introduced to account for so far neglected effects, often called the non-electrostatic or non-mean-field contributions [16, 17]. Following an otherwise *ab initio* approach, a key requirement in our search for a suitable solvation model was to keep the number of such parameters as low and the parameters themselves as transferable as possible [18]. Therefore, we based our approach on the multipole expansion (MPE) model [19, 20], which we recast into a novel, completely outlying-charge-error free formulation, and a simple non-electrostatic post-correction [21].

The decision to pick the MPE approach as the object of study here was heavily influenced by certain features of the code it should extend, namely the Fritz Haber Institute *ab initio* molecular simulation (FHI-aims) package [22]. The latter is an all-electron, full potential electronic structure code which relies on localized, numeric atom-centered basis sets and non-uniform, overlapping integration grids for DFT [23] as well as higher level calculations [24, 25]. Specifically, our implementation relies on—and heavily exploits—its efficient representation and evaluation of the Hartree potential as a splined multi-center, multipole expansion. Although we concentrate in this work on our implementation in FHI-aims and DFT, it should be noted already here that all algorithms presented in this work can straightforwardly be adapted to other electronic structure methods and codes, as long as those allow a direct access to the Hartree potential in real space.

Subsequently, chapter 4 is centered thematically around the numerical realization of the improved MPE model, i.e., the discretization of its central equations on the solvation cavity and their solution *via* efficient linear algebra methods.

In chapter 5, novel methods of creating the solvent cavity and measuring its volume and surface area are developed. This allows us to complement the so far purely electrostatic model with an established non-electrostatic correction term [21].

Depending on the flavor of this term, the full MPE model gets by with as little as two or three parameters which we aim to optimize in chapter 6 by fitting the calculated free energies of hydration for small organic molecules to experimental data.

After a conclusion about the homogeneous MPE model in chapter 8, we present an extension

in chapter 7 to include a second dielectric medium. For apparent surface charge (ASC) models, similar approaches have already been reported [26–28] which should not be confused with so-called layered models [29, 30]. This is the first step to open up a promising field of application, namely chemical reactions at liquid-liquid (or liquid-air) interfaces, to DFT and beyond-DFT methods. For example, experimental studies recently found enhanced catalytic activity of carbon supported MoS<sub>2</sub> nanoparticles at a water-organic solvent interface [31, 32]. Although the present heterogeneous MPE model is still in a conceptual state, we can demonstrate the soundness and accuracy of the modified electrostatic approach in different model cases.



## 2 Quantum Mechanics

Although the later on introduced implicit solvation model is also applicable in classical mechanics, this work focuses on its combination with a quantum mechanics (QM) description of the solute. In order to provide a theoretical basis for our methods, we here briefly introduce some long-standing concepts of quantum chemistry—which today allow to conduct (within certain limits) accurate computations of realistic, molecular systems as a regular task. For a more extensive review, the interested reader is referred to well-known textbooks on this topic [33, 34].

### 2.1 Schrödinger Equation and Born-Oppenheimer Approximation

The starting point of most computational chemistry methods is the time-independent (and non-relativistic) Schrödinger equation,

$$\hat{H}\Psi(\{\mathbf{r}\}, \{\mathbf{R}\}) = E\Psi(\{\mathbf{r}\}, \{\mathbf{R}\}), \quad (2.1)$$

where  $\hat{H}$  is the Hamilton operator (also called Hamiltonian) and  $E$  the total energy of the system. The quantum mechanical wave-function  $\Psi$  contains all degrees of freedom of the molecular system's  $N$  electrons,  $\{\mathbf{r}\} = \mathbf{r}_1, \mathbf{r}_2, \dots, \mathbf{r}_N$ , and  $M$  nuclei,  $\{\mathbf{R}\} = \mathbf{R}_1, \mathbf{R}_2, \dots, \mathbf{R}_M$ . These degrees of freedom also enter  $\hat{H}$  which can—in the absence of magnetic or electric fields—be written as

$$\hat{H} = \underbrace{\sum_{i=1}^N \frac{-\nabla_i^2}{2}}_{\hat{T}_e} + \underbrace{\sum_{k=1}^M \frac{-\nabla_k^2}{2m_k}}_{\hat{T}_n} + \underbrace{\sum_{i=1}^N \sum_{j>i}^N \frac{1}{\|\mathbf{r}_i - \mathbf{r}_j\|_2}}_{\hat{V}_{ee}} + \underbrace{\sum_{k=1}^M \sum_{l>k}^M \frac{z_k z_l}{\|\mathbf{R}_k - \mathbf{R}_l\|_2}}_{\hat{V}_{nn}} + \underbrace{\sum_{i=1}^N \sum_{k=1}^M \frac{-z_k}{\|\mathbf{r}_i - \mathbf{R}_k\|_2}}_{\hat{V}_{ne}}, \quad (2.2)$$

where  $\nabla$  is the Del operator and  $\|\cdot\|_2$  denotes the  $l^2$ -norm. Note that in the atomic unit system (with Gaussian units for electromagnetism) used here, mass  $m$  and charge  $z$  of the nuclei are referenced to the electron's mass and charge. In the above equation, the decomposition of the total Hamiltonian into kinetic ( $\hat{T}$ ) and potential ( $\hat{V}$ ) energy operators is already indicated. Thereby,  $\hat{T}_e$  describes the kinetic energy of the electrons and  $\hat{T}_n$  that of the nuclei. The potential energy consists of Coulomb interactions between pairs of electrons ( $\hat{V}_{ee}$ ), pairs of nuclei ( $\hat{V}_{nn}$ ), and between electrons and nuclei ( $\hat{V}_{ne}$ ).

In many cases, electron and nuclear motions occur on very different time-scales such that in the adiabatic Born-Oppenheimer approximation the nuclei appear static from the point of view of the electrons. This reduces the nuclear degrees of freedom to mere parameters of the electronic wave-function  $\Psi(\{\mathbf{r}\}; \{\mathbf{R}\})$  and Hamiltonian,

$$\hat{H}_e = \hat{T}_e + \hat{V}_{ee} + \hat{V}_{ne}, \quad (2.3)$$

where the latter no longer contains the kinetic energy of the nuclei  $\hat{T}_n$  nor the internuclear repulsion  $\hat{V}_{nn}$  since both are constant terms.

## 2.2 Variational Principle

The only practical strategy to solve Eq. (2.1) stems from the so-called variational principle which states that—for a given Hamiltonian—the ground state wave-function  $\Psi_0$  is the one that yields the lowest total energy  $E_0$ . This means that one can vary a (normalized) test wave-function  $\Psi_{\text{test}}$  such that the total energy is minimized in order to find the true ground state wave-function.

$$E_0 = \min_{\Psi_{\text{test}}} \langle \Psi_{\text{test}} | \hat{H} | \Psi_{\text{test}} \rangle \quad (2.4)$$

The equality in the above equation, however, is only fulfilled when the ground state wave-function is included in the search space of the test wave-function. Obviously, it is not feasible to test all possible functions and therefore this is probably not the case. In reality, the search space will be restricted to functions for which Eq. (2.4) can be evaluated easily and only the best possible approximation of  $\Psi_0$  will be obtained.

## 2.3 Hartree-Fock Approximation

One widely used recipe to create a search space of wave-functions is to construct the many-electron wave-function from products of single-electron wave-functions called spin orbitals  $\chi$ . Due to the fermionic nature of electrons this product should be anti-symmetric with respect to particle permutation. This property is fulfilled by a so-called Slater determinant,

$$\psi_{\text{SD}} = \frac{1}{\sqrt{N!}} \begin{vmatrix} \chi_1(\mathbf{r}_1) & \chi_2(\mathbf{r}_1) & \dots & \chi_N(\mathbf{r}_1) \\ \chi_1(\mathbf{r}_2) & \chi_2(\mathbf{r}_2) & \dots & \chi_N(\mathbf{r}_2) \\ \vdots & \vdots & \ddots & \vdots \\ \chi_1(\mathbf{r}_N) & \chi_2(\mathbf{r}_N) & \dots & \chi_N(\mathbf{r}_N) \end{vmatrix} = \frac{1}{\sqrt{N!}} \det\{\chi_1(\mathbf{r}_1) \chi_2(\mathbf{r}_2) \dots \chi_N(\mathbf{r}_N)\}. \quad (2.5)$$

In the Hartree-Fock (HF) approach, the variational principle is then applied to the spin orbitals under the constraint that they remain orthonormal. The total HF energy is given by

$$E_{\text{HF}} = \sum_{i=1}^N \langle i | \hat{h} | i \rangle + \frac{1}{2} \sum_{i=1}^N \sum_{j=1}^N \left( \langle ii | jj \rangle - \langle ij | ji \rangle \right) \quad (2.6)$$

where the following integral abbreviations have been used

$$\begin{aligned} \langle i | \hat{h} | i \rangle &= \int \chi_i^*(\mathbf{r}) \left( \frac{-\nabla^2}{2} + \sum_{k=1}^M \frac{-z_k}{\|\mathbf{r} - \mathbf{R}_k\|_2} \right) \chi_i(\mathbf{r}) d\mathbf{r}, \\ \langle ii | jj \rangle &= \iint \chi_i^*(\mathbf{r}) \chi_j^*(\mathbf{r}') \frac{1}{\|\mathbf{r} - \mathbf{r}'\|_2} \chi_j(\mathbf{r}') \chi_i(\mathbf{r}) d\mathbf{r} d\mathbf{r}', \\ \langle ij | ji \rangle &= \iint \chi_i^*(\mathbf{r}) \chi_j^*(\mathbf{r}') \frac{1}{\|\mathbf{r} - \mathbf{r}'\|_2} \chi_j(\mathbf{r}) \chi_i(\mathbf{r}') d\mathbf{r} d\mathbf{r}'. \end{aligned}$$

Since the minimum of this energy with respect to spin orbital variation should be reached, it is convenient to write this variation in terms of an effective one-electron Fock operator,

$$\hat{f}_i = \hat{h}_i + \sum_{j=1}^N (\hat{J}_j - \hat{K}_j) . \quad (2.7)$$

Here,  $\hat{h}$ —as already mentioned above—describes the one-electron kinetic energy and attraction to the nuclei,  $\hat{J}$  is the Coulomb operator between electrons,

$$\hat{J}_j(\mathbf{r}) = \int \chi_j^*(\mathbf{r}') \frac{1}{\|\mathbf{r} - \mathbf{r}'\|_2} \chi_j(\mathbf{r}') d\mathbf{r}' , \quad (2.8)$$

and  $\hat{K}$  is the exchange operator,

$$\hat{K}_j(\mathbf{r}) = \int \chi_j^*(\mathbf{r}') \frac{1}{\|\mathbf{r} - \mathbf{r}'\|_2} \hat{P}(\mathbf{r}, \mathbf{r}') \chi_j(\mathbf{r}') d\mathbf{r}' , \quad (2.9)$$

which is written here using the operator  $\hat{P}$  that permutes the following pair of spin orbitals, i.e.

$$\hat{P}(\mathbf{r}, \mathbf{r}') \chi_j(\mathbf{r}') \chi_i(\mathbf{r}) = \chi_j(\mathbf{r}) \chi_i(\mathbf{r}') . \quad (2.10)$$

Introducing Lagrangian multipliers  $\epsilon$  to implement the orthonormalization constraints, one finally obtains the HF equations,

$$\hat{f}_i \chi_i = \epsilon_i \chi_i , \quad (2.11)$$

which have the form of an eigenvalue problem. The Fock operator of one spin orbital, however, depends on the form of all other (occupied) spin orbitals *via* the operators  $\hat{J}$  and  $\hat{K}$  which account for the interaction of an electron in said spin orbital with a mean field created by all electrons in the other spin orbitals. Thus, Eq. (2.11) forms a set of coupled equations which need to be solved iteratively until the so-called self-consistent field (SCF) solution is obtained, i.e., the solution  $\chi_i$  of any one HF Eq. (2.11) does not change the mean field in the other equations.

The final energy can also be written in terms of the orbital energies  $\epsilon$ ,

$$E_{\text{HF}} = \sum_{i=1}^N \epsilon_i - \frac{1}{2} \sum_{i=1}^N \sum_{j=1}^N (\langle \chi_i | \hat{J}_j | \chi_i \rangle - \langle \chi_i | \hat{K}_j | \chi_i \rangle) . \quad (2.12)$$

Since the operators  $\hat{J}$  and  $\hat{K}$  are identical when the interaction of one electron  $i$  with itself is calculated, these terms cancel and the unphysical “self-interaction” is exactly zero. This extremely beneficial property makes the HF approach an attractive starting point for more elaborate post-HF methods which aim to cure inherent shortcomings of the HF model such as the missing explicit correlation between electrons and the single-determinant wave-function ansatz.

## 2.4 Density Functional Theory

A huge drawback of HF—and even more so for post-HF methods—is the unfavorable scaling with system size due to the appearing four-center integrals in the Coulomb and exchange operators in practical applications. An appealing alternative is therefore to express the problem in terms of the electron density which is only three-dimensional independent of the system size. This led to the idea of density functional theory (DFT) discussed in this section.

### 2.4.1 Hohenberg-Kohn Theorems

The theoretical justification for the electron density being sufficient to describe the quantum mechanical system is given by the first Hohenberg-Kohn (HK) theorem. Simplified, it states that the Hamiltonian is (up to a constant) uniquely defined by the electron density  $\rho$  and thus also the full ground state wave-function. Furthermore, the second HK theorem states that the variational principle is also applicable in DFT, i.e., the electron density that minimizes the total energy defines the true ground state. In fact, the real problem of DFT arises from the shortcoming that the exact representation of the (electronic) Hamiltonian in functional form of the electron density is unknown. It should be noted here that, in contrast to the density or wave-function, the variational principle does obviously not apply to the Hamiltonian, i.e. one cannot determine the “correct” one by varying it to minimize the total energy. Typically, this total energy is split into contributions of kinetic energy ( $T$ ), classical electron-nucleus ( $E_{ne}$ ) and electron-electron ( $E_{ee}$ ) Coulomb interactions, as well as any non-classical contributions ( $E_{ncl}$ ).

$$E = T_e[\rho] + E_{ee}[\rho] + E_{ne}[\rho] + E_{ncl}[\rho] \quad (2.13)$$

While the classical Coulomb terms can be readily expressed as density functionals,

$$E_{ne}[\rho] = \sum_{k=1}^M \int \frac{-\rho(\mathbf{r})z_k(\mathbf{R}_k)}{\|\mathbf{r} - \mathbf{R}_k\|_2} d\mathbf{r}, \quad (2.14)$$

and

$$E_{ee}[\rho] = \frac{1}{2} \iint \frac{\rho(\mathbf{r})\rho(\mathbf{r}')}{\|\mathbf{r} - \mathbf{r}'\|_2} d\mathbf{r}d\mathbf{r}', \quad (2.15)$$

the real challenge is to find corresponding functional expressions for  $T_e$  and  $E_{ncl}$ . This will now lead to density functional approximations to the so far exact derivations.

### 2.4.2 Kohn-Sham Approach

Early density functional approaches like the Thomas-Fermi model failed to describe chemical bonds mainly due to the unsatisfactory description of the kinetic energy. This motivated Kohn and Sham to split this energy into two parts of which one could be calculated exactly, i.e., the kinetic energy of a non-interacting system. First, a non-interacting reference system with an

effective, local potential  $\hat{V}_{\text{ref}}$  entering the Hamiltonian,

$$\hat{H}_{\text{ref}} = -\frac{1}{2} \sum_{i=1}^N \nabla_i^2 + \sum_{i=1}^N \hat{V}_{\text{ref}} \quad (2.16)$$

is introduced. Similar to the HF approach before, the wave-function of this system is expressed as a Slater determinant of spin orbitals  $\varphi_i$ —here called Kohn-Sham (KS) orbitals. A key feature of this fictitious reference system is that its electron density is exactly the same as  $\varrho_0$  of the real, interacting system, i.e.

$$\sum_{i=1}^N |\varphi_i|^2 = \varrho_0. \quad (2.17)$$

In the reference system, the kinetic energy can be calculated exactly,

$$T_{\text{ref}} = -\frac{1}{2} \sum_{i=1}^N \langle \varphi_i | \nabla^2 | \varphi_i \rangle, \quad (2.18)$$

which, however, is only a part of the interacting kinetic energy,

$$T = T_{\text{ref}} + T_C. \quad (2.19)$$

The missing unknown part,  $T_C$  is then conventionally combined with the other unknown part of the full functional, namely the non-classical potential, forming the so-called exchange-correlation energy,  $E_{\text{XC}}$ . Assigning an exchange-correlation potential  $V_{\text{XC}}$  with this energy, an effective potential  $V_{\text{eff}}$  can be formulated,

$$V_{\text{eff}} = \int \frac{\varrho(\mathbf{r}')}{\|\mathbf{r} - \mathbf{r}'\|_2} d\mathbf{r}' + \sum_{k=1}^M \frac{-z_k}{\|\mathbf{r} - \mathbf{R}_k\|_2} + V_{\text{XC}}, \quad (2.20)$$

with which the KS equations can be expressed as

$$\left( \frac{-\nabla^2}{2} + V_{\text{eff}} \right) \varphi_i = \epsilon_i \varphi_i. \quad (2.21)$$

Like Eq. (2.11), Eq. (2.21) is a result of energy optimization with respect to orbital form under an orthonormalization constraint. Given the large similarity between the HF and the KS approach, it is not surprising that also Eq. (2.21) need to be solved iteratively to obtain an SCF. Note, however, that—in contrast to HF theory—the interaction between an electron with its own mean-field is not exactly compensated by the exchange-correlation term due to a lack of an exact form for the exchange operator. In the following, we will thus also see approached that combine HF and DFT.

### 2.4.3 Exchange-Correlation Functional Approximations

Summarizing the previous findings, the exchange-correlation energy  $E_{\text{XC}}$  consists of all parts of the molecular potential that is not classical Coulomb interaction and of the missing part of the kinetic energy with respect to the non-interacting reference system. All these parts are lacking an



exact expression and need to be approximated in practical applications which led to the advent of various density functional approximations. Those can be roughly categorized by computational complexity into different classes:

LDA In the local density approximation (LDA), the exchange-correlation energy depends only on the local density value which yields good results for systems with slowly varying densities.

GGA The generalized gradient approximation (GGA) additionally includes the local information of the density gradient which usually gives a better description of molecular systems than LDA.

meta-GGA This type of functionals also includes higher order derivatives of the electron density. As the gradients are only evaluated locally, both GGA and meta-GGA are called semi-local functionals.

hybrids Hybrid functionals aim to cure the self-interaction error in the previous density functional approximations, i.e., even in a one electron system, this electron interacts with its own potential. As mentioned before, HF theory is self-interaction free due to the exact exchange operator. When applying the exchange operator to the KS instead of the HF orbitals, one does not obtain the true exchange energy yet something similar that can be used to at least approximately correct the self-interaction error. This is done by mixing said KS-HF exchange energy with the one of the explicit density functional. The approach is further complicated by the fact that the previously mentioned exchange correlation functionals already partially correct for self-interaction error (and other shortcomings not accounted for in HF theory) with varying quality depending on the investigated system. Therefore, there is a whole class of hybrid functionals with varying recipes how to mix the different exchange (or, in the case of double hybrids, also correlation) energies. Examples of such functional approximations are PBE0 [35] which mixes 25 % of KS-HF exchange,  $E_X^{\text{HF}}$ , with the PBE-GGA [36] exchange energy,

$$E_{\text{XC}}^{\text{PBE0}} = 0.25 E_X^{\text{HF}} + 0.75 E_X^{\text{PBE}} + E_C^{\text{PBE}},$$

or HSE06 [37, 38] which splits the exchange energy into short and long range contributions and only mixes the short range part with the KS-HF exchange.

The above listing, however, is far from being exhaustive and the interested reader is referred to the literature on this topic [39].

After having investigated methods to solve the quantum mechanical equations on an atomistic scale, one can go a step further and try to describe macroscopic or, at least, mesoscopic systems. For an ideal, highly symmetric solid-state material which can be represented by a small repetition unit this approach is even feasible. Also, non-interacting particles (with on the order of a few thousand atoms) can be described computationally on the same level. When the system lacks an appropriate symmetry or interacts with a complex environment, however, the necessary computational effort soon renders the full quantum mechanical treatment of the system unfeasible. An example of such a situation is the computation of a molecular species embedded in a liquid environment. In the following chapter, we will present a whole class of methods that (by coarse graining the environment) still allow for a quantum mechanical description of the system's core parts.

### 3 Basic Ingredients for Implicit Solvation

---

Following the idea put forward in a review by Tomasi et al. [16], continuum solvation can be understood in terms of a focused model. In an explicit treatment of the solvent, the total Hamiltonian of the system is given as the sum of solute–solute, solvent–solvent, and solute–solvent interactions.

$$\hat{H}_{\text{total}}(\underline{\mathbf{f}}, \underline{\mathbf{s}}) = \hat{H}_{\text{solute}}(\underline{\mathbf{f}}) + \hat{H}_{\text{solvent}}(\underline{\mathbf{s}}) + \hat{H}_{\text{interaction}}(\underline{\mathbf{f}}, \underline{\mathbf{s}}) \quad (3.1)$$

While only the solute or solvent degrees of freedom,  $\underline{\mathbf{f}}$  or  $\underline{\mathbf{s}}$ , enter in the first two of those terms, the whole set of degrees of freedom is present in the last term.

In a first approximation, one assumes that the interactions within the solvent, given by  $\hat{H}_{\text{solvent}}(\underline{\mathbf{s}})$ , are not influenced by the solute and can thus be simplified as a constant offset in energy. This, however, does not yet eliminate the solvent degrees of freedom  $\underline{\mathbf{s}}$  which are still present in the interaction Hamiltonian with the solute.

The second, more aggressive approximation is to replace the explicit dependence on solvent degrees of freedom  $\underline{\mathbf{s}}$  in the solute–solvent interaction Hamiltonian,  $\hat{H}_{\text{interaction}}(\underline{\mathbf{f}}, \underline{\mathbf{s}})$ , by a response function  $S(\mathbf{r}, \mathbf{r}')$  and neglect any explicit contribution to the kinetic energy operator  $\hat{T}$ .

Both approximations combined lead to the following effective Hamiltonian

$$\hat{H}_{\text{total}}^{\text{approx}}(\underline{\mathbf{f}}) = \hat{T}_{\text{solute}}(\underline{\mathbf{f}}) + \hat{V}_{\text{solute}}(\underline{\mathbf{f}}) + \hat{V}_{\text{interaction}}^{\text{approx}}[\underline{\mathbf{f}}, S(\mathbf{r}, \mathbf{r}')]. \quad (3.2)$$

where  $\hat{V}$  denotes the potential energy operator. Note, that  $\mathbf{r}$  and  $\mathbf{r}'$  are just regular position vectors. This marks a drastic reduction of complexity as any sampling now only includes solute degrees of freedom  $\underline{\mathbf{f}}$ —typically a much smaller set than the solvent degrees of freedom.

The price of this simplification comes with the problem of finding a proper response function  $S$ . Conventionally,  $S$  is assumed to be only a local function  $S(\mathbf{r})$  which solely contains the (dipole) polarization response of the solvent. This part is illuminated in more detail in section 3.1 which will lead to the first ingredient of all continuum solvation models, the dielectric permittivity function.

The second ingredient are non-electrostatic (or sometimes called non-mean-field) terms as discussed in section 3.4. Present in all modern continuum solvation models, these extend the electrostatic response kernel by effective models for previously partially or completely ignored effects such as dispersion interaction or Pauli repulsion.

Last but not least, solute and solvent are not only separated in phase space but also in real space by a solvation cavity. This third ingredient will be encountered in section 3.5 where different definitions and contributions to the non-electrostatic model are presented.

## 3.1 Electrostatic Model

### 3.1.1 Vacuum Electrostatic Potential

We have seen that the Hamiltonian of the solvated system can be approximated by Eq. (3.2). This expression only differs from the Hamiltonian of the solute *in vacuo* by the additional interaction potential  $\hat{V}_{\text{interaction}}^{\text{approx}}$ . In order to understand the latter term, it is didactically helpful to analyze the solute's potential energy operator  $\hat{V}_{\text{solute}}$  which—in the absence of an external field—is solely determined by the solute's charge distribution  $\rho_{\text{solute}}^{\text{vac}}$  *in vacuo*. The governing electrostatic equation in this case is Gauss's law, Eq. (3.3), which relates this charge distribution to the electrostatic field  $\mathbf{E}$ .<sup>1</sup>

$$\nabla \cdot \mathbf{E}(\mathbf{r}) = 4\pi\rho_{\text{solute}}^{\text{vac}}(\mathbf{r}) \quad (3.3)$$

The relationship between the (static) field  $\mathbf{E}$  and  $\hat{V}_{\text{solute}} = \Phi_{\text{H}}$  is then simply given by

$$\mathbf{E}(\mathbf{r}) = -\nabla\Phi_{\text{H}}(\mathbf{r}). \quad (3.4)$$

Inserting Eq. (3.4) into Eq. (3.3) yields the well-known Poisson equation

$$\nabla \cdot (\nabla\Phi_{\text{H}}(\mathbf{r})) = -4\pi\rho_{\text{solute}}^{\text{vac}}(\mathbf{r}). \quad (3.5)$$

We have chosen the symbol  $\Phi_{\text{H}}$  because the electrostatic potential of a charge distribution in vacuum is often referred to as Hartree potential. It should be pointed out here that the solution to Eq. (3.5) is uniquely defined by imposing appropriate boundary conditions, e.g. when we require the potential to decay to zero at infinity (Dirichlet boundary conditions)

$$\lim_{\mathbf{r} \rightarrow \infty} \Phi_{\text{H}}(\mathbf{r}) = 0. \quad (3.6)$$

### 3.1.2 Electrostatic Potential of the Solvated System

Equation (3.5) can also directly be used in an explicit solvation approach with the total charge density,

$$\rho_{\text{total}}^{\text{vac}} = \rho_{\text{solute}} + \rho_{\text{solvent}}, \quad (3.7)$$

because the expected screening due to the surrounding environment will be explicitly accounted for. Due to the reduction of degrees of freedom in an implicit solvation approach to those of the solute, however,  $\rho_{\text{solvent}}$  is not accessible. Instead—as outlined before Eq. (3.2)—a response function is needed to describe the solvent's influence on the solute. In a very simplified picture, this effect is just the induction of dipole moments  $\mathbf{p}_i$  due to charge rearrangements within the solvent which can be summarized in a polarization density  $\mathbf{P}$  in the occupied volume  $V$ ,

$$\mathbf{P} = \frac{1}{V} \sum_i \mathbf{p}_i. \quad (3.8)$$

---

<sup>1</sup>Note again that Gaussian units are used for electromagnetic quantities unless stated otherwise.

The exact nature of these dipoles is not important, but they can e.g. be thought of as the contributions of all solvent molecules within range. In order to calculate  $\mathbf{P}$ , one is left to assume a certain behavior of the solvent. It is usually implied that the dielectric medium is isotropic, linear, and homogeneous. In this work, we follow this assumption and write  $\mathbf{P}$  in a simple linear relationship in terms of  $\mathbf{E}$  defining the (first order) electric susceptibility  $\chi$ .

$$\mathbf{P}(\mathbf{r}) = \chi \mathbf{E}(\mathbf{r}) \quad (3.9)$$

Before continuing the derivation, it is appropriate to shortly evaluate the effect and validity of the aforementioned assumptions about the solvent properties.

**Isotropy** If the medium were not isotropic,  $\mathbf{P}$  would not be aligned with  $\mathbf{E}$  and thus  $\chi$  would become a tensor instead of a scalar. While this is an inherent property of any bulk liquid, a certain degree of ordering can be expected, e.g., at an interface of the solvent such as the one with the solute. In fact, investigations on liquid-liquid interfaces revealed a highly anisotropic behavior of the dielectric response—even reaching several layers of molecules into the bulk. Therefore, this approximation certainly deserves further investigation and will hopefully receive improvements in the future.

**Linearity** In the case of a non-linear solvent, one would have to include second or higher order terms ( $\chi^{(2)}\mathbf{E}^2$ ,  $\chi^{(3)}\mathbf{E}^3$ , ...) in Eq. (3.9). Obviously, this approximation depends very much on the strength of the electric field as the higher order terms in the expansion are usually negligible for small values of  $\mathbf{E}$ . Gauging the electric field on an atomistic scale, however, is not a trivial task. Unfortunately, Poisson's equation is no longer valid in the non-linear regime and an appropriate theory is yet to be fully developed [16]. Therefore, non-linear effects are usually studied (if at all) indirectly through a modification, commonly called saturation effect, of the dielectric permittivity within the linear approximation [40].

**Homogeneity** In a non-homogeneous medium, the electric susceptibility  $\chi$  of Eq. (3.9) would not be constant but a function of the solvent degrees of freedom  $\underline{s}$ . Solvating a solute molecule in a solvent naturally introduces such a local inhomogeneity and thus we will from now on express this dependency as  $\chi(\mathbf{r})$ . Note, however, that this is distinctly different from inhomogeneities in the bulk solvent which would necessitate an explicit approach.

A further approximation has already been made before Eq. (3.9) in the sense that only dipole and no higher order polarizations are accounted for [17]. More importantly, however, only Coulomb interactions between the solute and the solvent charge density are considered and any explicit electron exchange or correlation between the two is lost in the simple form of the purely local response function  $S(\mathbf{r}) \propto \chi(\mathbf{r})$ . While the former approximations might only require further treatment in special cases, the latter one has to be accounted for immediately and this topic will be revisited in section 3.4.

Relying on the aforementioned approximations,  $\hat{V}_{\text{interaction}}^{\text{approx}} = \Phi_{\mathbf{P}}$  is simply given by the following relation in analogy to Eq. (3.4):

$$4\pi\mathbf{P}(\mathbf{r}) = 4\pi\chi(\mathbf{r})\mathbf{E}(\mathbf{r}) = -\nabla\Phi_{\mathbf{P}}(\mathbf{r}) . \quad (3.10)$$

Note, that the factor  $4\pi$  arises due to the Gaussian unit system. One can also formulate Gauss's law for the polarization density  $\mathbf{P}$  in order to obtain the induced charge distribution  $\varrho_P$ .

$$\nabla \cdot (4\pi\mathbf{P}(\mathbf{r})) = \nabla \cdot (4\pi\chi(\mathbf{r})\mathbf{E}(\mathbf{r})) = 4\pi\varrho_P(\mathbf{r}) \quad (3.11)$$

The charge distribution of the solvated solute,  $\varrho_{\text{solute}}$ , is now the sum of its charge distribution *in vacuo* and the induced charge distribution,

$$\varrho_{\text{solute}} = \varrho_{\text{solute}}^{\text{vac}} + \varrho_P, \quad (3.12)$$

and the total effective electric field is called displacement field

$$\mathbf{D}(\mathbf{r}) = \mathbf{E}(\mathbf{r}) + 4\pi\mathbf{P}(\mathbf{r}) = (1 + 4\pi\chi(\mathbf{r})) \mathbf{E}(\mathbf{r}) = \varepsilon(\mathbf{r})\mathbf{E}(\mathbf{r}). \quad (3.13)$$

Here, we introduced the dielectric permittivity  $\varepsilon$  which is a more commonly used property compared to the electric susceptibility.

Putting all pieces together, one obtains the macroscopic version of Gauss's law

$$\nabla \cdot \mathbf{D}(\mathbf{r}) = 4\pi\varrho_{\text{solute}}(\mathbf{r}) \quad (3.14)$$

which has the form of a generalized Poisson equation in terms of the electrostatic potential  $\Phi$ :

$$\nabla \cdot (\varepsilon(\mathbf{r})\nabla\Phi) = -4\pi\varrho_{\text{solute}}(\mathbf{r}) \quad (3.15)$$

Equation (3.15) replaces Eq. (3.5) as the central electrostatic equation to solve and the resulting potential includes both potential energy operators of Eq. (3.2).

$$\Phi = \Phi_H + \Phi_P = \hat{V}_{\text{solute}} + \hat{V}_{\text{interaction}}^{\text{approx}} \quad (3.16)$$

### 3.1.3 Electrostatic Energy

With the electrostatic (free) energy of the charge distribution in this field being an observable more accessible than the field itself, we want to determine this energy using the textbook [41] electrostatic equation,

$$G_{\text{el}} = \frac{1}{2} \int_V \varrho_{\text{solute}}(\mathbf{r})\Phi(\mathbf{r}) \, d\mathbf{r} = \frac{1}{2} \int_V (\varrho_{\text{solute}}^{\text{vac}}(\mathbf{r}) + \varrho_P(\mathbf{r})) (\Phi_H(\mathbf{r}) + \Phi_P(\mathbf{r})) \, d\mathbf{r}. \quad (3.17)$$

By referencing to the energy of the solute's charge density in vacuum,

$$G_{\text{el}}^{\text{vac}} = \frac{1}{2} \int_V \varrho_{\text{solute}}^{\text{vac}}(\mathbf{r})\Phi_H(\mathbf{r}) \, d\mathbf{r}, \quad (3.18)$$

one can now also define an electrostatic free energy of solvation  $\Delta G_{\text{el}}$ .

$$\Delta G_{\text{el}} = G_{\text{el}} - G_{\text{el}}^{\text{vac}} = \underbrace{\frac{1}{2} \int_V \varrho_{\text{solute}}^{\text{vac}}(\mathbf{r})\Phi_P(\mathbf{r}) \, d\mathbf{r}}_{\text{rigid}} + \underbrace{\frac{1}{2} \int_V \varrho_P(\mathbf{r}) (\Phi_H(\mathbf{r}) + \Phi_P(\mathbf{r})) \, d\mathbf{r}}_{\text{polarizable}} \quad (3.19)$$

One can distinguish between two different scenarios. In the approximation of a "rigid" charge

distribution, the latter does not react to the induced field, i.e.  $\rho_{\text{solute}} = \rho_{\text{solute}}^{\text{vac}}$ . Therefore, only the first integral labeled “rigid” contributes to  $\Delta G_{\text{el}}$  and the one labeled “polarizable” vanishes ( $\rho_{\text{p}} = 0$ ). This means that  $\Phi_{\text{p}}$  only needs to be evaluated once and can be added as a post-correction. In the full, self-consistent picture, however, the charge distribution will react to the induced field and thus also the “polarizable” term of Eq. (3.19) has to be accounted for.

### 3.2 Model for the Dielectric Function

In the last section, we have derived the basic electrostatic equation of implicit solvation, Eq. (3.15), and thereby introduced the dielectric permittivity function  $\varepsilon(\mathbf{r})$ . As alluded to above,  $\varepsilon$  determines the polarization of the solvent in the presence of the electric field of the solute. Therefore,  $\varepsilon$  should equal 1 in the core region of the solute which the solvent molecules cannot penetrate and it should reach the solvent bulk value,  $\varepsilon_{\text{b}}$ , far away from the solute. The exact form of  $\varepsilon$  at the interface of solute and solvent, however, is still under investigation and not fully clarified. Furthermore, given the approximations and limitations listed above that come with the form of a (scalar) dielectric permittivity,  $\varepsilon(\mathbf{r})$  should be seen as an effective parameter of the implicit solvent model rather than a rigorously defined physical quantity—especially since the definition of a local dielectric permittivity on an atomistic scale is questionable anyway. In this light it is also not easy to answer whether a sharp step-like transition or a smooth function of any sort is the better form for  $\varepsilon(\mathbf{r})$ .

For the sake of convenience,  $\varepsilon$  is chosen such that it fits the applied method to solve Eq. (3.15) and *vice versa*. Some of those methods perform a direct integration of Eq. (3.15) and therefore necessarily require a certain smoothness of the dielectric function  $\varepsilon(\mathbf{r})$  [21, 42]. In this work, however, we will exclusively focus on another very popular choice based on a piecewise constant  $\varepsilon$  with a step-like transition between the regions of solute and solvent. This latter picture readily translates into the very longstanding concept of an implicit solvent cavity which is usually also recovered for smooth dielectric functions. How such a cavity can be realized will be discussed in more detail in section 3.5. For now, it is sufficient to know that the cavity and the dielectric function are usually directly related in a way that one can derive the one from the other.

Defining a function  $\mathcal{C}(\mathbf{r})$  that is  $< 0$  inside of the cavity and  $> 0$  outside—as illustrated in Fig. 3.1—one can express the (discontinuous) function  $\varepsilon(\mathbf{r})$  in terms of Heaviside step functions  $\Theta$  and the bulk permittivity  $\varepsilon_{\text{b}}$ .

$$\varepsilon(\mathbf{r}) = \varepsilon_{\text{b}}\Theta[\mathcal{C}(\mathbf{r})] + (1 - \Theta[\mathcal{C}(\mathbf{r})]) \quad (3.20)$$

Inserting Eq. (3.20) into the generalized Poisson Equation (3.15) reveals the advantage of the piecewise constant form, namely the problem decays into two regular Poisson equations

$$-4\pi\rho_{\text{solute}}(\mathbf{r}) = \begin{cases} \nabla \cdot \nabla\Phi, & \mathcal{C}(\mathbf{r}) < 0 \\ \nabla \cdot \varepsilon_{\text{b}}\nabla\Phi = \varepsilon_{\text{b}}\nabla \cdot \nabla\Phi, & \mathcal{C}(\mathbf{r}) > 0 \end{cases}, \quad (3.21a)$$

or, equivalently,

$$\nabla \cdot \nabla\Phi = -4\pi\rho_{\text{solute}}(\mathbf{r}) \begin{cases} 1, & \mathcal{C}(\mathbf{r}) < 0 \\ \varepsilon_{\text{b}}^{-1}, & \mathcal{C}(\mathbf{r}) > 0 \end{cases}. \quad (3.21b)$$

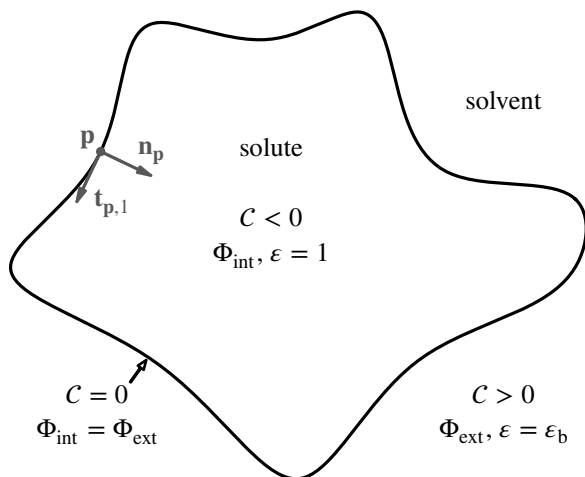


Fig. 3.1: Schematic picture of the cavity function  $\mathcal{C}$ . For a point  $\mathbf{p}$  on the cavity surface, the local coordinate system with the normal vector,  $\mathbf{n}_{\mathbf{p}}$ , and one tangent vector,  $\mathbf{t}_{\mathbf{p},1}$ , is sketched in gray. Reprinted with permission from Ref. [1]. © 2017 American Chemical Society.

This naturally leads to a separation of the electrostatic potential into internal,  $\Phi_{\text{int}}$ , and external,  $\Phi_{\text{ext}}$ , contributions—as shown in Figure 3.1. These two need to fulfill the following boundary conditions (taken again from textbook electrostatics [41]),

$$\Phi_{\text{int}}(\mathbf{p}) = \Phi_{\text{ext}}(\mathbf{p}) \quad (3.22a)$$

$$\mathbf{n}_{\mathbf{p}} \cdot \nabla \Phi_{\text{int}}(\mathbf{p}) = \mathbf{n}_{\mathbf{p}} \cdot \epsilon_b \nabla \Phi_{\text{ext}}(\mathbf{p}) \quad (3.22b)$$

for any point  $\mathbf{p}$  on the cavity surface, i.e.,  $\mathcal{C}(\mathbf{p}) = 0$ . It should be mentioned here, that we enforce the same boundary conditions on the polarization potential—and therefore on the whole potential  $\Phi$ —at infinite distance from the solute as given in Eq. (3.6) for the Hartree potential, i.e.

$$\lim_{\mathbf{r} \rightarrow \infty} \Phi_{\text{ext}}(\mathbf{r}) = 0. \quad (3.23)$$

Assuming a closed cavity surface, the above boundary conditions again uniquely define the solution to Eq. (3.21) which is to be determined in the following.

### 3.3 Solution Approaches to the Electrostatic Model

Although we have restricted ourselves (see section 3.2) to a certain form of the dielectric function  $\epsilon(\mathbf{r})$ , still several different approaches have been developed to solve Eq. (3.21) or directly determine the (free) energy of solvation, Eq. (3.19). To put our efforts into perspective, a small selection of those methods will be presented in the following.

### 3.3.1 Generalized Born Approach

The foundation of this model has been laid by Born in 1920 [43] with the calculation of the electrostatic (free) energy  $\Delta G_{\text{el}}$  of a sphere with radius  $a$  carrying a charge  $q$  in a medium with a dielectric permittivity  $\epsilon_b$ .

$$\Delta G_{\text{el}}^{\text{Born}} = \frac{1}{2} \left( \frac{1}{\epsilon_b} - 1 \right) \frac{q^2}{a} \quad (3.24)$$

This is equivalent to a setup where a point charge  $q$  is placed in the center of a spherical void within the same dielectric medium [44]. Without loss of generality, we assume the charge is located at the origin of the coordinate system. For symmetry reasons, the problem can furthermore be reduced to one dimension, i.e., the radial coordinate  $r$ . Due to the screening of the monopole by the dielectric medium outside of the cavity, the external potential is given by

$$\Phi_{\text{ext}}^{\text{Born}}(r) = \frac{q}{\epsilon_b r}, \quad r > a. \quad (3.25)$$

At a radius  $r = a$ , i.e., on the cavity surface, this potential has to match  $\Phi_{\text{int}}$  as stated in Eq. (3.22a) which in turn is the sum of  $\Phi_{\text{H}}$  and  $\Phi_{\text{P}}^{\text{Born}}$ . Therefore,

$$\Phi_{\text{P}}^{\text{Born}}(a) = \Phi_{\text{ext}}^{\text{Born}}(a) - \Phi_{\text{H}}(a) = \frac{q}{\epsilon_b a} - \frac{q}{a} = \left( \frac{1}{\epsilon_b} - 1 \right) \frac{q}{a} \quad (3.26)$$

Evaluating the second boundary condition, Eq. (3.22b), on the cavity surface yields

$$\left. \frac{\partial (\Phi_{\text{H}} + \Phi_{\text{P}}^{\text{Born}})}{\partial r} \right|_a = \epsilon_b \left. \frac{\partial \Phi_{\text{ext}}^{\text{Born}}}{\partial r} \right|_a, \quad (3.27)$$

and therefore

$$\left. \frac{\partial \Phi_{\text{P}}^{\text{Born}}}{\partial r} \right|_a = -\epsilon_b \frac{q}{\epsilon_b a^2} + \frac{q}{a^2} = 0. \quad (3.28)$$

At this point it is important to note that the charge distribution in the Born model is rigid and thus  $\Phi_{\text{P}}^{\text{Born}}$  has no source within the cavity. This means that  $\Phi_{\text{P}}^{\text{Born}}$  needs to fulfill Laplace's equation.

$$\frac{\partial^2 \Phi_{\text{P}}^{\text{Born}}}{\partial r^2} = 0 \quad (3.29)$$

Given the above result that the gradient of  $\Phi_{\text{P}}^{\text{Born}}$  needs to be zero at the cavity surface, it is rather straightforward to see that a constant function with the value given from Eq. (3.26) fulfills the boundary conditions. Thus,

$$\Phi_{\text{P}}^{\text{Born}}(r) = \left( \frac{1}{\epsilon_b} - 1 \right) \frac{q}{a}, \quad r < a \quad (3.30)$$

Evaluating the solvation energy of the (rigid) point charge *via* Eq. (3.19), we again arrive at Born's Eq. (3.24).



Obviously, this model is too simple to be used in connection with realistic solutes such as molecules due to the restriction to a single, spherical cavity. An important generalization, called generalized Born (GB) model, was achieved by Still and co-workers [45] which allows the calculation of  $n$  point charges  $q_i$ , each one in its own spherical cavity with an individual radius  $a_i$ .

$$\Delta G_{\text{el}}^{\text{GB}} = \frac{1}{2} \left( \frac{1}{\epsilon_{\text{b}}} - 1 \right) \sum_{i=1}^n \sum_{j=1}^n \frac{q_i q_j}{f_{\text{GB}}} \quad (3.31)$$

using an effective interaction distance

$$f_{\text{GB}} = \sqrt{r_{ij}^2 + a_i a_j \exp\left(-\frac{r_{ij}^2}{4a_i a_j}\right)}. \quad (3.32)$$

As reported by others, this expression nicely reproduces the physical limits of Eq. (3.31) for very small or very large distances  $r_{ij}$  between the charges [45].

While this model has been applied very successfully [46–48]—especially in connection with elaborate non-electrostatic terms, see section 3.4—its disadvantage is that it requires a large set of fit parameters, i.e., the Born radii  $a_i$  which depend on the species, the solvent, and also on the charge state.

### 3.3.2 Apparent Surface Charge Method

As a next step, we want to generalize the cavity model from interlocked spheres in the GB approach to an arbitrarily shaped cavity surface. Furthermore, the charge distribution is no longer restricted to point charges. This can be achieved with so-called apparent surface charge (ASC) methods. The general idea behind all those models is to represent the polarization potential (reaction field) as a Newton single layer potential  $U_1$  of a continuous charge distribution  $\sigma$  on the cavity surface [16].

$$U_1(\mathbf{r}) = \int_{\mathcal{C}(\mathbf{p})=0} \frac{\sigma(\mathbf{p})}{\|\mathbf{r} - \mathbf{p}\|_2} \mathrm{d}\mathbf{p} \quad (3.33)$$

In order to understand the viability of this approach, it is helpful to recall some properties of the Newtonian single layer potential provided that  $\sigma$  is smooth enough (see e.g. [44]). Given the (inwards pointing) normal vector  $\mathbf{n}_{\mathbf{p}}$  on a point  $\mathbf{p}$  on the cavity surface, i.e.,  $\mathcal{C}(\mathbf{p}) = 0$ , the following properties can be formulated:

- The potential is continuous at all points in space<sup>2</sup>, also at the cavity surface

$$\lim_{\delta \rightarrow 0} \left( U_1(\mathbf{p} + \delta \mathbf{n}_{\mathbf{p}}) - U_1(\mathbf{p} - \delta \mathbf{n}_{\mathbf{p}}) \right) = 0, \quad (3.34a)$$

and has derivatives of all orders.

---

<sup>2</sup>The apparent singularity at  $\mathbf{r} = \mathbf{p}$  can be lifted

- The first derivative shows a jump in the direction of the surface normal.

$$\lim_{\delta \rightarrow 0^+} \left( \mathbf{n}_p \cdot \nabla U_1 \Big|_{\mathbf{p} + \delta \mathbf{n}_p} - \mathbf{n}_p \cdot \nabla U_1 \Big|_{\mathbf{p} - \delta \mathbf{n}_p} \right) = 4\pi\sigma(\mathbf{p}) \quad (3.34b)$$

- The potential satisfies Laplace's equation inside and outside of the cavity.

$$\nabla \cdot \nabla U_1 = 0 \quad (3.34c)$$

Comparing Eqs. (3.34a) and (3.34b) to Eqs. (3.22a) and (3.22b) above, one immediately sees that the single layer potential  $U_1$  can nicely reproduce the boundary conditions for the total electrostatic potential given the correct surface charge distribution  $\sigma$ . However, Eq. (3.34c) shows that  $U_1$  cannot be the solution to Eq. (3.21) as it only describes a potential that has no source at any point not on the cavity surface. This can be solved by splitting the total potential into different parts as will be shown later.

To the best of the author's knowledge, all ASC methods so far (in their initial derivation) require the total charge to be located strictly inside the cavity and by doing so reduce the external problem to Laplace's equation. Actually, this is only true in realistic systems for the nuclear charge density while the electron density will always have a non-vanishing tail that penetrates into the exterior volume for any reasonably sized cavity. However, since the fraction of so-called outlying charge is usually small, the agreement with exact integration is still remarkable—mostly due to correction terms that have been broadly addressed in literature [49–51] and thus will not be discussed here.

In order to distinguish it from the real one, the localized charge density is in the following denoted  $\tilde{q}_{\text{solute}}$ . The same approach can be used again as before in the Born model, namely, separating off the solution to Poisson's equation *in vacuo*, Eq. (3.5), for the source generated by  $\tilde{q}_{\text{solute}}$ .

$$\Phi_{\text{int}}^{\text{ASC}} = \tilde{\Phi}_{\text{H}} + \Phi_{\text{P}}^{\text{ASC}} \quad (3.35)$$

Since there is no other source in the cavity than the one in

$$\nabla \cdot \nabla \tilde{\Phi}_{\text{H}} = -4\pi\tilde{q}_{\text{solute}}, \quad (3.36)$$

$\Phi_{\text{P}}^{\text{ASC}}$  has to be the solution to Laplace's equation and can therefore be represented by the Newtonian single-layer potential  $U_1$ . In order to find the appropriate surface charge distribution function  $\sigma$ , all ASC methods rely on a tessellation of the surface, i.e., decomposing it completely into non-overlapping surface elements each with an assigned area element  $o_k$  such that the sum of all  $o_k$  adds up to the total surface area  $O$  of the cavity. These so-called *tesserae* need to be chosen small enough such that the continuous distribution  $\sigma$  can be assumed to be constant within each *tessera* and may thus be approximated by a point charge  $q_k = \sigma(\mathbf{p}_k)o_k$  located at the *tessera*'s center  $\mathbf{p}_k$  [16].

$$\int_{C(\mathbf{p})=0} \frac{\sigma(\mathbf{p})}{\|\mathbf{r} - \mathbf{p}\|_2} d\mathbf{p} \approx \sum_k \frac{q_k}{\|\mathbf{r} - \mathbf{p}_k\|_2} \quad (3.37)$$

Based on the original polarizable continuum model (PCM) implementation [52] (nowadays rather

called DPCM), the model has received countless extensions and revisions [16]. Of all PCM flavors, the integral equation formalism (IEF) has become the most popular one in recent years. It should be noted here that a few other popular implicit solvation methods are also related to the IEF-PCM, such as the surface and simulation of volume polarization for electrostatics (SS(V)PE) method [53]—which has been shown [54] to coincide with IEF-PCM under some circumstances—or the conductor-like screening model (COSMO) [55]—which can be seen as an approximation to the IEF-PCM [16].

### 3.3.3 Multipole Expansion Model

Historically, the foundation of modern multipole expansion (MPE) methods has been laid with the work on model systems of simple point charge or point dipole distributions in spherical [19, 56, 57] or ellipsoidal [58] cavities—not much more complicated than the Born model presented earlier. Mainly due to efforts of scientists working in Nancy in France, the MPE model has received important generalizations [20, 59] such that it can be applied to realistic solutes with a continuous charge distribution situated in arbitrarily shaped, smooth cavities. The basic idea behind MPE is to expand the electrostatic polarization potential (reaction field) in terms of regular,

$$\mathcal{R}_m^l(\mathbf{x}) = \sqrt{\frac{4\pi}{2l+1}} (\|\mathbf{x}\|_2)^l Y_m^l(\mathbf{x}), \quad (3.38a)$$

and/or irregular solid harmonics,

$$\mathcal{I}_m^l(\mathbf{x}) = \sqrt{\frac{4\pi}{2l+1}} (\|\mathbf{x}\|_2)^{-l-1} Y_m^l(\mathbf{x}), \quad (3.38b)$$

where  $Y_m^l$  are spherical harmonic functions of degree  $l$  and order  $m$ .

Before diving into a similar derivation as in the previous section, one should note that—being harmonic functions—the solid harmonics solve Laplace’s equation as did the Newtonian single-layer potential (cf. Eq. (3.34c)). Thus, there should always be a direct mapping between the ASC and the MPE potential, and *vice versa* [49]. Instead of simply transforming the representation of the polarization potential, however, we will in the following start the derivation again from Eq. (3.21a) in order to avoid the so-called outlying charge error the ASC methods all suffer from more or less severely. Therefore, we may not assume a localization of the charge within the cavity. However, the problem of the polarization potential still needs to be reduced to a Laplace equation in order to be able to develop it in the solid harmonic functions, Eq. (3.38), above. In the first step, we assume that the solution to Poisson’s equation *in vacuo*,  $\Phi_{\text{H}}^{(0)}$ , can be calculated exactly for a given charge density of the solute  $\rho_{\text{solute}}^{(0)}$ . The corresponding equation is equivalent to Eq. (3.5).

$$\nabla \cdot \nabla \Phi_{\text{H}}^{(0)} = -4\pi \rho_{\text{solute}}^{(0)} \quad (3.39)$$

In fact, all DFT and also many other QM codes include such solvers as a core functionality. Note again, that  $\rho_{\text{solute}}^{(0)}$  is *not* artificially localized within the cavity.

Multiplying both sides of Eq. (3.39) with the reciprocal of the dielectric function  $\epsilon$  of Eq. (3.20)

yields

$$\nabla \cdot \nabla \Phi_{\text{H}}^{(0)}(\mathbf{r}) \begin{cases} 1 \\ \varepsilon_{\text{b}}^{-1} \end{cases} = -4\pi \varrho_{\text{solute}}^{(0)}(\mathbf{r}) \begin{cases} 1, & \mathcal{C}(\mathbf{r}) < 0 \\ \varepsilon_{\text{b}}^{-1}, & \mathcal{C}(\mathbf{r}) > 0 \end{cases} \quad (3.40)$$

Now, we define a potential  $\Phi_{\delta}^{(0)}$  as the difference between the full electrostatic potential  $\Phi$  of Eq. (3.21a) and the scaled Hartree potential  $\Phi_{\text{H}}^{(0)}$  of Eq. (3.40).

$$\Phi(\mathbf{r}) \equiv \left(\varepsilon(\mathbf{r})\right)^{-1} \Phi_{\text{H}}^{(0)}(\mathbf{r}) + \Phi_{\delta}^{(0)}(\mathbf{r}), \quad \mathcal{C}(\mathbf{r}) \neq 0 \quad (3.41)$$

Exploiting the linearity of the Laplace operator  $\nabla \cdot \nabla$ , one readily obtains the following result:

$$\nabla \cdot \nabla \Phi_{\delta}^{(0)}(\mathbf{r}) = -4\pi \left( \varrho_{\text{solute}} - \varrho_{\text{solute}}^{(0)} \right) \begin{cases} 1, & \mathcal{C}(\mathbf{r}) < 0 \\ \varepsilon_{\text{b}}^{-1}, & \mathcal{C}(\mathbf{r}) > 0 \end{cases}. \quad (3.42)$$

In the above expression,  $\varrho_{\text{solute}}$  is the relaxed charge density of the solute in presence of the dielectric continuum. Initially,  $\varrho_{\text{solute}}^{(0)}$  equals  $\varrho_{\text{solute}}^{\text{vac}}$ , i.e., the charge density of the solute *in vacuo* and the right-hand side of Eq. (3.42) is non-zero. When this methodology is applied in an SCF method, however,  $\Phi_{\delta}^{(0)}$  (together with the scaled  $\Phi_{\text{H}}^{(0)}$ ) can be used to update the solute's charge density to  $\varrho_{\text{solute}}^{(1)}$ . For the new charge density, Eqs. (3.39) and (3.42) can be applied in turn to obtain a new potential  $\Phi_{\delta}^{(1)}$ . Provided that self-consistency can be reached after  $i$  steps,  $\varrho_{\text{solute}}^{(i)}$  has to equal  $\varrho_{\text{solute}}$  up to numerical accuracy. This implies that the self-consistent polarization potential  $\Phi_{\text{p}}^{\text{MPE}} = \Phi_{\delta}^{(i)}$  has to fulfill Laplace's equation and can thus be exactly expressed in terms of the solid harmonic functions in Eq. (3.38).

$$\nabla \cdot \nabla \Phi_{\text{p}}^{\text{MPE}}(\mathbf{r}) = 0, \quad \mathcal{C}(\mathbf{r}) \neq 0 \quad (3.43)$$

For the sake of simplicity of notation,  $\Phi_{\text{p}}^{\text{MPE}}$  is split into parts inside,  $\Phi_{\text{R}}$ , and outside,  $\Phi_{\text{Q}}$ , of the cavity.

$$\Phi(\mathbf{r}) = \begin{cases} \Phi_{\text{int}}(\mathbf{r}) = \Phi_{\text{R}}(\mathbf{r}) + \Phi_{\text{H}}(\mathbf{r}), & \mathcal{C}(\mathbf{r}) < 0 \\ \Phi_{\text{ext}}(\mathbf{r}) = \Phi_{\text{Q}}(\mathbf{r}) + \varepsilon_{\text{b}}^{-1} \Phi_{\text{H}}(\mathbf{r}), & \mathcal{C}(\mathbf{r}) > 0 \end{cases} \quad (3.44)$$

Here, the vacuum potential of the (current) charge density is simply denoted  $\Phi_{\text{H}}$  and should not be confused with the "real" Hartree potential created by the unperturbed vacuum charge density.

Evaluating the boundary conditions of the electrostatic potential, Eqs. (3.22a) and (3.22b), one obtains the following important relations:

$$\Phi_{\text{R}}(\mathbf{p}) - \Phi_{\text{Q}}(\mathbf{p}) = \left(\varepsilon_{\text{b}}^{-1} - 1\right) \Phi_{\text{H}}(\mathbf{p}), \quad (3.45a)$$

$$\mathbf{n}_{\text{p}} \cdot \nabla \Phi_{\text{R}}(\mathbf{p}) - \mathbf{n}_{\text{p}} \cdot \varepsilon_{\text{b}} \nabla \Phi_{\text{Q}}(\mathbf{p}) = 0, \quad (3.45b)$$

where  $\mathbf{n}_{\text{p}}$  is the (inwards pointing) normal vector on a point  $\mathbf{p}$  on the cavity surface, i.e.,  $\mathcal{C}(\mathbf{p}) = 0$ . One way to determine  $\Phi_{\text{R}}$  and  $\Phi_{\text{Q}}$  from Eqs. (3.45a) and (3.45b) will be presented later on. Once

those potentials are known, the full electrostatic potential is given by Eq. (3.44).

Having derived the central MPE equations, we can now attempt to find a corresponding Newtonian potential. Comparing Eq. (3.45b) to Eq. (3.34b), one immediately sees that  $\sigma$  of a single-layer representation needs to be zero everywhere on the surface. This leads us to the so-called double-layer potential  $U_2$  created by a surface dipole distribution  $\varpi$ ,

$$U_2(\mathbf{r}) = \int_{\mathcal{C}(\mathbf{p})=0} \varpi(\mathbf{p}) \mathbf{n}_p \cdot \nabla_p \left( \|\mathbf{r} - \mathbf{p}\|_2 \right)^{-1} d\mathbf{p} = \int_{\mathcal{C}(\mathbf{p})=0} \varpi(\mathbf{p}) \frac{\mathbf{n}_p \cdot (\mathbf{r} - \mathbf{p})}{\left( \|\mathbf{r} - \mathbf{p}\|_2 \right)^3} d\mathbf{p}, \quad \mathcal{C}(\mathbf{r}) \neq 0, \quad (3.46)$$

with the following properties [60]:

- The potential is continuous at all points in space except at the cavity surface across which it exhibits a jump

$$\lim_{\delta \rightarrow 0^+} \left( U_2(\mathbf{p} + \delta \mathbf{n}_p) - U_2(\mathbf{p} - \delta \mathbf{n}_p) \right) = 4\pi \varpi(\mathbf{p}). \quad (3.47a)$$

- The first derivative is continuous in the direction of the surface normal.

$$\lim_{\delta \rightarrow 0^+} \left( \mathbf{n}_p \cdot \nabla U_2 \Big|_{\mathbf{p} + \delta \mathbf{n}_p} - \mathbf{n}_p \cdot \nabla U_2 \Big|_{\mathbf{p} - \delta \mathbf{n}_p} \right) = 0 \quad (3.47b)$$

- Like  $U_1$ , the potential satisfies Laplace's equation inside and outside of the cavity.

$$\nabla \cdot \nabla U_2 = 0 \quad (3.47c)$$

From the above properties it is immediately clear that  $U_2$  is ideally suited to fulfill the necessary boundary conditions, Eqs. (3.45a) and (3.45b). In summary, this means that the outlying-charge-error-free potential  $\Phi_p^{\text{MPE}}$  cannot be exactly represented by any ASC method but instead an apparent surface dipole (ASD) model needs to be developed.

### 3.4 Non-Electrostatic Interactions

As outlined before in section 3.1.2, many approximations have entered in the electrostatic solvation model. Although the so-called non-electrostatic correction terms that will be briefly discussed in this section are not meant to correct for those approximations, they usually contribute a few to many more fitting parameters to the whole implicit solvation model which also help to improve on the electrostatic description. The actual reason, however, that makes these corrections necessary is the lack of explicit exchange and correlation interaction between the solute's and solvent molecules' electrons—as has been pointed out in the introduction of this chapter. Obviously, the true interaction can never be fully recovered as the core benefit of implicit models lies in the elimination of solvent degrees of freedom that would enter the exact expressions. The correction terms are thus usually of rather phenomenological nature, such as the in literature omnipresent splitting of the “total” non-electrostatic free energy change  $\Delta G_{\text{ne}}$ —the reference being thereby the

unperturbed liquid in equilibrium state and the solute *in vacuo*—into the following parts [16]:

$$\Delta G_{\text{ne}} = G_{\text{cav}} + G_{\text{rep}} + G_{\text{dis}} + \Delta G_{\text{tm}} + p\Delta V \quad (3.48)$$

$G_{\text{cav}}$  is the energy needed to form the solvation cavity in the formerly unperturbed solvent bulk. The free energy connected with the transfer of the solute into this cavity is then partially determined by electrostatics, cf. Eq. (3.19). The missing parts are grouped into

$G_{\text{rep}}$  being repulsion and

$G_{\text{dis}}$  dispersion interactions between solute and solvent.

$\Delta G_{\text{tm}}$  accounts for a change in thermal motion of the solute’s nuclei, i.e., the influence on rotations and vibrations of the solute. Finally,

$p\Delta V$  measures the work related to volume changes. However, for most liquids incompressibility is safe to assume so that this term is usually ignored and the Gibbs and Helmholtz free energies are equal.

Especially for the first three terms— $G_{\text{cav}}$ ,  $G_{\text{rep}}$ , and  $G_{\text{dis}}$ —a plethora of more or less sophisticated models have been developed, most of them being simple scalar energy post-corrections while some modifying the solute’s Hamiltonian in a more complex way. We do not report those methods here and instead refer the interested reader to dedicated review articles [16, 61].

Instead, it should be pointed out that extremely simplified models have been reported in literature that reach remarkable agreement with experimental solvation free energies approximating the above non-electrostatic terms by a simple linear relation to the (“quantum”) surface,  $O_{\text{solute}}$ , of the solute [62],

$$\Delta G_{\text{ne}} \approx \alpha O_{\text{solute}} , \quad (3.49a)$$

or a sum of linear surface and (“quantum”) volume,  $V_{\text{solute}}$ , terms [21],

$$\Delta G_{\text{ne}} \approx \alpha O_{\text{solute}} + \beta V_{\text{solute}} . \quad (3.49b)$$

Thereby,  $\alpha$  and  $\beta$  are effective parameters that need to be fitted, e.g., to experimental measurements or explicit theoretical calculations.

The total solvation free energy  $\Delta G_{\text{sol}}$ , which is the sum of electrostatic and non-electrostatic contributions, can then be expressed as

$$\Delta G_{\text{sol}} = \Delta G_{\text{el}} + \alpha O_{\text{solute}} + \beta V_{\text{solute}} \quad (3.50)$$

Methods to calculate  $O_{\text{solute}}$  and  $V_{\text{solute}}$  will be discussed in section 3.5.

### 3.5 Cavity Definition

As already alluded to above, there is no unique way of defining the dielectric function  $\epsilon$  in the electrostatic problem. The physical idea behind the shape of  $\epsilon$  is to separate the volume occupied by the solute from the one occupied by the solvent since self-screening of the solute’s charge

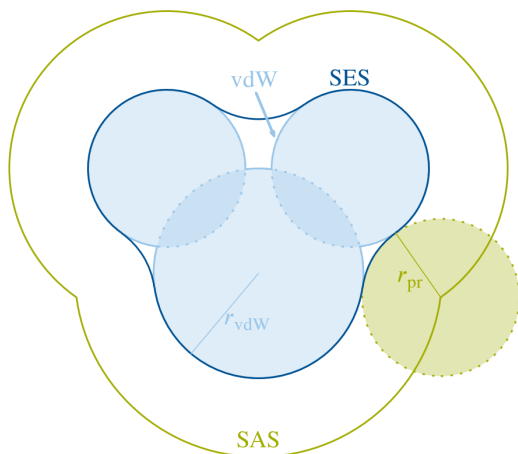


Fig. 3.2: Schematic picture of different surface definitions for the cavity. The spheres around the solute’s atoms with a van der Waals (vdW) radius  $r_{\text{vdW}}$  (shaded in blue) are bordered by a dashed blue line. The surface of the superposition of those spheres (marked by a solid blue line) is called vdW surface. Rolling a spherical probe of radius  $r_{\text{pr}}$  (shaded in green and bordered by a dashed green line) on the solute’s surface—i.e., the probe is always in contact with the vdW surface but does not intersect with the vdW volume—leads to another two surface definitions. The solvent-accessible surface (SAS) is given by all possible positions of the probe’s center (solid green line) whereas the solvent-excluded surface (SES) is defined as the set of closest points to the solute (solid dark blue line).

density is included in the former ( $\epsilon = 1$ ) while electrostatic screening due to the solvent needs to be modeled implicitly in the latter ( $\epsilon = \epsilon_b$ ). This naturally leads to the picture of a cavity within the solvent in which the solute resides—especially when a step-like transition function is used.

Similar to the different electrostatic models there is also a number of methods to define such a cavity. The simplest model is that of overlapping hard spheres around all nuclei with certain van der Waals (vdW) radii—as, e.g., defined by Bondi [63] or Pauling [64]. This is related to the idea behind the GB model introduced earlier in section 3.3. However, even in the GB with accessible surface area approach [65] the surface area used to calculate non-electrostatic contributions (similar to Eq. (3.49a) but with atomic surfaces and parameters) is not just the total surface area of the overlapping spheres. Instead, a concept called solvent-accessible surface (SAS) is introduced, i.e., the surface that is defined by all possible positions of the center of a spherical probe in close contact with at least one of the spheres—as illustrated in Fig. 3.2. Other models instead use the solvent-excluded surface (SES)—also called Connolly surface [66]—or a convex realization thereof [67].

A conceptually different type of cavity can be defined based on the electron density of the system [62, 68]. Physically, this is motivated by the repulsive interaction between the solute’s and the solvent molecules’ electron densities at close distances. Since the electron density is intrinsically smooth over the whole volume, the cavity can be defined as its isosurface with respect to a given iso-density value  $\rho_{\text{iso}}$ . In contrast to the potentially huge number of atomic radii that locally determine the extent of the cavity,  $\rho_{\text{iso}}$  acts globally on the solute cavity as a single parameter. This means that the model parametrization is much easier for an iso-density

cavity with a drastically reduced number of adjustable degrees of freedom.

Recently, the idea of the isodensity surface has been combined with the hard-sphere model. The resulting soft-sphere cavity [69] is still based on atomic spheres. Instead of a certain radius, however, these spheres are defined as continuous functions and can be simply multiplied with each other to define the total cavity. Although originally developed for a continuous cavity, this model can easily be transferred back to a discrete cavity which is simply defined by an isosurface on the cavity generation function.





## 4 MPE Method ‡

### 4.1 Discretization of the MPE Equations

In section 3.3.3, we have already derived the central electrostatic equations for the MPE model, Eqs. (3.45a) and (3.45b). These are already written in such a way that the unknown potential terms,  $\Phi_R$  and  $\Phi_Q$ , are collected on the left side of the equation while the already known Hartree potential  $\Phi_H$ , i.e. the potential *in vacuo*, is placed on the right side. In order to solve these equations, a boundary collocation method is used for which the problem is discretized in two ways.

#### 4.1.1 Truncated Multipole Expansion

First,  $\Phi_R$  and  $\Phi_Q$  are expanded in a series of solid harmonics which have been introduced earlier, Eqs. (3.38a) and (3.38b). For the following derivations, all of those expansion centers are required to be situated within the cavity—as illustrated in Fig. 4.1. Since an expansion in irregular solid harmonics would introduce unphysical singularities within the cavity, regular solid harmonics have to be used for  $\Phi_R$ . In contrast, the potential  $\Phi_Q$  outside of the cavity is required to decay to zero, cf. Eq. (3.23), which can only be fulfilled by irregular and not by regular solid harmonics. With both potentials being the solution to Laplace’s equation, both expansions are exact yet potentially infinite. For practical reasons, the expansions thus need to be truncated, which can easily be achieved in a controlled manner by restricting the expansion order  $l$  of the solid harmonic functions to a certain maximum value— $l_{\max,R}$  for  $\Phi_R$  and  $l_{\max,Q}$  for  $\Phi_Q$ .

$$\Phi_R(\mathbf{r}) = \sum_{l=0}^{l_{\max,R}} \sum_{m=-l}^l R_K^{(l,m)} \mathcal{R}_m^l(\mathbf{r} - \mathbf{r}_K) \quad (4.1a)$$

$$\Phi_Q(\mathbf{r}) = \sum_{J=1}^N \sum_{l=0}^{l_{\max,Q}} \sum_{m=-l}^l Q_J^{(l,m)} \mathcal{I}_m^l(\mathbf{r} - \mathbf{r}_J) \quad (4.1b)$$

Notice how Eq. (4.1b) is an expansion at multiple ( $N$ , to be precise) centers with index  $J$  positioned at the coordinates  $\mathbf{r}_J$ . This technique allows to drastically reduce the necessary expansion order  $l_{\max,Q}$  as every new center with irregular solid harmonic functions contributes new degrees of freedom to the expansion. In the case of Eq. (4.1a), however, this trick is not applicable due to the translational properties of regular solid harmonics [70] which allow to exactly represent the given expansion at center  $K$  by an expansion of the same order at a different center  $K'$ . In other words, the expansion at center  $K'$  does not contribute any new degrees of freedom as its functions can be exactly described by a linear combination of the existing regular solid harmonics at center  $K$ .

For the sake of simplicity, the same order  $l_{\max,Q}$  is chosen for all expansion centers  $J$  in  $\Phi_Q$ ,

‡Reprinted in parts with permission from Ref. [1]. © 2017 American Chemical Society.

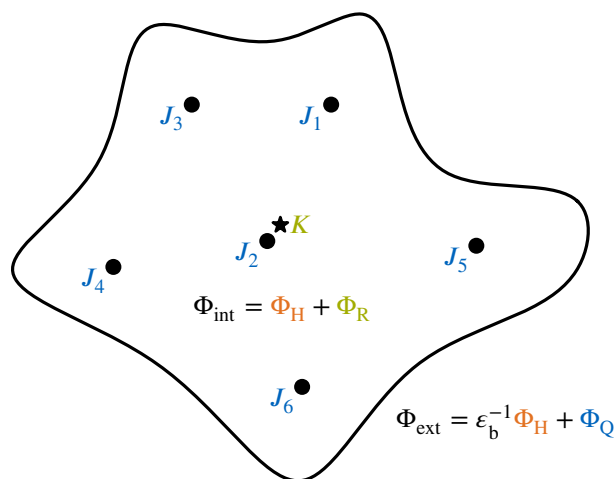


Fig. 4.1: Schematic picture of the cavity surface together with the expansion centers used to express the potentials  $\Phi_Q$  and  $\Phi_R$ . Adapted with permission from Ref. [1]. © 2017 American Chemical Society.

and those centers are placed on the positions of the nuclei. It should be noted, however, that this choice is not at all unique and most probably also not well suited for applications on larger systems than the ones discussed in this work. This choice, however, makes Eq. (4.1b) look very similar to the multipole expanded form of the Hartree potential  $\Phi_H$  as provided by FHI-aims—as shown in section 4.4.1. The position of center  $K$  for  $\Phi_R$  is in principle arbitrary—again due to the translational properties of regular harmonics. Nonetheless, placing it somewhere central in the cavity can be advantageous for reasons of numerical stability.

In total, the expansion outlined above include a total of

$$n_A = \underbrace{(l_{\max,R} + 1)^2}_{n_R} + N \underbrace{(l_{\max,Q} + 1)^2}_{n_Q} \quad (4.2)$$

basis functions with  $n_R$  expansion coefficients assigned to  $\Phi_R$  and  $n_Q$  to  $\Phi_Q$ .

Skipping far ahead to an application of the complete model for small organic molecules (for more information, please see chapter 6), we can observe its convergence behavior with respect to the mentioned maximum expansion levels in Fig. 4.2. The convergence test, indeed, shows the effect of the multi-center expansion, i.e.,  $l_{\max,Q}$  can often be chosen much lower than  $l_{\max,R}$  without compromising the accuracy of the results.

#### 4.1.2 Cavity Discretization

The second discretization step is connected to the fact that the boundary conditions are valid at any point  $\mathbf{p}$  on the implicit solvent cavity, i.e.  $\mathcal{C}(\mathbf{p}) = 0$ . Having reduced the problem to determining  $n_A$  unknown coefficients, cf. Eq. (4.2), it is sufficient to evaluate the MPE equations, Eqs. (3.45a) and (3.45b), at a finite number of such points  $\mathbf{p}$ . Assuming  $M$  points are picked, a total number of

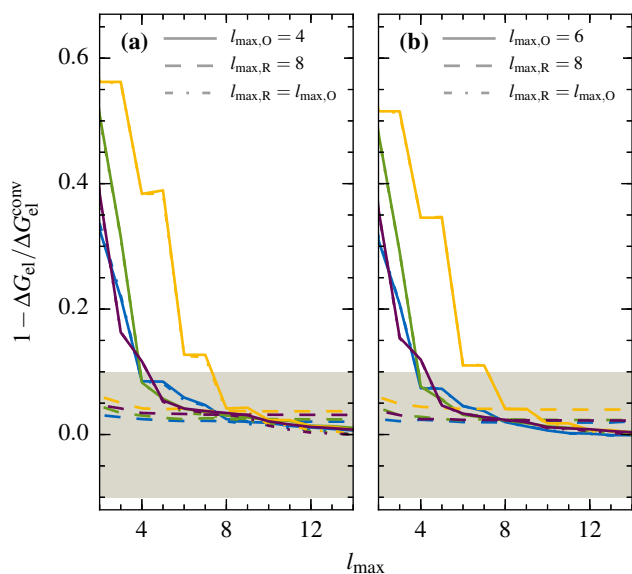


Fig. 4.2: Relative deviation of the calculated electrostatic solvation free energy,  $\Delta G_{\text{el}}$ , with respect to the value obtained for the largest employed expansion orders,  $\Delta G_{\text{el}}^{\text{conv}}$ , i.e.  $l_{\text{max,R}} = 14$  for  $\Phi_{\text{R}}$  and  $l_{\text{max,Q}} = 14$  for  $\Phi_{\text{Q}}$ , as a function of electrostatic potential expansion order  $l_{\text{max}}$  for three different cases: variation of  $l_{\text{max}} = l_{\text{max,R}}$  at a fixed expansion order for  $\Phi_{\text{Q}}$  (solid lines), variation of  $l_{\text{max}} = l_{\text{max,Q}}$  at a fixed expansion order for  $\Phi_{\text{R}}$  (dashed lines), and variation of expansion order of  $\Phi_{\text{R}}$  and  $\Phi_{\text{Q}}$  at the same time,  $l_{\text{max}} = l_{\text{max,R}} = l_{\text{max,Q}}$  (dash-dotted lines). Results are calculated with the PBE functional at **(a)** light and **(b)** tight integration grid settings for four randomly selected molecules out of the test-set T1 presented in section 6.1: biphenyl (chemical formula  $\text{C}_{12}\text{H}_{10}$ , drawn in blue), morpholine ( $\text{C}_4\text{H}_9\text{NO}$ , green), diethyl disulfide ( $\text{C}_4\text{H}_{10}\text{S}_2$ , yellow), and 1,3-dioxolane ( $\text{C}_3\text{H}_6\text{O}_2$ , purple). In all of these cases,  $\Delta G_{\text{el}}^{\text{conv}}$  is in the range of  $-0.32$  eV to  $-0.23$  eV. The shaded areas indicate an absolute deviation from  $\Delta G_{\text{el}}^{\text{conv}}$  of 10% or less. Reprinted with permission from Ref. [1]. © 2017 American Chemical Society.

$m_A = 2M$  equations are obtained:

$$\begin{aligned}
\Phi_R(\mathbf{p}_1) - \Phi_Q(\mathbf{p}_1) &= (\varepsilon_b^{-1} - 1) \Phi_H(\mathbf{p}_1) \\
\mathbf{n}_{\mathbf{p}_1} \cdot \nabla \Phi_R(\mathbf{p}_1) - \mathbf{n}_{\mathbf{p}_1} \cdot \varepsilon_b \nabla \Phi_Q(\mathbf{p}_1) &= 0 \\
\Phi_R(\mathbf{p}_2) - \Phi_Q(\mathbf{p}_2) &= (\varepsilon_b^{-1} - 1) \Phi_H(\mathbf{p}_2) \\
\mathbf{n}_{\mathbf{p}_2} \cdot \nabla \Phi_R(\mathbf{p}_2) - \mathbf{n}_{\mathbf{p}_2} \cdot \varepsilon_b \nabla \Phi_Q(\mathbf{p}_2) &= 0 \\
&\vdots \\
\Phi_R(\mathbf{p}_M) - \Phi_Q(\mathbf{p}_M) &= (\varepsilon_b^{-1} - 1) \Phi_H(\mathbf{p}_M) \\
\mathbf{n}_{\mathbf{p}_M} \cdot \nabla \Phi_R(\mathbf{p}_M) - \mathbf{n}_{\mathbf{p}_M} \cdot \varepsilon_b \nabla \Phi_Q(\mathbf{p}_M) &= 0
\end{aligned} \tag{4.3}$$

Assuming furthermore that all of the above equations are linearly independent, the number of equations,  $m_A$ , needs to match the number of unknowns  $n_A$ , i.e. potential expansion coefficients, such that the system of linear equations (SLE) can be solved exactly. This can also be expressed in the degree of determination,

$$d_{\text{det}} = \frac{m_A}{n_A}, \tag{4.4}$$

which is the ratio of conditions and variables in the SLE. Ideally,  $d_{\text{det}}$  equals 1. In reality, however, it could easily happen that some equations are linearly dependent and, according to the Rouché-Capelli theorem [71], this means no unique solution exists. To prevent this, additional points need to be added until the SLE is again determined, i.e. the number of *independent* equations  $m_A^{\text{red}}$  matches the number of unknowns.

Obviously, this could be realized by incrementally adding new points and checking the state of the SLE. New points, however, should be placed such that the cavity sampling remains homogeneous, i.e. the points should be distributed rather evenly on the surface, which could render this procedure rather tedious when applied in a strict manner. On the other hand, it would allow very fine control over the exact determination of the SLE. A much easier approach is to initialize a larger amount of points directly from the start—hoping that the resulting SLE is at least determined or, preferably, over-determined. In this case, however, the true degree of determination will be less than  $d_{\text{det}}$ .

$$d_{\text{det}}^{\text{true}} = \frac{m_A^{\text{red}}}{n_A} \leq \frac{m_A}{n_A} = d_{\text{det}} \tag{4.5}$$

Lacking an efficient, easy and—most importantly—general relationship between  $m_A$  and  $m_A^{\text{red}}$ , the value of  $d_{\text{det}}$  is exposed as a target value to the model and inversely used to estimate the required number  $M$  of points on the cavity for the known number of variables.

$$m_A = d_{\text{det}} n_A = 2M \tag{4.6}$$

How this can actually be achieved is covered in more detail in section 5.1. As illustrated in Fig. 4.3, the results of the full model converge very rapidly with  $d_{\text{det}}$  such that a target value of around 2 to 3 seems to be a safe choice.

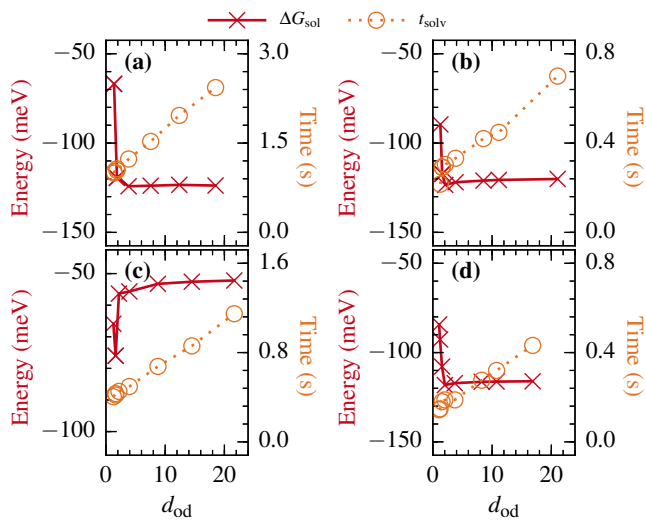


Fig. 4.3: Convergence behavior of the root finding problem with respect to the degree of determination,  $d_{\text{det}}$ , of the MPE equations, i.e. the ratio of number of conditions and variables in the SLE, for four test molecules **(a)** biphenyl ( $\text{C}_{12}\text{H}_{10}$ ), **(b)** butanal ( $\text{C}_4\text{H}_8\text{O}$ ), **(c)** diethyl disulfide ( $\text{C}_4\text{H}_{10}\text{S}_2$ ), and **(d)** 1,3-dioxolane ( $\text{C}_3\text{H}_6\text{O}_2$ ) (see also section 6.1). Overall solvation energies  $\Delta G_{\text{sol}}$  are marked as red crosses. Orange circles depict the time  $t_{\text{solv}}$  necessary to set up and solve the MPE equations using four parallel MPI tasks running on an Intel i5-4670 CPU. Reprinted with permission from Ref. [1]. © 2017 American Chemical Society.

## 4.2 Formulation as Linear Algebra Problem

Inserting the potential expansion formulas, Eqs. (4.1a) and (4.1b), into the discretized boundary conditions on the cavity, Eq. (4.3), yields the set of working equations for the MPE model.

$$\begin{aligned}
\sum_{l,m} R_K^{(l,m)} \mathcal{R}_m^l(\mathbf{p}_{1,K}) - \sum_{J,l,m} Q_J^{(l,m)} \mathcal{I}_m^l(\mathbf{p}_{1,J}) &= (\varepsilon_b^{-1} - 1) \Phi_H(\mathbf{p}_1) \\
\sum_{l,m} R_K^{(l,m)} \mathbf{n}_{\mathbf{p}_1} \cdot \nabla \mathcal{R}_m^l(\mathbf{p}_{1,K}) - \sum_{J,l,m} Q_J^{(l,m)} \mathbf{n}_{\mathbf{p}_1} \cdot \varepsilon_b \nabla \mathcal{I}_m^l(\mathbf{p}_{1,J}) &= 0 \\
\sum_{l,m} R_K^{(l,m)} \mathcal{R}_m^l(\mathbf{p}_{2,K}) - \sum_{J,l,m} Q_J^{(l,m)} \mathcal{I}_m^l(\mathbf{p}_{2,J}) &= (\varepsilon_b^{-1} - 1) \Phi_H(\mathbf{p}_2) \\
\sum_{l,m} R_K^{(l,m)} \mathbf{n}_{\mathbf{p}_2} \cdot \nabla \mathcal{R}_m^l(\mathbf{p}_{2,K}) - \sum_{J,l,m} Q_J^{(l,m)} \mathbf{n}_{\mathbf{p}_2} \cdot \varepsilon_b \nabla \mathcal{I}_m^l(\mathbf{p}_{2,J}) &= 0 \\
&\vdots && \vdots && \vdots \\
\sum_{l,m} R_K^{(l,m)} \mathcal{R}_m^l(\mathbf{p}_{M,K}) - \sum_{J,l,m} Q_J^{(l,m)} \mathcal{I}_m^l(\mathbf{p}_{M,J}) &= (\varepsilon_b^{-1} - 1) \Phi_H(\mathbf{p}_M) \\
\sum_{l,m} R_K^{(l,m)} \mathbf{n}_{\mathbf{p}_M} \cdot \nabla \mathcal{R}_m^l(\mathbf{p}_{M,K}) - \sum_{J,l,m} Q_J^{(l,m)} \mathbf{n}_{\mathbf{p}_M} \cdot \varepsilon_b \nabla \mathcal{I}_m^l(\mathbf{p}_{M,J}) &= 0
\end{aligned} \tag{4.7}$$

where  $\mathbf{p}_{i,K}$  is the distance vector between  $\mathbf{p}_i$  and the expansion center  $K$ 's coordinates  $\mathbf{r}_K$ , e.g.

$$\mathbf{p}_{2,J} = \mathbf{p}_2 - \mathbf{r}_J. \tag{4.8}$$

Rewriting Eq. (4.7) as an inner product representation yields (note the matrix and vector transpositions)

$$\begin{pmatrix}
\mathcal{R}_0^0(\mathbf{p}_{1,K}) & \mathbf{n}_{\mathbf{p}_1} \cdot \nabla \mathcal{R}_0^0(\mathbf{p}_{1,K}) & \mathcal{R}_0^0(\mathbf{p}_{2,K}) & \mathbf{n}_{\mathbf{p}_2} \cdot \nabla \mathcal{R}_0^0(\mathbf{p}_{2,K}) & \dots \\
\mathcal{R}_{-1}^1(\mathbf{p}_{1,K}) & \mathbf{n}_{\mathbf{p}_1} \cdot \nabla \mathcal{R}_{-1}^1(\mathbf{p}_{1,K}) & \mathcal{R}_{-1}^1(\mathbf{p}_{2,K}) & \mathbf{n}_{\mathbf{p}_2} \cdot \nabla \mathcal{R}_{-1}^1(\mathbf{p}_{2,K}) & \dots \\
\mathcal{R}_0^1(\mathbf{p}_{1,K}) & \mathbf{n}_{\mathbf{p}_1} \cdot \nabla \mathcal{R}_0^1(\mathbf{p}_{1,K}) & \mathcal{R}_0^1(\mathbf{p}_{2,K}) & \mathbf{n}_{\mathbf{p}_2} \cdot \nabla \mathcal{R}_0^1(\mathbf{p}_{2,K}) & \dots \\
\vdots & \vdots & \vdots & \vdots & \dots \\
-\mathcal{I}_0^0(\mathbf{p}_{1,J_1}) & -\mathbf{n}_{\mathbf{p}_1} \cdot \varepsilon_b \nabla \mathcal{I}_0^0(\mathbf{p}_{1,J_1}) & -\mathcal{I}_0^0(\mathbf{p}_{2,J_1}) & -\mathbf{n}_{\mathbf{p}_2} \cdot \varepsilon_b \nabla \mathcal{I}_0^0(\mathbf{p}_{2,J_1}) & \dots \\
-\mathcal{I}_{-1}^1(\mathbf{p}_{1,J_1}) & -\mathbf{n}_{\mathbf{p}_1} \cdot \varepsilon_b \nabla \mathcal{I}_{-1}^1(\mathbf{p}_{1,J_1}) & -\mathcal{I}_{-1}^1(\mathbf{p}_{2,J_1}) & -\mathbf{n}_{\mathbf{p}_2} \cdot \varepsilon_b \nabla \mathcal{I}_{-1}^1(\mathbf{p}_{2,J_1}) & \dots \\
\vdots & \vdots & \vdots & \vdots & \dots \\
-\mathcal{I}_0^0(\mathbf{p}_{1,J_2}) & -\mathbf{n}_{\mathbf{p}_1} \cdot \varepsilon_b \nabla \mathcal{I}_0^0(\mathbf{p}_{1,J_2}) & -\mathcal{I}_0^0(\mathbf{p}_{2,J_2}) & -\mathbf{n}_{\mathbf{p}_2} \cdot \varepsilon_b \nabla \mathcal{I}_0^0(\mathbf{p}_{2,J_2}) & \dots \\
-\mathcal{I}_{-1}^1(\mathbf{p}_{1,J_2}) & -\mathbf{n}_{\mathbf{p}_1} \cdot \varepsilon_b \nabla \mathcal{I}_{-1}^1(\mathbf{p}_{1,J_2}) & -\mathcal{I}_{-1}^1(\mathbf{p}_{2,J_2}) & -\mathbf{n}_{\mathbf{p}_2} \cdot \varepsilon_b \nabla \mathcal{I}_{-1}^1(\mathbf{p}_{2,J_2}) & \dots \\
\vdots & \vdots & \vdots & \vdots & \ddots
\end{pmatrix}^T \cdot \begin{pmatrix} R_K^{(0,0)} \\ R_K^{(1,-1)} \\ R_K^{(1,0)} \\ \vdots \\ Q_{J_1}^{(0,0)} \\ Q_{J_1}^{(1,-1)} \\ \vdots \\ Q_{J_2}^{(0,0)} \\ Q_{J_2}^{(1,-1)} \\ \vdots \end{pmatrix} = \begin{pmatrix} (\varepsilon_b^{-1} - 1) \Phi_H(\mathbf{p}_1) & 0 & (\varepsilon_b^{-1} - 1) \Phi_H(\mathbf{p}_2) & 0 & \dots \end{pmatrix}^T, \tag{4.9}$$

which can be expressed in the simplified linear algebra form

$$\underline{\mathbf{A}}\mathbf{c} = \mathbf{b} \quad (4.10)$$

with an  $(m_A \times n_A)$  (cf. Eqs. (4.2) and (4.6)) basis set matrix  $\underline{\mathbf{A}}$ , the vector of unknown expansion coefficients  $\mathbf{c}$ , and a right hand side of measurements  $\mathbf{b}$ .

#### 4.2.1 Matrix Factorization and Solution

As mentioned before, the number of sampling points is chosen such that the SLE is over-determined and that it can be solved in a linear least squares manner, i.e., the best solution  $\tilde{\mathbf{c}}$  needs to be determined which minimizes the residual  $\mathcal{F}$ .

$$\tilde{\mathbf{c}} = \arg \min_{\mathbf{c}} \mathcal{F}(\mathbf{c}) = \arg \min_{\mathbf{c}} \|\underline{\mathbf{A}}\mathbf{c} - \mathbf{b}\|_2 \quad (4.11)$$

This residual is defined as the  $l^2$ -norm of the difference between left and right hand side for a given coefficient vector  $\mathbf{c}$ . The minimization problem can formally be rewritten as a system of normal equations,

$$\underline{\mathbf{A}}^T \underline{\mathbf{A}} \tilde{\mathbf{c}} = \underline{\mathbf{A}}^T \mathbf{b}, \quad (4.12)$$

where  $\underline{\mathbf{A}}^T \underline{\mathbf{A}}$  is an  $(n_A \times n_A)$  square matrix also called the Gramian of  $\underline{\mathbf{A}}$ . Given that the columns of  $\underline{\mathbf{A}}$  are linearly independent, i.e.,  $\underline{\mathbf{A}}$  has full (column) rank, the Gramian matrix is positive definite and thus invertible such that the solution to the problem could be calculated as

$$\tilde{\mathbf{c}} = (\underline{\mathbf{A}}^T \underline{\mathbf{A}})^{-1} \underline{\mathbf{A}}^T \mathbf{b}. \quad (4.13)$$

In practice, however, this approach is neither efficient nor stable. The set of normal equations never needs to be explicitly calculated, but rather serves as a stepping-stone towards numerically much more stable approaches.

A long accepted method in order to solve a general set of linear equations is to factorize the  $(m_A \times n_A)$  coefficient matrix  $\underline{\mathbf{A}}$ ,

$$\underline{\mathbf{A}} = \underline{\mathbf{Q}}\underline{\mathbf{R}}. \quad (4.14)$$

to obtain an orthogonal  $(m_A \times m_A)$  square matrix  $\underline{\mathbf{Q}}$  and an  $(m_A \times n_A)$  matrix  $\underline{\mathbf{R}}$  with upper triangular form. More specifically, this means that all entries below the upper diagonal of  $\underline{\mathbf{R}}$  are zero, i.e.,

$$\underline{\mathbf{R}} = \begin{pmatrix} R_{11} & R_{12} & R_{13} & \dots & R_{1n_A} \\ 0 & R_{22} & R_{23} & \dots & R_{2n_A} \\ 0 & 0 & R_{33} & \dots & R_{3n_A} \\ 0 & 0 & 0 & \ddots & \vdots \\ 0 & 0 & 0 & 0 & R_{n_A n_A} \\ 0 & 0 & 0 & 0 & 0 \\ \vdots & \vdots & \vdots & \vdots & \vdots \end{pmatrix}, \quad (4.15)$$



which can also be written in terms of an upper triangular ( $n_A \times n_A$ ) square matrix  $\tilde{\mathbf{R}}$  padded by a matrix of zeros,

$$\underline{\mathbf{R}} = \begin{pmatrix} \tilde{\mathbf{R}} \\ \underline{\mathbf{0}} \end{pmatrix}. \quad (4.16)$$

Inserting this into Eq. (4.14) reveals that only the first  $n_A$  columns of  $\underline{\mathbf{Q}}$ —which we collect in the ( $m_A \times n_A$ ) matrix  $\tilde{\mathbf{Q}}$ —are required to form the reduced QR-decomposition of  $\underline{\mathbf{A}}$ ,

$$\underline{\mathbf{A}} = \tilde{\mathbf{Q}}\tilde{\mathbf{R}}. \quad (4.17)$$

It should be noted here that, while the columns of the reduced matrix  $\tilde{\mathbf{Q}}$  are still orthogonal, the rows in general are not, i.e.

$$\tilde{\mathbf{Q}}^T \tilde{\mathbf{Q}} = \underline{\mathbf{1}}_{n_A}, \quad \tilde{\mathbf{Q}}\tilde{\mathbf{Q}}^T \neq \underline{\mathbf{1}}_{m_A}, \quad (4.18)$$

with  $\underline{\mathbf{1}}_k$  being the ( $k \times k$ ) unity matrix.

Inserting Eq. (4.17) into Eq. (4.12) yields

$$\left( \tilde{\mathbf{Q}}\tilde{\mathbf{R}} \right)^T \tilde{\mathbf{Q}}\tilde{\mathbf{R}}\tilde{\mathbf{c}} = \left( \tilde{\mathbf{Q}}\tilde{\mathbf{R}} \right)^T \mathbf{b}, \quad (4.19)$$

which can be reduced to

$$\tilde{\mathbf{R}}^T \tilde{\mathbf{R}}\tilde{\mathbf{c}} = \tilde{\mathbf{R}}^T \tilde{\mathbf{Q}}^T \mathbf{b}, \quad (4.20)$$

using the relation  $\left( \tilde{\mathbf{Q}}\tilde{\mathbf{R}} \right)^T = \tilde{\mathbf{R}}^T \tilde{\mathbf{Q}}^T$  and the orthogonality properties of  $\tilde{\mathbf{Q}}$  noted above. Since multiplication with an orthogonal matrix is a norm preserving operation, the conditioning of the system of equations remains unchanged. Provided that  $\tilde{\mathbf{R}}^T$  is invertible—i.e.  $\tilde{\mathbf{R}}$  and thus also  $\underline{\mathbf{A}}$  have full rank—the least-squares solution  $\tilde{\mathbf{c}}$  to Eq. (4.20) can simply be found by backward substitution due to the triangular shape of  $\tilde{\mathbf{R}}$ ,

$$\tilde{\mathbf{R}}\tilde{\mathbf{c}} = \tilde{\mathbf{Q}}^T \mathbf{b}. \quad (4.21)$$

Using one of the widely available factorization algorithms—such as e.g. the Gram-Schmidt, Givens or Householder methods [72]—QR-decomposition can thus be a straightforward and exact approach to solving linear least-squares problems as occurring in the MPE solvation model.

Unfortunately,  $\tilde{\mathbf{R}}$  can and is actually sometimes found to be rank-deficient even when enough measurements were available ( $m_A \gg n_A$ ). This happens especially for very large expansion orders of the solid harmonic functions that enter  $\underline{\mathbf{A}}$  when no point on the cavity can be found that would allow to *numerically* distinguish two or more basis functions—although they are in principle all linearly independent—such that  $\underline{\mathbf{A}}$  becomes numerically rank-deficient. A numerically more robust way of solving Eq. (4.20) is thus to further factorize  $\tilde{\mathbf{R}}$  using a singular value decomposition (SVD),

$$\tilde{\mathbf{R}} = \tilde{\mathbf{U}}\tilde{\mathbf{\Sigma}}\tilde{\mathbf{V}}^T, \quad (4.22)$$

into the orthogonal ( $n_A \times n_A$ ) matrices  $\underline{\tilde{\mathbf{U}}}$  and  $\underline{\mathbf{V}}$ , and the ( $n_A \times n_A$ ) diagonal matrix  $\underline{\tilde{\Sigma}}$  containing the non-negative singular values sorted in descending order, i.e.

$$\tilde{\Sigma}_{11} \geq \tilde{\Sigma}_{22} \geq \dots \geq \tilde{\Sigma}_{n_A n_A} \geq 0. \quad (4.23)$$

Alternatively, the SVD can directly be applied to  $\underline{\mathbf{A}}$ ,

$$\underline{\mathbf{A}} = \underline{\tilde{\mathbf{W}}} \underline{\tilde{\Sigma}} \underline{\mathbf{V}}^T, \quad (4.24)$$

where we already assumed the reduced (sometimes also called thin) form of the SVD with an ( $m_A \times n_A$ ) matrix  $\underline{\tilde{\mathbf{W}}}$  with the same orthogonality properties as  $\underline{\tilde{\mathbf{Q}}}$ , Eq. (4.18). In fact, it is straightforward to see that  $\underline{\tilde{\mathbf{W}}}$  is simply  $\underline{\tilde{\mathbf{Q}}}\underline{\tilde{\mathbf{U}}}$  and

$$\underline{\mathbf{A}} = \underline{\tilde{\mathbf{Q}}}\underline{\tilde{\mathbf{U}}}\underline{\tilde{\Sigma}}\underline{\mathbf{V}}^T. \quad (4.25)$$

While both approaches yield equivalent results, the computational effort can be quite different. The additional cost of the QR-decomposition to obtain  $\underline{\tilde{\mathbf{R}}}$  can pay off by reducing the size of the matrix operated on for the SVD from ( $m_A \times n_A$ ) to ( $n_A \times n_A$ ). According to the LAPACK reference implementation [73], current algorithms reach this crossover point already at  $m_A \geq 1.6n_A$  which is typically exceeded by the coefficient matrices occurring in the MPE model (cf. Fig. 4.3).

Inserting Eq. (4.22) into Eq. (4.20) leads to

$$\underline{\mathbf{V}}\underline{\tilde{\Sigma}}^T \underline{\tilde{\mathbf{U}}}^T \underline{\tilde{\mathbf{U}}}\underline{\tilde{\Sigma}}\underline{\mathbf{V}}^T \tilde{\mathbf{c}} = \underline{\mathbf{V}}\underline{\tilde{\Sigma}}^T \left( \underline{\tilde{\mathbf{Q}}}\underline{\tilde{\mathbf{U}}} \right)^T \mathbf{b}, \quad (4.26)$$

which can be simplified by trivially inverting the orthogonal matrix  $\underline{\mathbf{V}}$  and using the orthogonality properties of  $\underline{\tilde{\mathbf{U}}}$ ,

$$\underline{\tilde{\Sigma}}^T \underline{\tilde{\Sigma}}\underline{\mathbf{V}}^T \tilde{\mathbf{c}} = \underline{\tilde{\Sigma}}^T \left( \underline{\tilde{\mathbf{Q}}}\underline{\tilde{\mathbf{U}}} \right)^T \mathbf{b}. \quad (4.27)$$

This reduces the problem to finding the inverse of the diagonal matrix  $\underline{\tilde{\Sigma}} = \underline{\tilde{\Sigma}}^T$  which is only defined if the diagonal of  $\underline{\tilde{\Sigma}}$  contains only numerically non-zero values, meaning that  $\underline{\mathbf{A}}$  has full rank. Nonetheless, also for rank-deficient problems it is possible to find the unique solution [72],

$$\tilde{\mathbf{c}} = \underline{\mathbf{V}}\underline{\tilde{\Sigma}}^\dagger \left( \underline{\tilde{\mathbf{Q}}}\underline{\tilde{\mathbf{U}}} \right)^T \mathbf{b}, \quad (4.28)$$

by defining the pseudoinverse  $\underline{\tilde{\Sigma}}^\dagger$  of  $\underline{\tilde{\Sigma}}$  (and thus also of  $\underline{\tilde{\Sigma}}^T$ ) as diagonal matrix with the entries  $\tilde{\Sigma}_{ii}^\dagger$ ,

$$\tilde{\Sigma}_{ii}^\dagger = \begin{cases} 1/\tilde{\Sigma}_{ii}, & \tilde{\Sigma}_{ii} > \delta \\ 0, & \tilde{\Sigma}_{ii} \leq \delta \end{cases}, \quad \delta \geq 0. \quad (4.29)$$

The positive threshold  $\delta$  used here is usually related to the largest singular value  $\tilde{\Sigma}_{11}$  and depends on the available numerical precision. Since the condition number  $\kappa$  of the matrix  $\underline{\mathbf{A}}$  is given by the ratio of largest to smallest singular value, a certain effective conditioning  $\kappa_{\text{eff}}$  can be enforced

by ignoring all singular values in the inversion lower than a certain value

$$\delta = \frac{\tilde{\Sigma}_{11}}{\kappa_{\text{eff}}} . \quad (4.30)$$

For the exemplary case of a double precision implementation, an ill-conditioning of the SLE can be avoided by choosing  $\kappa_{\text{eff}} < 1 \times 10^{16}$ .<sup>1</sup>

For the required QR-decomposition and SVD, the implementation relies on standard double precision LAPACK [73] routines for serial and the corresponding Scalable LAPACK (ScaLAPACK) [74] routines for parallel execution.

### 4.2.2 Solver Memory

Revisiting Eq. (4.9), one observes that the matrix  $\underline{\mathbf{A}}$  depends only on the expansion (centers and order) and the cavity (via the points  $\mathbf{p}_i$ ) and, e.g., not on the Hartree potential  $\Phi_{\text{H}}$ . Leaving aside the possibility that the cavity might depend on the charge density of the system, this means that  $\underline{\mathbf{A}}$  does not change during the SCF cycle. In this case, we can almost completely eliminate the computational overhead spent on solving the MPE equations in following SCF steps by simply memorizing the matrices used in Eq. (4.28) which amounts to storing two  $(n_A \times n_A)$  matrices,  $\underline{\mathbf{V}}^{\text{T}}$  and  $\underline{\mathbf{U}}$ ,  $n_A$  diagonal elements of  $\underline{\tilde{\Sigma}}$ , and the  $(m_A \times n_A)$  matrix  $\underline{\tilde{\mathbf{Q}}}$  together with the  $n_A$  elementary reflectors  $\tau$  created by the dgeqrf or pdgeqrf routine—in total  $(m_A + 2n_A + 2)n_A$  elements. In principle,  $\underline{\tilde{\mathbf{Q}}}$  and  $\underline{\tilde{\mathbf{U}}}$  could be combined to save the memory needed for  $\underline{\tilde{\mathbf{U}}}$ . This, however, was not done in the current implementation to avoid code branching in case of a fall-back to pure QR without SVD.

In the case of a pure QR-decomposition approach, the only matrix to be saved together with  $\underline{\tilde{\mathbf{Q}}}$  is  $\underline{\tilde{\mathbf{R}}}$  with  $\frac{1}{2}n_A(n_A + 1)$  non-zero elements. As the  $n_A$  elementary reflectors  $\tau$  are stored separately, all elements on the upper diagonal of  $\underline{\tilde{\mathbf{Q}}}$  are 1 and need not be stored explicitly. The same applies to the  $\frac{1}{2}n_A(n_A - 1)$  elements above the upper diagonal which are zero and redundant due to the column orthogonality of  $\underline{\tilde{\mathbf{Q}}}$ . This is exploited by the above mentioned QR-factorization routines which save  $\underline{\tilde{\mathbf{R}}}$  in the vacant upper triangular area of  $\underline{\tilde{\mathbf{Q}}}$ . The total solver memory then only needs to store  $(m_A + 1)n_A$  elements, i.e.,  $(2n_A + 1)n_A$  less than in the SVD case.

In the case of parallel execution *via* the Message Passing Interface, the solver memory is distributed over all processes which can aid to alleviate potential memory problems. Note, however, that besides the above mentioned memory additional storage space is needed during the solver's execution especially in the first run to temporarily store a non-negligible amount of intermediate results of the LAPACK and ScaLAPACK routines, as well as  $\underline{\mathbf{b}}$  and—at least at the first time of execution— $\underline{\mathbf{A}}$ .

### 4.2.3 Improving the Matrix Conditioning

As we have seen above, the solution to Eq. (4.10) amounts to an inversion of the left-hand side matrix  $\underline{\mathbf{A}}$ . The quality of the solution thus strongly depends on the conditioning of the problem. As already alluded to above, the SVD reveals the condition number  $\kappa$  of  $\underline{\mathbf{A}}$  which is the ratio of

<sup>1</sup>The implementation actually obtains the relative machine precision—which is the inverse of the coefficient number  $\kappa_{\text{eff}}$ —from a call to the LAPACK function `dlamch`.

the largest,  $\Sigma_{\max} = \tilde{\Sigma}_{11}$ , to the smallest,  $\Sigma_{\min} = \tilde{\Sigma}_{n_A n_A}$ , singular value,

$$\kappa = \frac{\Sigma_{\max}}{\Sigma_{\min}}. \quad (4.31)$$

The presented factorization methods do not worsen the conditioning, i.e. they do not increase  $\kappa$ , but can still run into problems when  $\kappa$  becomes very large. The remarkable robustness of the SVD in this case stems from the fact that it truncates the lower end of the singular value spectrum which it sets to zero. Obviously, this is accompanied by a loss of possibly relevant information. It is thus desirable to explore methods that allow to reformulate the equations such that the condition number of the matrix that needs to be inverted is reduced.

One case in which the matrix conditioning becomes a problem has already been presented in Fig. 4.2. When increasing the expansion orders, the regular, Eq. (3.38a), and irregular, Eq. (3.38b), solid harmonic basis functions show exactly opposite behavior for an input vector with length  $\|\mathbf{x}\|_2 > 1$ : While  $\mathcal{R}_m^l(\mathbf{x})$  becomes extremely large,  $\mathcal{I}_m^l(\mathbf{x})$  vanishes to zero (and *vice versa* for  $\|\mathbf{x}\|_2 < 1$ ). Combining these numbers of very different magnitude in the basis matrix  $\underline{\mathbf{A}}$ , cf. Eq. (4.10) naturally leads to a spread in the singular value spectrum of  $\underline{\mathbf{A}}$  as illustrated in Fig. 4.4. Limited by the available numerical accuracy, only a certain window of this spectrum can be taken into account which in the case of double precision calculations amounts to roughly 16 orders of magnitude. As can be seen in the top panels of Fig. 4.4, this may lead to a neglect of a large part of the spectrum. In fact, in several applications with an expansion order of  $l_{\max, R} = l_{\max, Q} = 14$  the introduced numerical errors prevented a convergence and led to oscillations in the SCF cycle. Of course this is an extreme case well beyond the convergence limit of the method for the relatively small systems investigated here. The situation, however, might change with increasing system size and such problems can already start to occur at lower expansion orders.

### **Uniform Coordinate Scaling**

Luckily, the above observations already hint to the solution of this problem. The difference between the different basis functions becomes smallest when the length of the input vector is close to 1. With  $\mathbf{x}$  being the difference between any point  $\mathbf{p}$  on the cavity surface and the expansion center's position  $\mathbf{r}_K$ , we propose a center-specific coordinate scaling by a scalar factor,  $\gamma > 0$ , for the solid harmonic functions such that  $\|\mathbf{x}\|_2$  does not exceed 1 for  $\mathcal{R}_m^l$ ,

$$\gamma_K \|\mathbf{p} - \mathbf{r}_K\|_2 \leq 1, \quad \forall \mathbf{p} \in \{ \mathbf{r} \mid \mathcal{C}(\mathbf{r}) = 0 \}, \quad (4.32a)$$

but is at least 1 for  $\mathcal{I}_m^l$ ,

$$\gamma_J \|\mathbf{p} - \mathbf{r}_J\|_2 \geq 1, \quad \forall \mathbf{p} \in \{ \mathbf{r} \mid \mathcal{C}(\mathbf{r}) = 0 \}. \quad (4.32b)$$

Therefore, the optimal  $\gamma_K$  can be determined from the largest distance of any surface point to center  $K$ ,

$$\gamma_K = \left[ \max_{\mathbf{p}} \left( \|\mathbf{p} - \mathbf{r}_K\|_2 \right) \right]^{-1}, \quad \mathcal{C}(\mathbf{p}) = 0, \quad (4.33a)$$

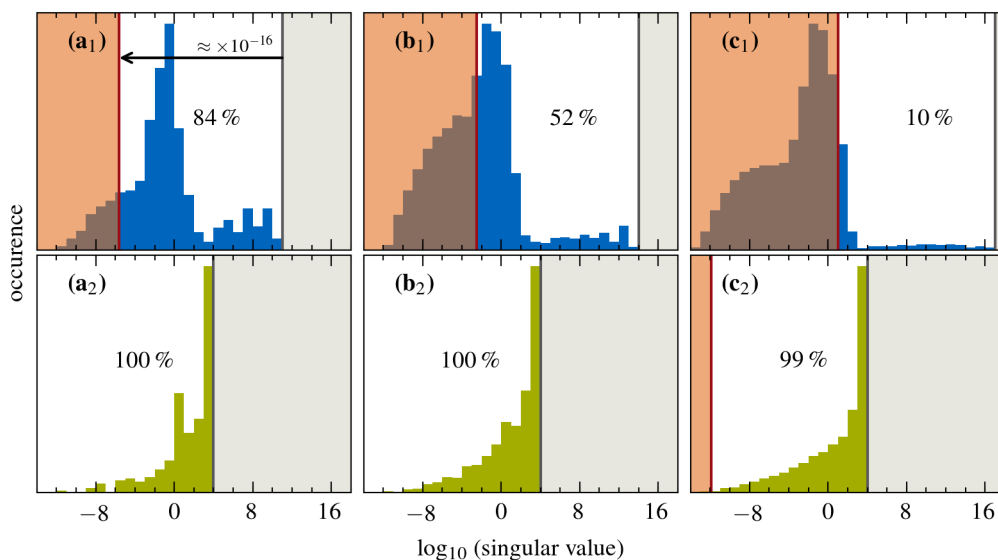


Fig. 4.4: Distribution of singular values of the basis matrix in the MPE equations for three small organic molecules out of the test-set T2 presented in section 6.1: **(a)** methane (chemical formula  $\text{CH}_4$ ), **(b)** benzene ( $\text{C}_6\text{H}_6$ ), and **(c)** n-octane ( $\text{C}_8\text{H}_{18}$ ). The potentials  $\Phi_R$  and  $\Phi_Q$  are expanded up to an order of  $l = 14$  and a number of cavity points is chosen such that the MPE equations are at least three-fold over-determined. In the top (subscript 1), the (logarithmized) singular values from a direct construction of Eq. (4.10) are shown whereas on the bottom (subscript 2) a coordinate scaling as presented in section 4.2.3 has been applied. The vertical gray line indicates the largest singular value in each spectrum and thus defines its right border. Any singular values smaller than roughly  $10^{-16}$  times the largest one are set to zero when creating the matrix's pseudo-inverse. This lower boundary of the considered spectrum is marked by a red vertical line and the neglected region in the spectrum is shaded in orange. The fraction of considered singular values is given in each tile.

and the optimal  $\gamma_J$  from the corresponding smallest distance,

$$\gamma_J = \left[ \min_{\mathbf{p}} \left( \|\mathbf{p} - \mathbf{r}_J\|_2 \right) \right]^{-1}, \quad \mathcal{C}(\mathbf{p}) = 0. \quad (4.33b)$$

Scaling the expansions in Eqs. (4.1a) and (4.1b) yield the following expressions which then enter in the left-hand side matrix  $\underline{\mathbf{A}}$  of Eq. (4.10),

$$\Phi_{\mathbf{R}}(\mathbf{r}) = \sum_{l=0}^{l_{\max, \mathbf{R}}} \sum_{m=-l}^l \tilde{R}_K^{(l,m)} \mathcal{R}_m^l(\gamma_K(\mathbf{r} - \mathbf{r}_K)), \quad (4.34a)$$

and

$$\Phi_{\mathbf{Q}}(\mathbf{r}) = \sum_{J=1}^N \sum_{l=0}^{l_{\max, \mathbf{Q}}} \sum_{m=-l}^l \tilde{Q}_J^{(l,m)} \mathcal{I}_m^l(\gamma_J(\mathbf{r} - \mathbf{r}_J)). \quad (4.34b)$$

The improvement on the conditioning of the problem is clearly visible when comparing the top and bottom singular value spectra in Fig. 4.4 where the only difference is the introduced uniform coordinate scaling. Not only can a much larger part of the spectrum be covered but the singular values are also accumulated at its right boundary which—depending on the right-hand side in the SLE—can increase the numerical accuracy of the solution obtained by the pseudo-inverse [72].

### ***Obtaining the Unscaled Coefficients***

The modifications of Eqs. (4.34a) and (4.34b) with respect to Eqs. (4.1a) and (4.1b), of course, also affect the expansion coefficients—which are now denoted as  $\tilde{R}$  and  $\tilde{Q}$ , respectively. Due to the polynomial form of the solid harmonic functions, cf. Eqs. (3.38a) and (3.38b), the uniform scaling factor can simply be factorized out of the regular,

$$\mathcal{R}_m^l(\gamma_K(\mathbf{r} - \mathbf{r}_K)) = (\gamma_K)^l \mathcal{R}_m^l(\mathbf{r} - \mathbf{r}_K), \quad (4.35a)$$

and irregular,

$$\mathcal{I}_m^l(\gamma_J(\mathbf{r} - \mathbf{r}_J)) = (\gamma_J)^{-l-1} \mathcal{I}_m^l(\mathbf{r} - \mathbf{r}_J), \quad (4.35b)$$

solid harmonic functions. Inserting a unity expression in the potential expansions of  $\Phi_{\mathbf{R}}$ , Eq. (4.1a),

$$\Phi_{\mathbf{R}}(\mathbf{r}) = \sum_{l=0}^{l_{\max, \mathbf{R}}} \sum_{m=-l}^l R_K^{(l,m)} (\gamma_K)^{-l} (\gamma_K)^l \mathcal{R}_m^l(\mathbf{r} - \mathbf{r}_K), \quad (4.36)$$

and comparing this to Eq. (4.35a) immediately identifies the new expansion coefficients as simply being the old ones scaled by an inverse factor, i.e.

$$\tilde{R}_K^{(l,m)} = (\gamma_K)^{-l} R_K^{(l,m)}. \quad (4.37)$$

Therefore, having solved the MPE equations with the better conditioned basis matrix, it is straightforward to obtain the (unscaled) expansion coefficients,  $R$ , from the (scaled) solution,  $\tilde{R}$ ,

$$R_K^{(l,m)} = (\gamma_K)^l \tilde{R}_K^{(l,m)}. \quad (4.38a)$$

Similarly, one finds

$$Q_J^{(l,m)} = (\gamma_J)^{-l-1} \tilde{Q}_J^{(l,m)}. \quad (4.38b)$$

### 4.3 Benchmark Systems

In the following, our implementation of the MPE model is tested on two different benchmark systems. First, we compare calculated solvation energies of ions in spherical cavities to the analytically solvable Born model. Second, to gauge the accuracy of the reaction field, the electrostatic potential in a number of 2D systems is compared against the one obtained with a high-accuracy finite-element solver for the generalized Poisson equation. The interplay of MPE electrostatics and non-electrostatic effects (computed from volume and surface of the solvation cavity) first requires the introduction of a cavity generation method and is thus explored later on during the parametrization of the full model (cf. chapter 6).

#### 4.3.1 Born Equation

The first benchmark model discussed here is the (electrostatic) free energy of solvation,  $\Delta G_{\text{el}}^{\text{Born}}$ , of a spherical, atomic ion with radius  $a$  carrying a charge  $q$ , as calculated by Born [43] in (1920) using Eq. (3.24). As already observed by Kirkwood [19] in the 1930s, the MPE model trivially agrees with the Born equation in case of spherically symmetric problems. Then, the multipole expansions of the involved electrostatic potentials reduce to monopoles centered at the origin. Evaluating the boundary conditions at any one point on the interface then leads to an SLE with a square ( $2 \times 2$ ) matrix  $\underline{A}$  which can easily be solved by hand to yield Eq. (3.24). Due to the existence of this analytical solution, spherical problems are an ideal first test-case for any numerical implementation. In Figure 4.5 we compare our results for the Born model with the analytical reference for 10 different dielectric permittivities  $\epsilon_b$  and 3 charges  $q$ , and can thereby rule out implementation errors and significant numerical inaccuracies.

#### 4.3.2 2D Model Systems: Comparison to FEM

In the second benchmark, more complex charge distributions are addressed while the simple radially symmetric geometry of the cavity is retained. As there is no general, analytical solution to such a problem, we compare here to a direct solution of the generalized Poisson equation, Eq. (3.15), calculated by KARDOS [75], an adaptive finite element method (FEM) solver for nonlinear parabolic systems of partial differential equations. It should be noted that in principle, a solution to Eq. (3.15) or similar equations can be obtained efficiently with FEM solvers, also for realistic systems [76]. Most of such established approaches, however, rely on regularly spaced integration grids whereas FHI-aims—similar to other electronic structure codes based on localized basis sets—uses atom-centered, non-uniform spherical grids. For reasons of efficiency and accuracy

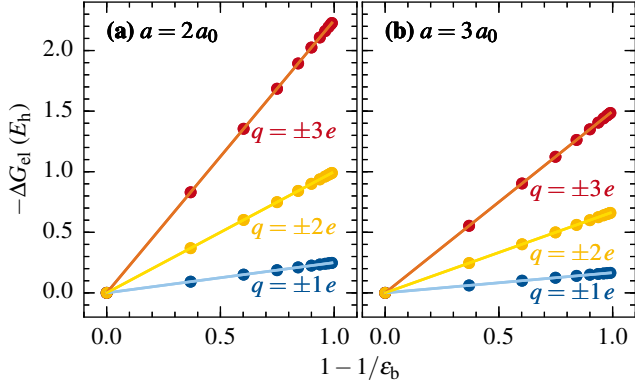


Fig. 4.5: Comparison of the free energy of solvation  $\Delta G_{el}$  for ions calculated with charges  $q = \pm 1 e$  (blue),  $q = \pm 2 e$  (yellow), and  $q = \pm 3 e$  (red) in spherical cavities with two different radii: (a)  $a = 2 a_0$  and (b)  $a = 3 a_0$ . Shown are results from the MPE model (dots) and analytical results from the Born equation (lines), see text. Reprinted with permission from Ref. [1]. © 2017 American Chemical Society.

we therefore avoid interpolating between the two grids, favoring the MPE method for the all electron solvation problem.

More technical details of the finite-element approach are presented in appendix B.

### Benchmark Setup

In order to efficiently achieve highly accurate FEM solutions, the (inherently 3D) model systems in this section are constructed such that they exhibit rotational symmetry around the Cartesian  $z$ -axis allowing for a projection into a 2D cylindrical coordinate system. It is spanned by the polar axis  $\rho$  and the longitudinal axis  $\zeta$ , where the latter coincides with the Cartesian  $z$ -axis. This allows to employ significantly refined FEM grids with a minimum mesh size of  $3 \times 10^{-3} a_0$ . Due to the rotation symmetry, the multipole expansion basis of such a system's electrostatic potential can be reduced to irregular solid harmonics with  $m = 0$ , as defined in 3.38b, positioned on the  $\zeta$ -axis. For a system of  $n$  multipoles of order  $l_i$  with magnitude  $M_i^{(l_i,0)}$  positioned on the  $\zeta$  (or  $z$ ) axis at a value of  $\zeta = \zeta_i$ , the vacuum potential reads

$$\Phi_0(\rho, \zeta) = \sum_{i=1}^n M_i^{(l_i,0)} \mathcal{I}_{(l_i,0)}(\rho, \zeta - \zeta_i). \quad (4.39)$$

Analyzing all combinations of

$$\begin{aligned} n &\in \{1, 2, 3\}, \\ l_i &\in \{0, 1, 2\}, \\ M_i^{(l_i,0)} &\in \{-1, 1\}, \end{aligned}$$

and

$$\zeta_i \in \{-0.6, -0.3, 0.0, 0.3, 0.6\},$$



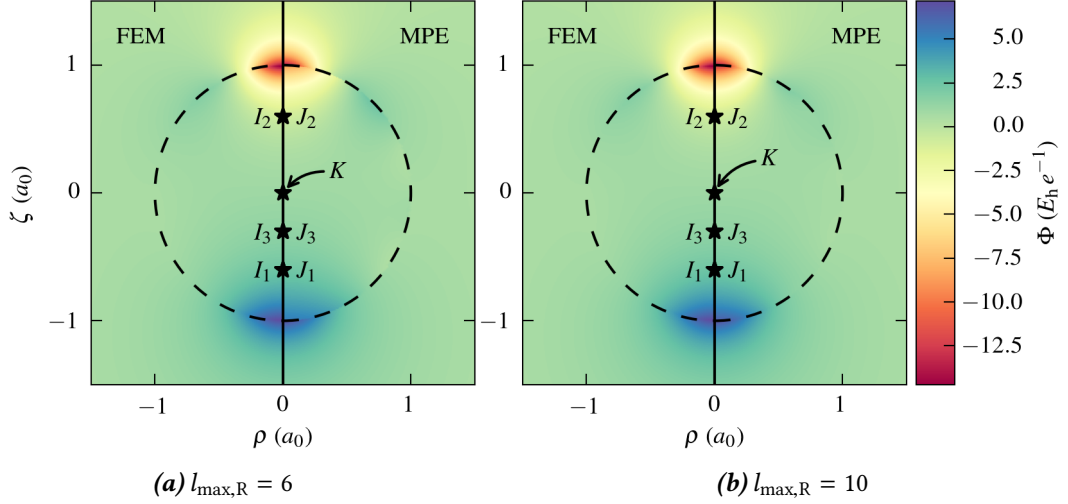


Fig. 4.6: Exemplary benchmark setup. The point multipoles are placed at centers  $I_i$  on the  $\zeta$  axis within a cavity of radius  $r_c$  (dashed circle). The MPE expansion centers are placed at sites  $K$  and  $J_i$  with respective expansion orders of  $l_{\max,Q} = 6$  and  $l_{\max,R}$  as indicated below the two panels. The resulting potentials for FEM and MPE are shown in color-code on the left and right hand side, respectively, of each panel.

one finds that 27900 of them lead to a non-vanishing  $\Phi_0$ . Those define the set of model potentials used for comparison between the MPE and FEM methods—as exemplified in Figure 4.6.

The radius  $r_c$  of the (spherical) solvent cavity is fixed at a value of  $1 a_0$  throughout this section. For each model potential, we sample a set of logarithmically spaced relative dielectric permittivities with values of

$$\varepsilon_b \in \{10^{0.48}, 10^{0.96}, 10^{1.44}, 10^{1.92}, 10^{2.40}\} \approx \{3.02, 9.12, 27.5, 83.2, 251\}$$

which leads to a total of 139500 combinations.

For all of those model systems (i.e. model potential and dielectric permittivity), two calculations are performed: First, a discrete grid representation of the reaction field  $\Phi'$ , cf. Eq. (B.24), is calculated with the FEM solver KARDOS. Second, the MPE method is used to calculate  $\Phi_\delta$  with the expansion center  $K$  of the reaction field  $\Phi_R$  being placed at the origin of the coordinate system, cf. Eq. (4.1a), whereas the multiple centers of  $\Phi_Q$ , cf. Eq. (4.1b), are identical to the positions of the multipole charges in  $\Phi_0$ . Using a simple modification, cf. Eq. (B.25), this potential can be directly compared to  $\Phi'$ .

In all MPE calculations,  $\Phi_Q$  is expanded up to an order of  $l_{\max,Q} = 6$ . The expansion order of the reaction field  $\Phi_R$ ,  $l_{\max,R}$ , will be subject to a convergence study. The subsequent discrete evaluation of  $\Phi_\delta$  (and also  $\Phi'_\delta$ ) is performed on the same grid used for the representation of  $\Phi'$  to avoid interpolation errors.

### Integration

In order to assess the agreement between FEM and MPE results, it is convenient to derive scalar quantities that can easily be compared. To this end, a good observable is the interaction energy  $E$

of a charge distribution  $\kappa$  with the electrostatic potential  $\Phi$ .

$$E = \int \kappa(\mathbf{r})\Phi(\mathbf{r})d\mathbf{r} \quad (4.40)$$

As the benchmark systems consists only of classical point multipoles, Eq. (4.40) would only probe the potential at the position of the expansion centers. Therefore, we introduce the fictitious density  $\kappa$  in two different “flavors”:  $\kappa_{\text{hom}}$  is equivalent to a homogeneous charge distribution of a single elementary charge in the cavity and  $\kappa_{\text{Gauss}}$  to a Gaussian shaped distribution of one elementary charge with a width of  $\tau^2 = 0.1 a_0^2$ , i.e. 2% of the density is located outside of the cavity.

$$\kappa_{\text{hom}}(\mathbf{r}) = \begin{cases} \frac{1 e}{V_{\text{cav}}}, & \|\mathbf{r}\|_2 \leq r_c \\ 0, & \text{otherwise} \end{cases} \quad (4.41a)$$

$$\kappa_{\text{Gauss}}(\mathbf{r}) = \frac{1 e}{\left(\sqrt{2\pi\tau^2}\right)^3} \exp\left(-\frac{\mathbf{r}^2}{2\tau^2}\right) \quad (4.41b)$$

While the homogeneous fictitious charge distribution is a good probe for the overall agreement between MPE and FEM,  $\kappa_{\text{Gauss}}$  amounts to a weighting of the integration towards the physically relevant regions close to the interaction centers.

The integration of Eq. (4.40) is performed numerically on the adaptive triangular grid created by the finite element solver using integration weights  $dV_i$  at grid points  $\mathbf{r}_i$  as described in appendix B.4,

$$E = \sum_i \kappa(\mathbf{r}_i) \cdot \Phi(\mathbf{r}_i) \cdot dV_i . \quad (4.42)$$

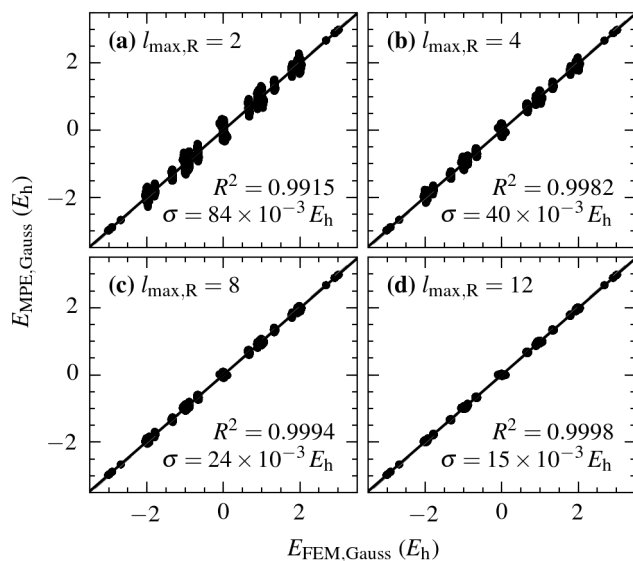
### Benchmark Results

For the 139500 setups in the 2D test-set of different model potential and dielectric permittivity, the fictitious energy expression in Eq. (4.42) is evaluated separately for  $\Phi'$  and  $\Phi'_\delta$ , once for the Gaussian and once for the homogeneous charge density, i.e.  $\kappa \in \{\kappa_{\text{hom}}, \kappa_{\text{Gauss}}\}$ . Figure 4.7a depicts the correlation of  $E_{\text{FEM,Gauss}}$  and  $E_{\text{MPE,Gauss}}$ . While the coefficient of determination  $R^2$  already hints at an excellent correlation for the lowest expansion order of  $l_{\text{max,R}} = 2$  for  $\Phi_p$ , the root-mean-square error  $\sigma$

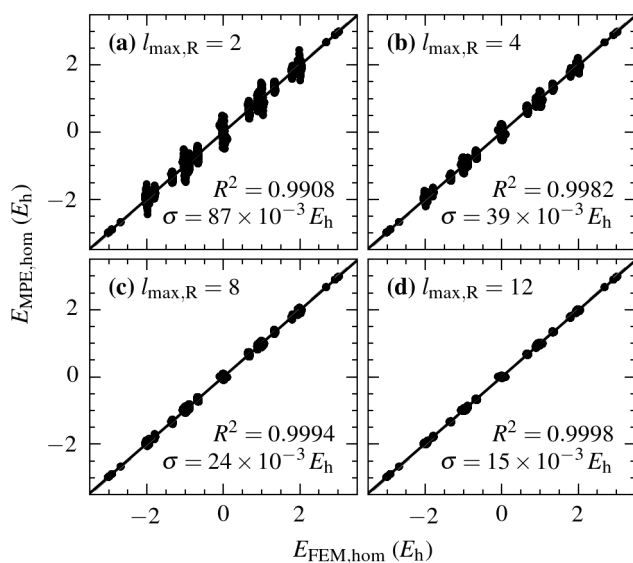
$$\sigma = \sqrt{\frac{1}{N} \sum_{i=1}^N \left(E_{\text{FEM,Gauss}} - E_{\text{MPE,Gauss}}\right)^2} \quad (4.43)$$

improves visibly when the expansion order is increased. At an expansion order of  $l_{\text{max,R}} = 4$ , the seemingly large value of  $\sigma = 40 \times 10^{-3} E_h$  is already less than 1% of the spanned energy range. The corresponding correlation for the homogeneous charge density depicted in Fig. 4.7b exhibits almost identical correlation coefficients and standard deviations compared to the ones calculated for the Gaussian density except for low expansion orders where the spread of results is slightly larger for the homogeneous charge density.

Considering the simple, highly symmetric dielectric function in this synthetic benchmark,



(a) Gaussian charge density. Reprinted with permission from Ref. [1]. © 2017 American Chemical Society.



(b) Homogeneous charge density

Fig. 4.7: Correlation graph for FEM and MPE interaction energies  $E$  of the polarization potential, as defined in Eq. (4.40) for different expansion orders  $l_{\max,R}$  for the MPE reaction field  $\Phi_\delta$ .

these results suggest a minimal expansion order of 4 for the application on realistic (molecular) geometries. Yet, we point out that the expansion order of the potentials is a convergence parameter which in principle needs to be checked for each system.

## 4.4 A Note on Previous MPE Models

The above approach is not entirely unique in the sense that also previous MPE models and implementations [20, 59] used solid harmonic basis functions for the potential expansion, discretized the problem on the cavity surface, and reformulated and solved the problem using very similar linear algebra methods. There are, however, important conceptual differences which are mainly related to the outlying charge problem discussed earlier (cf. sections 3.3.2 and 3.3.3).

### 4.4.1 Hartree Potential Expansion

In the derivations so far, no assumption has been made about the shape of the Hartree potential,  $\Phi_H$ . In fact, it is only assumed that  $\Phi_H$  exists and can be evaluated (to sufficient accuracy) at all points on the cavity surface. As an example, FHI-aims offers a very efficient way of evaluation at arbitrary points in real space by representing  $\Phi_H$  in a splined multipole expanded form which can be written as

$$\Phi_H^{\text{aims}}(\mathbf{r}) = \sum_{I=1}^N \sum_{l=0}^{l_{\text{max,H}}} \sum_{m=-l}^l v_I^{(l,m)}(\|\mathbf{r} - \mathbf{r}_I\|_2) Y_m^l(\mathbf{r} - \mathbf{r}_I) \quad (4.44)$$

where  $\mathbf{r}_I$  are the coordinates of the expansion center situated at nucleus  $I$ . Unlike in the original formulation of FHI-aims [22], we do not distinguish here between different contributions, e.g. from the nuclei or electrons. In Eq. (4.44), the free atom contributions are for example simply included in the monopole terms  $v_I^{(0,0)}$ . Previous MPE models, on the other hand, suggested the following representation [20, 59],

$$\Phi_H^{\text{ff}}(\mathbf{r}) = \sum_{I=1}^N \sum_{l=0}^{l_{\text{max,H}}} \sum_{m=-l}^l M_I^{(l,m)} \|\mathbf{r} - \mathbf{r}_I\|_2^{-l-1} Y_m^l(\mathbf{r} - \mathbf{r}_I) = \sum_{I=1}^N \sum_{l=0}^{l_{\text{max,H}}} \sum_{m=-l}^l M_I^{(l,m)} \mathcal{I}_m^l(\mathbf{r} - \mathbf{r}_I), \quad (4.45)$$

with the so-called multipole moments  $M_I^{(l,m)}$ .

Equation (4.44) is very similar to Eq. (4.45) with one decisive difference, namely, the expansion coefficients  $v_I^{(l,m)}$  are radial splines and as such a generalization of the simple  $\|\mathbf{r} - \mathbf{r}_I\|_2^{-l-1}$  radial term. Only this allows Eq. (4.44) to describe the electrostatic potential within an extended charge distribution while Eq. (4.1b) only provides an exact description outside of this charge distribution, i.e. in the absence of a source. This means that the value of  $\Phi_H^{\text{ff}}$  is equal to  $\Phi_H^{\text{aims}}$  only when the charge density is completely localized within the cavity. This assumption has already been discussed earlier in the context of the ASC method (cf. section 3.3.2). Since both expressions then no longer describe the true Hartree potential of the unlocalized charge density, the potential values entering the MPE equations are also not exact. We only dare to speculate whether error cancellation or suitable parametrization is responsible for the apparently lower impact of this approximation regarding that this issue is rarely discussed in literature about MPE models [77].

#### 4.4.2 Probe Charge Approach

The advantage of the simplified form of Eq. (4.45) becomes apparent when each reaction field coefficient,  $R$ , is expressed in terms of linear response coupling factors  $f$  to the multipole moments  $M$ ,

$$R_K^{(l,m)} = \sum_{I=1}^N \sum_{l'=0}^{l_{\max}} \sum_{m'=-l'}^{l'} f_{K,I}^{(l,m),(l',m')} M_I^{(l',m')}. \quad (4.46)$$

The term  $f_{K,I}^{(l,m),(l',m')}$  describes the influence of a single multipole component  $(l', m')$  of the Hartree potential at center  $I$  on the reaction field's multipole component  $(l, m)$  at center  $K$ . Note that the implicitly assumed linearity of the solvent is no additional approximation but has already been introduced to the model in the early stages of its derivation, cf. section 3.1.2.

The effective decoupling of contributions from different multipole moments in eq 4.46 is due to the superposition principle. One can thus probe the effect of each single multipole moment  $M_I^{(l',m')}$  separately with a hypothetical Hartree potential that consists only of the respective probed multipole component  $M_{\tilde{I}}^{(\tilde{l},\tilde{m})}$ , the so called probe charge, i.e.

$$M_I^{(l',m')} = M_{\tilde{I}}^{(\tilde{l},\tilde{m})} \delta_{(I,\tilde{I})} \delta_{(l',\tilde{l})} \delta_{(m',\tilde{m})}, \quad (4.47)$$

where  $\delta$  is the Kronecker delta. It should be noted here that any non-zero value is a valid choice for  $M_{\tilde{I}}^{(\tilde{l},\tilde{m})}$ . Inserting the terms corresponding to this chosen probe charge—i.e.

$$\Phi_{\text{H}}^{\text{ff,probe}}(\mathbf{r}) = M_{\tilde{I}}^{(\tilde{l},\tilde{m})} \mathcal{I}_{\tilde{m}}^{\tilde{l}}(\mathbf{r} - \mathbf{r}_{\tilde{I}}) \quad (4.48)$$

for  $\Phi_{\text{H}}$  and

$$\Phi_{\text{R}}^{\text{probe}}(\mathbf{r}) = \sum_{l=0}^{l_{\max,\text{R}}} \sum_{m=-l}^l f_{K,I}^{(l,m),(\tilde{l},\tilde{m})} M_{\tilde{I}}^{(\tilde{l},\tilde{m})} \mathcal{R}_m^l(\mathbf{r} - \mathbf{r}_K) \quad (4.49)$$

for  $\Phi_{\text{R}}$ —into Eq. (4.7) and reformulating the result again yields a matrix equation with the same basis set matrix  $\underline{\mathbf{A}}$  but a different right-hand side and unknowns,

$$\underline{\mathbf{A}} \cdot \begin{pmatrix} f_{K,\tilde{I}}^{(0,0),(\tilde{l},\tilde{m})} M_{\tilde{I}}^{(\tilde{l},\tilde{m})} \\ f_{K,\tilde{I}}^{(1,-1),(\tilde{l},\tilde{m})} M_{\tilde{I}}^{(\tilde{l},\tilde{m})} \\ \vdots \\ Q_{J_1}^{(0,0)} \\ Q_{J_1}^{(1,-1)} \\ \vdots \\ Q_{J_2}^{(0,0)} \\ Q_{J_2}^{(1,-1)} \\ \vdots \end{pmatrix} = (\epsilon_{\text{b}}^{-1} - 1) \begin{pmatrix} \mathcal{I}_{\tilde{m}}^{\tilde{l}}(\mathbf{p}_1, \mathbf{r}_{\tilde{I}}) M_{\tilde{I}}^{(\tilde{l},\tilde{m})} \\ 0 \\ \mathcal{I}_{\tilde{m}}^{\tilde{l}}(\mathbf{p}_2, \mathbf{r}_{\tilde{I}}) M_{\tilde{I}}^{(\tilde{l},\tilde{m})} \\ 0 \\ \vdots \end{pmatrix}. \quad (4.50)$$

Now, Eq. (4.50) has to be solved for every possible probe charge, i.e. every combination of  $\tilde{l}$ ,  $\tilde{l}$ , and  $\tilde{m}$ . This can be done simultaneously in a single matrix equation,

$$\mathbf{A} \cdot \begin{pmatrix} f_{K, \tilde{l}_1}^{(0,0),(0,0)} M_{\tilde{l}_1}^{(0,0)} & f_{K, \tilde{l}_1}^{(0,0),(1,-1)} M_{\tilde{l}_1}^{(1,-1)} & \dots & f_{K, \tilde{l}_2}^{(0,0),(0,0)} M_{\tilde{l}_2}^{(0,0)} & \dots \\ f_{K, \tilde{l}_1}^{(1,-1),(0,0)} M_{\tilde{l}_1}^{(0,0)} & f_{K, \tilde{l}_1}^{(1,-1),(1,-1)} M_{\tilde{l}_1}^{(1,-1)} & \dots & f_{K, \tilde{l}_2}^{(1,-1),(0,0)} M_{\tilde{l}_2}^{(0,0)} & \dots \\ f_{K, \tilde{l}_1}^{(1,0),(0,0)} M_{\tilde{l}_1}^{(0,0)} & f_{K, \tilde{l}_1}^{(1,0),(1,-1)} M_{\tilde{l}_1}^{(1,-1)} & \dots & f_{K, \tilde{l}_2}^{(1,0),(0,0)} M_{\tilde{l}_2}^{(0,0)} & \dots \\ \vdots & \vdots & & \vdots & \\ Q_{J_1}^{(0,0)} & Q_{J_1}^{(0,0)} & \dots & Q_{J_1}^{(0,0)} & \dots \\ Q_{J_1}^{(1,-1)} & Q_{J_1}^{(1,-1)} & \dots & Q_{J_1}^{(1,-1)} & \dots \\ \vdots & \vdots & & \vdots & \\ Q_{J_2}^{(0,0)} & Q_{J_2}^{(0,0)} & \dots & Q_{J_2}^{(0,0)} & \dots \\ Q_{J_2}^{(1,-1)} & Q_{J_2}^{(1,-1)} & \dots & Q_{J_2}^{(1,-1)} & \dots \\ \vdots & \vdots & & \vdots & \ddots \end{pmatrix} = \quad (4.51)$$

$$(\varepsilon_b^{-1} - 1) \begin{pmatrix} \mathcal{I}_0^0(\mathbf{p}_1, \mathbf{r}_{\tilde{l}_1}) M_{\tilde{l}_1}^{(0,0)} & \mathcal{I}_{-1}^1(\mathbf{p}_1, \mathbf{r}_{\tilde{l}_1}) M_{\tilde{l}_1}^{(1,-1)} & \dots & \mathcal{I}_0^0(\mathbf{p}_1, \mathbf{r}_{\tilde{l}_2}) M_{\tilde{l}_2}^{(0,0)} & \dots \\ 0 & 0 & \dots & 0 & \dots \\ \mathcal{I}_0^0(\mathbf{p}_2, \mathbf{r}_{\tilde{l}_1}) M_{\tilde{l}_1}^{(0,0)} & \mathcal{I}_{-1}^1(\mathbf{p}_2, \mathbf{r}_{\tilde{l}_1}) M_{\tilde{l}_1}^{(1,-1)} & \dots & \mathcal{I}_0^0(\mathbf{p}_2, \mathbf{r}_{\tilde{l}_2}) M_{\tilde{l}_2}^{(0,0)} & \dots \\ 0 & 0 & \dots & 0 & \dots \\ \vdots & \vdots & & \vdots & \ddots \end{pmatrix}.$$

Similar to Eq. (4.10), Eq. (4.51) can be abbreviated as

$$\mathbf{AC} = \mathbf{B}, \quad (4.52)$$

with an  $(n_A \times k_A)$  matrix of unknowns  $\mathbf{C}$  and an  $(m_A \times k_A)$  right-hand side matrix  $\mathbf{B}$ . Since  $\mathbf{A}$  and its factorization are the same as before in the “direct” approach, the exact same methods to obtain the least square solution  $\tilde{\mathbf{C}}$  are applicable, i.e. for the pure QR-decomposition in analogy to Eq. (4.21),

$$\tilde{\mathbf{R}}\tilde{\mathbf{C}} = \tilde{\mathbf{Q}}^T \mathbf{B}, \quad (4.53)$$

and for the pseudo-inverse *via* SVD in analogy to Eq. (4.28),

$$\tilde{\mathbf{C}} = \mathbf{V}\tilde{\Sigma}^\dagger \left( \tilde{\mathbf{Q}}\tilde{\mathbf{U}} \right)^T \mathbf{B}. \quad (4.54)$$

From  $\tilde{\mathbf{C}}$ , the reaction field factors  $f$  are then extracted *via* a simple rescaling with the probe charges’ multipole moments. Once these reaction field factors are known, Eq. (4.49) can be used to construct  $\Phi_R$  given the multipole moments  $M$  of an expanded Hartree potential  $\Phi_H^{\text{ff}}$  (cf. Eq. (4.45)).

The electrostatic solvation free energy  $\Delta G_{\text{el}}^{\text{MPE,probe}}$ , cf. Eq. (3.19), is given by the interaction of  $\Phi_R$  with the (model) charge density that is the source of  $\Phi_H^{\text{ff}}$  which can be written in the relatively

simple form [16]

$$\begin{aligned}\Delta G_{\text{el}}^{\text{MPE,probe}} &= \frac{1}{2} \sum_{J=1}^N \sum_{l=0}^{l_{\text{max}}} \sum_{m=-l}^l M_J^{(l,m)} R_J^{(l,m)} \\ &= \frac{1}{2} \sum_{J=1}^N \sum_{l=0}^{l_{\text{max}}} \sum_{m=-l}^l M_J^{(l,m)} \sum_{I=1}^N \sum_{l'=0}^{l_{\text{max}}} \sum_{m'=-l'}^{l'} f_{J,I}^{(l,m),(l',m')} M_I^{(l',m')}.\end{aligned}\quad (4.55)$$

In essence, the above equation sums over center ( $J$ ) and multipole ( $l, m$ ) partitioned interactions of the model density with the reaction field. Equation (4.52), however, only serves to calculate the reaction field factors—and thus also  $R$ —at a single center  $K$ . Since the previous literature [20] is not very specific about this issue, we would like to point out that Eq. (4.52) does not have to be solved for each center  $K = J$  which could become very costly as the matrix  $\underline{\mathbf{A}}$  depends on the choice of  $K$ . Instead, given the solution of Eq. (4.52) for a single center  $K$ , one can analytically and exactly translate  $\Phi_{\text{R}}$  from this to any other center  $J$  where it can be expressed using a different set of expansion coefficients [70],

$$\Phi_{\text{R}}(\mathbf{r}) = \sum_{l''=0}^{l_{\text{max}}} \sum_{m''=-l''}^{l''} R_K^{(l'',m'')} \mathcal{R}_{m''}^{l''}(\mathbf{r} - \mathbf{r}_K) = \sum_{l=0}^{l_{\text{max}}} \sum_{m=-l}^l R_J^{(l,m)} \mathcal{R}_m^l(\mathbf{r} - \mathbf{r}_J). \quad (4.56)$$

As any multipole  $R_K^{(l'',m'')}$  on center  $K$  can correspond to a mixture of multipoles  $R_J^{(l,m)}$  with the same or lower expansion order (i.e.,  $l'' \geq l$ ), the effect of the translation is expressed in terms of a translational coupling  $t$ ,

$$R_J^{(l,m)} = \sum_{l''=0}^{l_{\text{max}}} \sum_{m''=-l''}^{l''} t_{J,K}^{(l,m),(l'',m'')} R_K^{(l'',m'')}. \quad (4.57)$$

Inserting Eq. (4.57) into Eq. (4.55), one obtains the following result

$$\begin{aligned}\Delta G_{\text{el}}^{\text{MPE,probe}} &= \frac{1}{2} \sum_{J=1}^N \sum_{l=0}^{l_{\text{max}}} \sum_{m=-l}^l M_J^{(l,m)} \sum_{l''=0}^{l_{\text{max}}} \sum_{m''=-l''}^{l''} t_{J,K}^{(l,m),(l'',m'')} R_K^{(l'',m'')} \\ &= \frac{1}{2} \sum_{J=1}^N \sum_{l=0}^{l_{\text{max}}} \sum_{m=-l}^l M_J^{(l,m)} \sum_{l''=0}^{l_{\text{max}}} \sum_{m''=-l''}^{l''} t_{J,K}^{(l,m),(l'',m'')} \sum_{I=1}^N \sum_{l'=0}^{l_{\text{max}}} \sum_{m'=-l'}^{l'} f_{K,I}^{(l'',m''),(l',m')} M_I^{(l',m')},\end{aligned}\quad (4.58)$$

where the coupling terms  $f$  can be extracted from the solution to Eq. (4.52) and  $t$  can be calculated analytically. Note that  $t$  depends only on the choice of expansion centers and the maximum order  $l_{\text{max}}$ , and  $f$  additionally on the geometry of the cavity. This means that when the cavity surface does not change, the new reaction field can be directly obtained from Eq. (4.49) and the electrostatic free energy of solvation from Eq. (4.58) when the multipole expansion of the Hartree potential changes.

As a final side note we remark that, since the model density is restricted to the inside of the cavity, the coefficients  $Q$  are not of real interest in the “probe charge” approach and merely serve to enforce the correct boundary conditions in Eq. (4.52).

### 4.4.3 Comparison to the Direct Approach

The overall computational complexity of solving the matrix Eqs. (4.10) and (4.52) is dominated by the factorization of  $\underline{\mathbf{A}}$ , rendering the additional effort spent for matrix-matrix *versus* matrix-vector multiplications almost negligible. With both methods targeting a self-consistent description of the solvation effect, the real difference between the “direct” and the “probe charge” approach lies in the way what information is stored between SCF steps and how it can be used.

In terms of simplicity, we believe the “direct” approach clearly beats the “probe charge” approach. Furthermore, a lot of overhead to compute the reaction field factors can be saved should the cavity’s geometry change during the SCF cycle.

The “probe charge” approach is only significantly faster when not enough memory is available to store the factorization of  $\underline{\mathbf{A}}$ . Otherwise, the reaction field coefficients are readily available in the “direct” approach with a few matrix-vector multiplications.

The most important advantage of the “direct” approach, however, stems from the fact that it does not require any specific form of the Hartree potential. Having overcome the necessity to express the Hartree potential in terms of a multipole expansion, Eq. (4.45), the “direct” approach finally allows to get rid of the outlying charge problem. Therefore, the choice of which model to implement has been made clearly in favor of the “direct” approach.





## 5 *Isodensity Cavity Generation* ‡

---

As previously outlined in section 3.5, different types of implicit solvation cavities are being used in practical applications. The common approach is to define a deterministic cavity generation function which will include some to many model parameters. The latter are then typically adjusted such that a given observable fits best to reference calculations or experimental measurements of a sufficiently large set of test systems (see e.g. Ref. [21]). In the case of the MPE model, these cavity functions should readily yield a chosen number of points, preferably equidistributed over a smooth, closed surface. Furthermore, the generation function needs to yield a—sufficiently efficient—way to determine normal vectors on this surface for each of the given points. Due to several extensions [20, 57] to the early examples of MPE methods [19, 56], this surface is not limited to any particular shape as long as it is smooth enough.

Our current implementation relies on cavities that are iso-surfaces of the DFT electronic density. These are, by definition, smooth and—from the level of GGA functionals upwards—the normal vectors are trivially available in the form of the density gradient. On top of that, this density-based cavity generation has the added advantage of only depending on a single free parameter, i.e., the density iso-value  $\rho_{\text{iso}}$ . It is important to note here that the overall achievable accuracy of an implicit solvation model, i.e. how faithfully it reproduces explicit or experimental solvation results, is to a very large degree determined through the choice of the solvation cavity. To this end, earlier studies [21, 42, 50, 62, 68, 78, 79] already demonstrated the applicability of charge density based cavities, reproducing solvation free energies for a large molecular test-set—even in the case of charged molecular ions [80]. In the following, an efficient way of determining a set of evenly spaced points and their surface normals for use in MPE solvation calculations will be presented.

### 5.1 *Density-Walker Initialization*

Given the cavity function  $\mathcal{C}$  from section 3.2, the task now is to find enough points  $\mathbf{p}$  on the cavity surface to set up the MPE equation systems, Eq. (4.10) (or, respectively, Eq. (4.52) for the probe charge approach). The task of finding points on an iso-surface of  $\mathcal{C}$ , without loss of generality in this case  $\mathcal{C}(\mathbf{p}) = 0$ , however, is complicated by the fact that the density is not known analytically. A direct root finding of e.g. a 3D spline function is complex and would also not guarantee an even spacing of points in the interface. Yet, as mentioned above, in order to minimize the number of linearly dependent rows in the coefficient matrix, spreading the interface points as evenly as possible over the entire cavity surface is clearly desirable. To facilitate cavity point generation and ensure homogeneous sampling of the interface, we therefore present a deterministic algorithm based on a constrained molecular dynamics of a set of fictitious “density-walkers”.

---

‡Reprinted in parts with permission from Ref. [1]. © 2017 American Chemical Society.

### 5.1.1 Atomic Spherical Grids

The total number of points to generate on the interface,  $M$ , is given by the required degree of determination,  $d_{\text{det}}$ , of the SLEs—as previously motivated in section 4.1.2. In the present algorithm, each of these interface points is represented as a pseudo-particle in space which we term a density-walker. The set of density-walkers is initialized from a superposition of spherical Lebedev-Laikov (LL) grids [81] around all  $N$  atomic centers—each sphere with a radius  $R_J$  and  $M_J$  grid points. Since the electron density of the free atom, i.e. the single atom *in vacuo* isolated from the rest of the molecule in a neutral charge state, is trivially available for each atom type (from here on called species) within FHI-aims as splined radial functions, the grid radii here are obtained by inverting the species-specific radial density spline functions  $\varrho_{\text{spec}}^{\text{free}}(r)$  and evaluating the inverted function  $r_{\text{spec}}^{\text{free}}(\varrho)$  at the iso-density value,

$$R_i = r_{\text{spec}(J)}^{\text{free}}(\varrho_{\text{iso}}), \quad (5.1)$$

where  $\text{spec}(J)$  is a function which returns the species of atom  $J$ . For all atoms of a certain species present in a given molecule,  $R_i$  thus only needs to be determined once. At least in the case of neutral molecules, this places the density-walkers at a good starting point.

The next figure to be determined is the number of points that should be initialized on these spheres. This is a discrete problem since the employed LL grids are only defined for a certain number of points, i.e.

$$M_J \in \{6, 14, 26, 38, \dots, 5294, 5810\}. \quad (5.2)$$

Obviously, the method is generally not limited to 5810 points but an LL grid with more points has simply not been implemented in FHI-aims so far. With LL spheres being placed on all centers, it is nonetheless typically very easy to generate enough points and this possible limitation has never been an issue in any application encountered during the work presented here. The major complication that arises, however, is the overlap between LL spheres on different centers. Grid points of a given center that would reside within, or on the border of one or several spheres placed around other centers need to be relocated or, as will be done here, discarded. Thus, during initialization a certain number of grid points is lost. This loss is proportional to the overlap between LL spheres and therefore depends on the geometry of the molecule. Instead of trying to find an exact expression for  $M_J$  in general—which we consider a hardly feasible task—we can estimate the overlap between different spheres through an analytic correction without a need for iterative refinement. To this end we determine  $M_J$  under the assumptions that

- the molecule is spherical, i.e. its surface,  $O_{\text{mol}}$ , to volume,  $V_{\text{mol}}$ , ratio is given by

$$O_{\text{mol}} \propto V_{\text{mol}}^{\frac{2}{3}}, \quad (5.3)$$

- $V_{\text{mol}}$  is simply the sum of all atomic LL spheres' volumes,  $V_J$ , i.e., the overlap between different spheres exactly compensates for the “empty” volume within the assumed molecular sphere,

$$V_{\text{mol}} = V_{\text{tot}} = \sum_{J=1}^N V_J, \quad (5.4)$$

- and the points are evenly distributed such that the desired point density on the molecular surface can be directly equated to the ratio of  $M_J$  points on any atomic sphere to its surface area  $O_J$ ,

$$\frac{M}{O_{\text{mol}}} = \frac{M_J}{O_J}. \quad (5.5)$$

Note that—in contrast to the volumes—the atomic surface areas do not, in general, sum up to the molecular value. Solving Eq. (5.5) for the unknown number of points on the atomic grid,  $M_J$ , the connection to the atomic quantities can be made by first using Eq. (5.3),

$$M_J = M \left( \frac{V_J}{V_{\text{mol}}} \right)^{\frac{2}{3}}, \quad (5.6)$$

and then Eq. (5.4) together with the simple formula for spherical volumes,  $V_J \propto R_J^3$ , to obtain the solution,

$$M_J = M \left( \frac{R_J^3}{\sum_{J=1}^N R_J^3} \right)^{\frac{2}{3}}. \quad (5.7)$$

With the previously determined LL sphere radii  $R_J$  and  $M$  being known from Eq. (4.6), Eq. (5.7) can be used to directly calculate the number of grid points per atom which will be rounded to the next larger integer number for which an LL grid is defined.

In the current implementation, the problem is even further simplified. Assuming that all atomic spheres (with volume  $V_J$  and surface area  $O_J$ ) are of the same size, i.e.

$$R_1 = R_2 = \dots = R_N, \quad (5.8)$$

the number of points per sphere is simply

$$M_J \approx M \cdot N^{-\frac{2}{3}}. \quad (5.9)$$

This rather crude approximation has proved to work well for all test cases investigated here such that in the final result rather more points than required by a certain degree of determination,  $d_{\text{det}}$ , are created. Unfortunately, this overestimation depends on the geometry of the molecule and is bad in terms of computational costs but the clear advantage is that the MPE equations never end up under-determined.

### 5.1.2 Overlapping the Atomic Spheres

Having created LL grids at all centers  $J$  with radius  $R_J$ , the next step is to identify all points that reside on the actual cavity surface. This is done by removing those points belonging to a center  $J$  that end up inside another center  $K$ 's atomic sphere due to overlap of the two spheres. Given a set of points  $\mathbf{p}_{J,i}$  on  $J$ 's LL grid defined by the center's position vector  $\mathbf{r}_J$  and a radial direction

vector  $\mathbf{R}_i$  with length  $R_J$ ,

$$\mathbf{p}_{J,i} = \mathbf{r}_J + \mathbf{R}_{J,i}, \quad (5.10)$$

two extreme cases that affect all those points can be identified:

- (A) No overlap between the spheres around  $J$  and  $K$  is possible, or
- (B) every point belonging to  $J$  resides within the sphere around  $K$ .

Mathematically, the criteria can be formulated as follows: The distance between all points  $\mathbf{p}_{J,i}$  to another center  $K$

- (A) always exceeds that center's grid radius,

$$\|\mathbf{p}_{J,i} - \mathbf{r}_K\|_2 > R_K, \quad K \neq J, \quad \forall i, \quad (5.11)$$

or

- (B) never exceeds that center's grid radius,

$$\|\mathbf{p}_{J,i} - \mathbf{r}_K\|_2 \leq R_K, \quad K \neq J, \quad \forall i. \quad (5.12)$$

Using the reverse triangle inequality,

$$\|\mathbf{p}_{J,i} - \mathbf{r}_K\|_2 = \|\mathbf{R}_{J,i} + \mathbf{r}_J - \mathbf{r}_K\|_2 \geq \left| R_J - \|\mathbf{r}_K - \mathbf{r}_J\|_2 \right|, \quad (5.13)$$

one finds that a sufficient condition for (A) is

$$\left| R_J - \|\mathbf{r}_K - \mathbf{r}_J\|_2 \right| > R_K. \quad (5.14)$$

Since the centers can safely be assumed to be further apart than the radius of the sphere around  $J$  in this case,

$$R_J < \|\mathbf{r}_K - \mathbf{r}_J\|_2, \quad (5.15)$$

one can derive the following sufficient condition for case (A) from Eq. (5.14),

$$\|\mathbf{r}_K - \mathbf{r}_J\|_2 > R_K + R_J, \quad (5.16)$$

or, in words, the distance between the centers of the spheres needs to be greater than the sum of their radii.

A sufficient condition for case (B) can be obtained in a very similar way,

$$\|\mathbf{r}_K - \mathbf{r}_J\|_2 \leq R_K - R_J, \quad (5.17)$$

where we have used the triangle inequality

$$\|\mathbf{p}_{J,i} - \mathbf{r}_K\|_2 = \|\mathbf{R}_{J,i} + \mathbf{r}_J - \mathbf{r}_K\|_2 \leq R_J + \|\mathbf{r}_J - \mathbf{r}_K\|_2. \quad (5.18)$$

Both conditions for the cases (A), Eq. (5.16), and (B), Eq. (5.17), depend only on the position of the centers  $J$  and  $K$  and the spheres' radii,  $R_J$  and  $R_K$ , and not on the actual position vectors. Identifying either case can help to reduce the computational effort of an otherwise necessary point-by-point checking if a point is situated within another sphere and should be discarded, i.e. testing

$$\|\mathbf{p}_{J,i} - \mathbf{r}_K\|_2 \leq R_K, K \neq J, \quad (5.19)$$

for every possible  $i$ . Instead, (B) leads to a rejection of all points belonging to center  $J$  while (A) leaves all of them untouched for comparison with further centers.

After the exclusion of any internal points due to the overlap of spherical grids, the generated set of points corresponds to the vdW cavity shown in Fig. 3.2. Potentially occurring discontinuities of the normal vectors on this surface, however, can lead to numerical problems in the evaluation of the electrostatic boundary conditions, cf. Eq. (3.45b). Rather than directly being used in the MPE equations, the obtained points thus only serve as an initial guess for the next step, in which an optimization shapes them into a smooth cavity similar to an SES.

## 5.2 Walker Dynamics Simulation

### 5.2.1 Forces

Once the initialization of the walkers' starting positions described above is completed, a molecular dynamics simulation is conducted with the walkers moving on a fictitious potential energy hypersurface designed to yield a faithful representation of the density iso-surface, even spacing of walkers and a fast convergence. To that end, the following forces act on each walker:

$\mathbf{F}_d$  ("density force")

acts along the electron density gradient and draws the walkers towards the desired iso-density value

$$\mathbf{F}_d(\mathbf{r}_i) = -\delta_i^{e,\text{rel}} k_d f_d \frac{\nabla \varrho(\mathbf{r}_i)}{\|\nabla \varrho(\mathbf{r}_i)\|_2} \quad (5.20)$$

with the relative deviation from the desired iso-density value  $\delta_i^{e,\text{rel}}$

$$\delta_i^{e,\text{rel}} = \frac{\varrho(\mathbf{r}_i)}{\varrho_{\text{iso}}} - 1 \quad (5.21)$$

a specified force constant  $k_d$ , and an enhancement factor

$$f_d = \max \left( 1, \frac{f_0}{\max_i |\delta_i^{e,\text{rel}}|} \right) \quad (5.22)$$

which increases the density force as soon as the walker ensemble approaches the desired iso-density value such that this force has (at least) a constant norm of  $k_d f_0$  for the walker with the largest absolute relative deviation.

$\mathbf{F}_g$  (“gravitation force”)

accelerates density-walkers towards the center of mass of the system,  $\mathbf{R}_0$ , if the density gradient is too close to zero, to avoid numerical problems at low charge densities

$$\mathbf{F}_g(\mathbf{r}_i) = -k_g \frac{\mathbf{r}_i - \mathbf{R}_0}{\|\mathbf{r}_i - \mathbf{R}_0\|_2} \quad (5.23)$$

where  $k_g$  is a force constant.

$\mathbf{F}_r$  (“repulsive force”)

creates pairwise repulsive interaction between the walkers and leads to a more even point distribution on the iso-density surface

$$\mathbf{F}_r(\mathbf{r}_i, \mathbf{r}_j) = k_r \frac{\mathbf{q}_{ij}}{\|\mathbf{q}_{ij}\|_2} \frac{1}{s_{ij}^2} \quad (5.24)$$

The direction of the repulsive force,  $\mathbf{q}_{ij}$  is determined by the relative distance vector between the involved sampling points,  $\mathbf{r}_{ij} = \mathbf{r}_j - \mathbf{r}_i$ , where the component along the density gradient is projected out such that it is perpendicular to the density force

$$\mathbf{q}_{ij} = \left( 1 - \frac{(\nabla\varrho(\mathbf{r}_i)) \cdot (\nabla\varrho(\mathbf{r}_i))^T}{\|\nabla\varrho(\mathbf{r}_i)\|_2^2} \right) \mathbf{r}_{ij} \quad (5.25)$$

The effective interaction distance  $s_{ij}$  is obtained by scaling of the Cartesian distance between the interacting points accounting approximately for the local curvature of the cavity

$$s_{ij}^2 = \|\mathbf{r}_{ij}\|_2^2 \left( 1 + \frac{1 - \cos \theta_{ij}}{6} + \frac{(1 - \cos \theta_{ij})^2}{22.5} \right) \quad (5.26)$$

with

$$\cos \theta_{ij} = \frac{(\nabla\varrho(\mathbf{r}_i)) \cdot (\nabla\varrho(\mathbf{r}_j))}{\|\nabla\varrho(\mathbf{r}_i)\|_2 \cdot \|\nabla\varrho(\mathbf{r}_j)\|_2} \quad (5.27)$$

A derivation of Eq. (5.26) is given in appendix C.2.

### 5.2.2 Walker Propagation

Given the position vector,  $\chi_i(t)$ , at time  $t$  and the momentum vector,  $\varphi_i(t - \Delta t/2)$ , of a previous half-step (initially set to zero) of any given density walker  $i$ , the propagation of position and momentum is done through the following steps:

1. Evaluate the density at all positions  $\chi_i(t)$  and calculate the relative deviation from the iso-density value, Eq. (5.21).
2. Find the largest absolute value of  $\delta_i^{\varrho, \text{rel}}$  among all walkers and check whether it is below a

certain threshold,  $\delta^{\rho, \text{rel}, \text{thresh}}$ . When

$$\left| \delta_i^{\rho, \text{rel}} \right| < \delta^{\rho, \text{rel}, \text{thresh}} \quad \forall i, \quad (5.28)$$

the iso-density surface has been found (up to the required accuracy) and the loop terminates.

3. Otherwise, determine the density force  $F_{d,i}(\chi_i)$  (reusing the previously obtained information) and other forces that act on walker  $i$ , cf. section 5.2.1. Sum up all forces of each walker to  $F_i(\chi_i)$ .
4. Update the momentum,

$$\boldsymbol{\varphi}_i(t + \Delta t/2) \leftarrow \boldsymbol{\varphi}_i(t - \Delta t/2) + F_i(\chi_i(t))\Delta t, \quad (5.29)$$

and

5. rescale it afterwards,

$$\tilde{\boldsymbol{\varphi}}_i(t + \Delta t/2) \leftarrow (1 - \eta) \boldsymbol{\varphi}_i(t + \Delta t/2), \quad (5.30)$$

using a friction coefficient  $\eta$  where  $0 \leq \eta < 1$ .

6. Update the walker's position,

$$\chi_i(t + \Delta t) \leftarrow \chi_i(t) + \frac{\tilde{\boldsymbol{\varphi}}_i(t + \Delta t/2)}{\mu_i} \Delta t, \quad (5.31)$$

where  $\mu_i$  is the walker's mass. For the sake of simplicity we assign the same mass to all walkers and use this value as the unit of mass e.g. for the force constants, i.e.  $\mu_i = 1$ .

7. Finally, increase the time by  $\Delta t$ ,

$$t \leftarrow t + \Delta t, \quad (5.32)$$

and start again from 1.

This propagation algorithm is a modification of the Leapfrog time integration method which in turn is similar to the well-known Velocity-Verlet algorithm. Apart from the simple rearrangement of steps, the only real difference arises from step 5 when the momenta are rescaled. This serves to drain kinetic energy from the walkers which they accrue during the simulation when moving towards the minimum of the potential defined by the aforementioned forces, cf. section 5.2.1. With no or just a very small value for the friction constant  $\eta$ , the walkers may start to oscillate around the desired iso-density value which is clearly undesirable. A too large value of  $\eta$ , however, can severely restrict the walkers' mobility and require many more steps until the minimum is found. Therefore, picking an optimal value for  $\eta$  is crucial for the efficiency of the method.

It should be noted here that a second termination criterion is given by a maximum number of allowed steps,  $n_{\text{max}}$ , after which the program's execution is aborted in order to avoid a possible infinite loop. This condition usually indicates a bad choice of parameters which can lead to extremely slow convergence or to walkers getting "stuck" during the dynamics.



Tab. 5.1: Exemplary Set of Parameters for the Cavity Sampling Algorithm<sup>a</sup>

| parameter  | value |                                      |       |
|------------|-------|--------------------------------------|-------|
| $k_d$      | 1     | $f_0$                                | 0.1   |
| $k_g$      | 5     | $\delta \varrho_{\text{rel,thresh}}$ | 0.01  |
| $k_r$      | 0.01  | $n_{\text{max}}$                     | 500   |
| $\Delta t$ | 0.1   | $r_{\text{kill}}$                    | 0.001 |
| $\eta$     | 0.2   | $n_{\text{update}}$                  | 50    |

<sup>a</sup> as employed in this work for the molecular dynamics simulation with density walkers for small organic molecules (see e.g. chapter 6). Reprinted with permission from Ref. [1]. © 2017 American Chemical Society.

### 5.2.3 Walker Elimination and Neighbor Lists

After each  $n_{\text{update}}$  cycles during step 3 in the aforementioned propagation loop, a certain ratio  $r_{\text{kill}}$  of walkers furthest away from the iso-density value is discarded. This serves to eliminate walkers trapped in the electronic density hyper-surface’s potential local minima above (or local maxima below) the iso-density value. For small values of  $r_{\text{kill}}$ , this has little to no influence on the distribution of walkers.

Thereafter, the distances between all pairs of walkers are calculated. This information is used to determine neighbor lists for all walkers which list all other walkers closer than a certain distance threshold. The value of the latter is calculated once after the density walkers’ initialization based on the average distance between walkers assuming that this quantity does not change significantly during the simulation.

### 5.2.4 Parameters

It is important to note here that the parameters of this fictitious dynamics exert no influence over the final shape of the cavity—as it is entirely determined by the density—and have only minor impact on the final distribution of walkers. Rather, the choice of parameters governs the rate of convergence of walkers towards the optimal point distribution. A parameter set yielding fast convergence for the systems we considered is given in Tab. 5.1. Efficiency and accuracy of this method of cavity generation will be discussed in more detail below. An example of such a cavity for morpholine, an organic molecule taken from the test-set T1 defined in section 6.1 below, is illustrated in Fig. 5.1.

## 5.3 Which Density?

Solvation cavities based on electron densities inherently allow for different approaches, depending on which density is being used. Besides the common choice between a “fixed” initial guess,  $\varrho_{\text{solute}}^{\text{init}}$ , for the density—possibly from restart information—or the “self-consistent” total electron density  $\varrho_{\text{solute}}^{\text{sc}}$  being converged during the SCF cycle, the current implementation also offers a third option, namely the superposition of “free” atom densities,  $\varrho_{\text{solute}}^{\text{free}}$ . In FHI-aims,  $\varrho_{\text{solute}}^{\text{free}}$  is readily available as it is used to regularize the total density [22].

The main difference between these options is that in the “fixed” and “free” case the cavity is sampled only once—from  $\varrho_{\text{solute}}^{\text{init}}$  or  $\varrho_{\text{solute}}^{\text{free}}$ —and kept fixed through the rest of the calculation. With

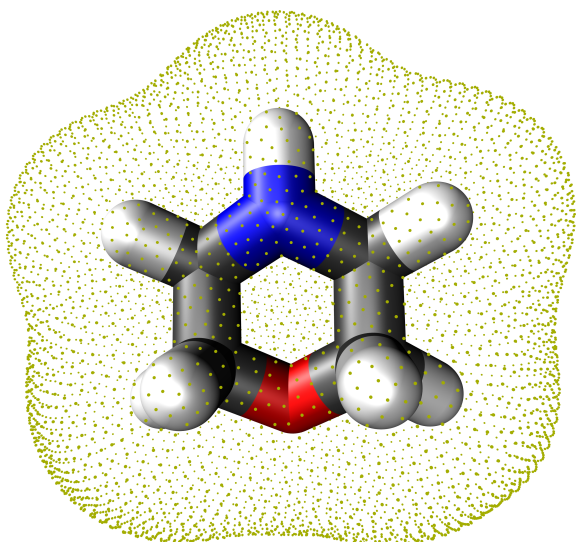


Fig. 5.1: Schematic picture of a small organic molecule (morpholine) surrounded by evenly distributed points (light-green dots) representing the iso-density cavity. Reprinted with permission from Ref. [1]. © 2017 American Chemical Society.

the “self-consistent” cavity option, on the other hand, the cavity is adapted to the current total electron density  $\rho_{\text{solute}}^{\text{SC}}$  in every SCF step. Considering that the MPE equations only have to be solved fully once when the cavity does not change during the SCF cycle (cf. section 4.2), the “fixed” and “free” cavity options potentially offer greater savings in computational cost compared to the “self-consistent” one.

A different aspect concerns the dependence of the “fixed” approach to  $\rho_{\text{solute}}^{\text{init}}$ , i.e., the density used to initialize the cavity. Tests on small molecules (cf. chapter 6) indicate that the converged electron density of a calculation *in vacuo* is perfectly suitable to be used as  $\rho_{\text{solute}}^{\text{init}}$  as it usually leads to very similar results compared to the “self-consistent” solution—provided that the model is parametrized properly. Most applications presented later on involve the calculation of the free energy of solvation  $\Delta G_{\text{sol}}$ , cf. Eq. (3.50). In these cases, the additional vacuum calculation from which  $\rho_{\text{solute}}^{\text{init}}$  can be extracted is required anyway. In other cases, however, this calculation might be unnecessary otherwise. Furthermore, the “fixed” approach requires information to be stored between the two separate calculations *in vacuo* and with the continuum solvation model. All of this is needed neither in the “self-consistent” nor in the “free” option which are both uniquely defined by the information available within the single, implicit solvent calculation.

Keeping in mind that the shape of the solvation cavity is one of the parameters of the model, it is not obvious which of the three options is the optimal choice. In the interest of computational efficiency, all subsequent parameterizations (cf. e.g. section 6.1) are performed either with the “fixed” or with the “free” option.

## 5.4 Calculation of Surface Area and Volume

For the iso-density based continuous cavity functions, volume and surface area—as e.g. needed in the calculation of non-electrostatic free energy contributions—are easily obtainable by spatial

integration [21, 68]. In the case of step like functions represented as a set of points at the dielectric interface, they are not as accessible. We therefore describe here a straightforward way to determine  $O$  and  $V$  relying only on the collection of points and their respective local coordinate systems.

Our algorithm is based on a partitioning of the total cavity surface into local patches assigned to each point on the surface. It is thus by construction highly parallel with respect to the cavity points, as it only requires knowledge of the local neighborhood of each processed point, e.g. all points that are closer than a certain distance threshold [82]. Currently, we have implemented a simple linear search to find a desired number of nearest neighbors (usually around 30). The complexity of this approach is  $\mathcal{O}(M^2)$  where  $M$  is the number of points on the cavity surface. While the cost of this neighbor search is negligible for the systems investigated in this work, it might become a bottleneck when going to very large point clouds. In such cases, one could consider using faster algorithms like space partitioning or k-d tree schemes with a typical average complexity of  $\mathcal{O}(M \log M)$ .

#### 5.4.1 Local Coordinate System

Having determined an evenly distributed set of points  $\mathbf{p}$  on the cavity surface,  $\mathcal{C}(\mathbf{p}) = 0$ , the first step is to construct a local Cartesian coordinate system  $\{\mathbf{t}_{p,1}, \mathbf{t}_{p,2}, \mathbf{n}_p\}$  such that  $\mathbf{n}_p$  is the vector locally perpendicular to the interface and  $\mathbf{t}_{p,1}, \mathbf{t}_{p,2}$  are two local tangent vectors—as already illustrated in Fig. 3.1. In many density functional approximations such as GGA, density gradients are already used in the energy calculation such that  $\mathbf{n}_p$  can be taken as the normalized local gradient at no additional computational cost.

$$\mathbf{n}_p = \frac{\nabla\varrho(\mathbf{p})}{\|\nabla\varrho(\mathbf{p})\|_2} \quad (5.33)$$

A similar approach has been used previously in this work to define the forces in the molecular dynamics simulation of walkers. The tangent vectors  $\mathbf{t}_{p,1}$  and  $\mathbf{t}_{p,2}$  are then chosen such as to fulfill the conditions

$$\mathbf{t}_{p,1} \times \mathbf{t}_{p,2} = \mathbf{n}_p, \quad (5.34)$$

and

$$\mathbf{t}_{p,1} \cdot \mathbf{t}_{p,2} = 0. \quad (5.35)$$

Yet, these leave the rotation of the tangent vectors around  $\mathbf{n}_p$  as an arbitrary remaining degree of freedom. For the sake of simplicity we therefore align  $\mathbf{t}_{p,1}$  perpendicular to the  $z$  direction of the global coordinate system, if possible, otherwise perpendicular to the  $x$ -axis.

#### 5.4.2 Voronoi Construction in Local Projection

The subsequent construction is illustrated in Fig. 5.2 to aid the reader follow the procedure. First, the neighboring points  $\mathbf{q}_i$  are projected into the plane that is spanned by the tangent vectors  $\mathbf{t}_{p,1}$

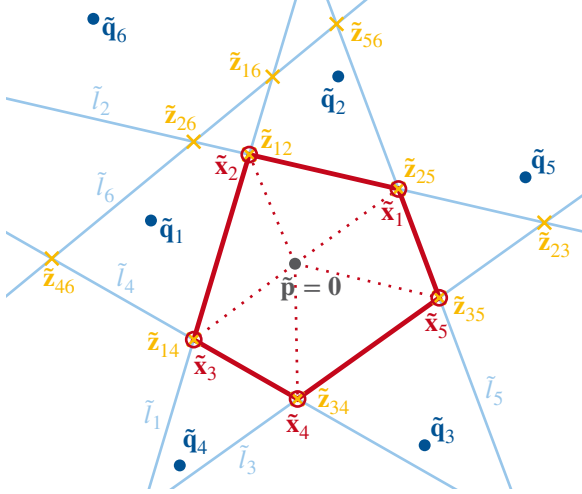


Fig. 5.2: Schematic picture of the Voronoi-tessellation of point  $\mathbf{p}$  with origin  $\tilde{\mathbf{p}}$  (gray dot).  $\tilde{\mathbf{q}}_i$  (blue dots) are the relative coordinates of neighboring points  $\mathbf{q}_i$  with respect to  $\mathbf{p}$  projected into the plane spanned by the tangent vectors of point  $\mathbf{p}$  (see text). The perpendicular bisectors (light blue lines) between each point  $\tilde{\mathbf{q}}_i$  and  $\tilde{\mathbf{p}}$  are denoted  $\tilde{l}_i$ . A subset of the bisecting lines' intersection points  $\tilde{\mathbf{z}}_{ij}$  (yellow crosses), denoted  $\tilde{\mathbf{x}}_m$  (red circles), forms the Voronoi cell (bordered by the red line). This cell is further divided (indicated by dashed lines) into non-overlapping triangles each formed by two successive points  $\tilde{\mathbf{x}}_{m/m'}$  and point  $\tilde{\mathbf{p}}$ . Reprinted with permission from Ref. [1]. © 2017 American Chemical Society.

and  $\mathbf{t}_{p,2}$  of point  $\mathbf{p}$  (as defined above),

$$\tilde{\mathbf{q}}_i = \begin{pmatrix} \tilde{q}_{i,1} \\ \tilde{q}_{i,2} \end{pmatrix} = \begin{pmatrix} \mathbf{t}_{p,1} \cdot (\mathbf{q}_i - \mathbf{p}) \\ \mathbf{t}_{p,2} \cdot (\mathbf{q}_i - \mathbf{p}) \end{pmatrix}. \quad (5.36)$$

These projections are collected in the set  $\mathcal{Q} = \{\tilde{\mathbf{q}}_i\}$ . The perpendicular bisector  $\tilde{l}_i$  between the (local) origin and  $\tilde{\mathbf{q}}_i$  in this projection is given by

$$\tilde{l}_i : \tilde{\mathbf{I}}(\lambda_i) = \frac{1}{2}\tilde{\mathbf{q}}_i + \lambda_i\tilde{\mathbf{v}}_i \quad (5.37)$$

where  $\tilde{\mathbf{v}}_i$  is the (not normalized) direction vector perpendicular to the connecting line

$$\tilde{\mathbf{v}}_i = \begin{pmatrix} 0 & -1 \\ 1 & 0 \end{pmatrix} \tilde{\mathbf{q}}_i = \begin{pmatrix} -\tilde{q}_{i,2} \\ \tilde{q}_{i,1} \end{pmatrix} \quad (5.38)$$

Then, for all pairs of lines,  $\tilde{l}_i$  and  $\tilde{l}_j$ , that are not collinear, i.e.  $\tilde{q}_{i,1}\tilde{q}_{j,2} \neq \tilde{q}_{j,1}\tilde{q}_{i,2}$ , the intersection point,  $\tilde{\mathbf{z}}_{ij}$ , is calculated

$$\tilde{\mathbf{z}}_{ij} = \frac{1}{2} \begin{pmatrix} \tilde{q}_{i,1} \\ \tilde{q}_{i,2} \end{pmatrix} + \frac{1}{2} \frac{\tilde{q}_{j,2}(\tilde{q}_{j,2} - \tilde{q}_{i,2}) + \tilde{q}_{j,1}(\tilde{q}_{j,1} - \tilde{q}_{i,1})}{\tilde{q}_{i,1}\tilde{q}_{j,2} - \tilde{q}_{j,1}\tilde{q}_{i,2}} \begin{pmatrix} -\tilde{q}_{i,2} \\ \tilde{q}_{i,1} \end{pmatrix} \quad (5.39)$$

A derivation of Eq. (5.39) is shown in appendix C.1.

From the set of intersection points  $Z = \{\tilde{\mathbf{z}}_{ij}\}$ , the ones that actually span the Voronoi cell need to be isolated. To this end, all points are discarded which are separated from the (local) origin by any bisecting line  $\tilde{l}_k$ . This can equivalently be expressed in terms of projections on the corresponding position vector  $\tilde{\mathbf{q}}_k$ ,

$$\tilde{\mathbf{x}}_m \in \left\{ \tilde{\mathbf{z}}_{ij} \left| \tilde{\mathbf{z}}_{ij} \in Z, \left( \tilde{\mathbf{z}}_{ij} - \frac{1}{2} \tilde{\mathbf{q}}_k \right) \cdot \tilde{\mathbf{q}}_k \leq 0 \forall \tilde{\mathbf{q}}_k \in Q \right. \right\}. \quad (5.40)$$

### 5.4.3 Calculation of Area and Volume Elements

The remaining points  $\tilde{\mathbf{x}}_m$  span the Voronoi cell and are sorted with respect to increasing angles between their position vector and one axis of the local coordinate system. This quantity is trivially obtainable by supplying  $\tilde{\mathbf{x}}_m$ 's coordinates to the intrinsic Fortran function  $\text{atan2}(y, x)$ . The cell is now divided into triangles each formed by two (in this sorting) successive points—including the pair of last and first point—and the (local) origin. Again, the described procedure is illustrated in Fig. 5.2.

Calculating the area,  $\tilde{o}_m$ , of these triangles is straightforward, for example

$$\tilde{o}_m = \frac{1}{2} \left| \tilde{x}_{m,1} \tilde{x}_{m+1,2} - \tilde{x}_{m+1,1} \tilde{x}_{m,2} \right| \quad (5.41)$$

for spanning point  $\tilde{\mathbf{x}}_m$  and its successor  $\tilde{\mathbf{x}}_{m+1}$ .

To account for the local curvature of the cavity surface, an optional correction factor of

$$c_m = \frac{2}{1 + \sqrt{\frac{1}{2} + \mathbf{n}_p \cdot \frac{\mathbf{n}_{q_{i_1}} + \mathbf{n}_{q_{i_2}} + \mathbf{n}_{q_{i_3}} + \mathbf{n}_{q_{i_4}}}{8}}} \quad (5.42)$$

can applied, where  $\mathbf{n}_{i_1}$  to  $\mathbf{n}_{i_4}$  are the normal vectors of the neighboring points  $\mathbf{q}_{i_1}$  to  $\mathbf{q}_{i_4}$  which created the two intersections involved. Note that we refer here to the original points and not their projections. Using the example illustrated in Fig. 5.2, the correction factor for the area  $\tilde{o}_2$  spanned by points  $\tilde{\mathbf{x}}_2$ ,  $\tilde{\mathbf{x}}_3$ , and the (local) origin  $\tilde{\mathbf{p}}$  would be

$$c_2 = \frac{2}{1 + \sqrt{\frac{1}{2} + \mathbf{n}_p \cdot \frac{\mathbf{n}_{q_2} + 2\mathbf{n}_{q_1} + \mathbf{n}_{q_4}}{8}}}, \quad (5.43)$$

since  $\tilde{\mathbf{x}}_2 = \tilde{\mathbf{z}}_{12}$  is the intersection of bisecting lines  $\tilde{l}_1$  and  $\tilde{l}_2$ , and  $\tilde{\mathbf{x}}_3 = \tilde{\mathbf{z}}_{14}$  the one of  $\tilde{l}_1$  and  $\tilde{l}_4$ . A full derivation of Eq. (5.42) is given in appendix C.3. The total area element  $O_p$  assigned to point  $\mathbf{p}$  is simply the sum of the corrected triangle areas,

$$O_p = \sum_m c_m \tilde{o}_m. \quad (5.44)$$

From the area elements of the Voronoi-tessellated surface, *signed* volume elements,  $\tilde{v}_m$ , can be derived by forming pyramids with an arbitrary (global) origin,  $\mathbf{o}$ .

$$\tilde{v}_m = \frac{h}{3} c_m \tilde{o}_m \quad (5.45)$$

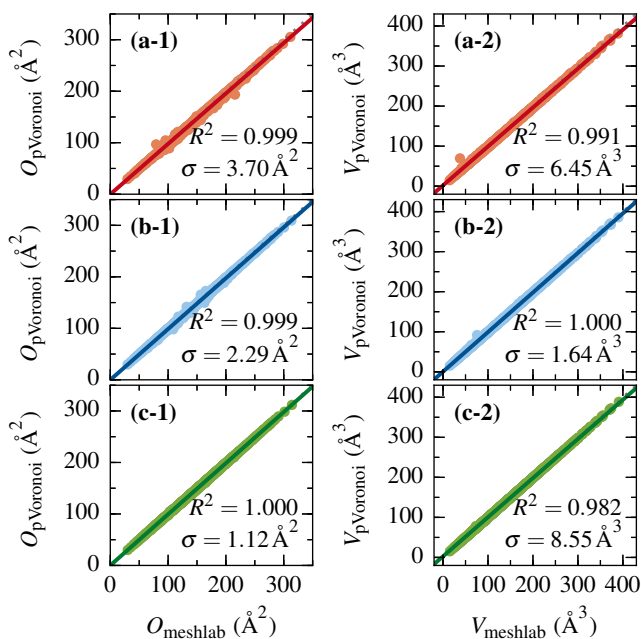


Fig. 5.3: Correlation between surface areas (left column) and volumes (right column) obtained by applying the MeshLab [83] tool and the method presented in this work to cavities generated for small molecules at various iso-density values (cf. section 6.1). Results are shown for point densities of the point clouds that yield a degree of determination,  $d_{\text{det}}$ , of the MPE equations of approximately (a) two, (b) four, and (c) eight for the respective systems at expansion orders of  $l_{\text{max,R}} = 6$  and  $l_{\text{max,Q}} = 6$ . Reprinted with permission from Ref. [1]. © 2017 American Chemical Society.

Since the *signed* height of these pyramids is defined by the *signed* distance of  $\mathbf{o}$  and the plane of the Voronoi cell,

$$h = (\mathbf{o} - \mathbf{p}) \cdot \mathbf{n}_p \quad (5.46)$$

it is the same for all elements belonging to a single point  $\mathbf{p}$ . Thus, the cavity volume assigned to a single point can trivially be determined from the area element without knowledge of the tessellation,

$$V_p = \sum_m v_m = \sum_m \frac{h}{3} c_m \tilde{\delta}_m = \frac{h}{3} O_p. \quad (5.47)$$

The total surface area  $O$  and the total volume  $V$  of the cavity are then simply given by the sum of all points' increments  $O_p$  and  $V_p$ . The choice of the origin is thereby mostly arbitrary, as volume elements outside the cavity would simply cancel out. Yet, for reasons of numerical accuracy it can be advantageous to pick an  $\mathbf{o}$  near the center of the solute.

As illustrated in Fig. 5.3, the method presented here has been verified by comparing obtained point cloud measures for small organic molecules (see section 6.1) with reference calculations with the open source tool MeshLab's [83] ball pivoting and geometric measures tools. This comparison indicates an excellent agreement of both methods for the systems under investigation even for

the lowest point densities employed here.

## 6 MPE Model Parametrization ‡

---

As with any effective model, our approach contains a number of parameters, which need to be determined for the application, e.g. with DFT calculations for given solute molecules. As previously presented in section 3.4, we apply the non-electrostatic solvation free energy model of Andreussi et al. [21] as a non self-consistent post-SCF correction—thus keeping the shape of the solvation cavity independent of non-electrostatic contributions [42]. The reaction field and thus also the free energy of solvation of our model, cf. Eq. (3.50), is a function of three free parameters: The first of these,  $\varrho_{\text{iso}}$ , is the already discussed density iso-value influencing the shape of the solvation cavity, its surface area and volume. The other two,  $\alpha$  and  $\beta$ , are effective parameters describing surface tension as well as dispersion and excluded volume effects of the solvent.

In order to parametrize and benchmark the MPE model for real systems, we will fit calculated free energies of solvation to experimentally measured values for different test sets of small organic molecules that will be presented in the following.

### 6.1 Test Sets

For the parametrization of our model, we utilize different test-sets with experimentally measured free energies of hydration for

- (T1) 239 organic molecules [84] and water [85],
- (T2) 274 neutral solutes including the water dimer,
- (T3) 52 singly-charged (unclustered) cations,
- (T3c) 52 singly-charged, selectively clustered cations,
- (T4) 60 singly-charged (unclustered) anions, and
- (T4c) 60 singly-charged, selectively clustered anions.

Molecular geometries for T1 have been provided by Andreussi et al. as used in their earlier work [21]. The other test-sets (T2, T3, T3c, T4 and T4c) are part of the Minnesota solvation database, version 2012 [86]. T2 thereby corresponds to subset “[a]” of the full database while T3 and T4 form subset “[i]”, both of which are described in detail in the Minnesota database manual [86]. T3c is almost identical to T3 except for 8 molecules that are selectively clustered with a single water molecule in set T3c. The same relationship holds for T4 and T4c with 23 selectively clustered molecules in T4c [48].

---

‡Reprinted in parts with permission from Ref. [1]. © 2017 American Chemical Society.



## 6.2 Fitting Procedure

In order to minimize the computational effort which mostly stems from the required DFT calculations, we use the following parametrization scheme for a first search of the parameter space:

1. For a given molecule  $M$  in the fitting set,  $\Delta G_{\text{el},M}(\varrho_{\text{iso}})$ ,  $O_M(\varrho_{\text{iso}})$ , and  $V_M(\varrho_{\text{iso}})$  depend on  $\varrho_{\text{iso}}$  (which defines the cavity shape), but not on the other fitting parameters,  $\alpha$  and  $\beta$ . For a small number ( $< 10$ ) of different iso-density values picked from the range from  $\varrho_{\text{iso},\text{min}} = 1 \text{ me \AA}^{-3}$  to  $\varrho_{\text{iso},\text{max}} = 100 \text{ me \AA}^{-3}$  where the optimal value is expected to be found, DFT calculations are performed. The obtained  $\Delta G_{\text{el},M}(\varrho_{\text{iso}})$ ,  $O_M(\varrho_{\text{iso}})$ , and  $V_M(\varrho_{\text{iso}})$  are in the following called nodes.
2. Based on all (explicitly calculated) nodes, the analytical spline representations  $\Delta G_{\text{el},M}^{\text{spl}}(\varrho_{\text{iso}})$ ,  $O_M^{\text{spl}}(\varrho_{\text{iso}})$ , and  $V_M^{\text{spl}}(\varrho_{\text{iso}})$  are constructed using univariate cubic splines<sup>1</sup> as provided by the open-source software package SciPy [87].
3. The deviation from the experimentally measured solvation free energy  $\Delta G_{\text{sol,ref},M}$  for each individual molecule can then analytically be expressed by

$$d_M^{\text{spl}}(\varrho_{\text{iso}}, \alpha, \beta) = \Delta G_{\text{el},M}^{\text{spl}}(\varrho_{\text{iso}}) + \alpha O_M^{\text{spl}}(\varrho_{\text{iso}}) + \beta V_M^{\text{spl}}(\varrho_{\text{iso}}) - \Delta G_{\text{sol},M}^{\text{exp}}. \quad (6.1)$$

Note that this is just an approximation of the actual deviation,  $d_M$ , unless the chosen value of  $\varrho_{\text{iso}}$  falls directly on a node.

4. We perform a minimization of the sum of squared deviations for all molecules,

$$D^{\text{spl}}(\varrho_{\text{iso}}, \alpha, \beta) = \sum_M \left( d_M^{\text{spl}}(\varrho_{\text{iso}}, \alpha, \beta) \right)^2, \quad (6.2)$$

using the L-BFGS-B minimization method [88, 89] as provided by the open-source software package SciPy [87] under the boundary condition that

$$\varrho_{\text{iso},\text{min}} \leq \varrho_{\text{iso}} \leq \varrho_{\text{iso},\text{max}},$$

to avoid extrapolation errors for the splined functions. Due to the low dimensionality of the optimization problem, we can ensure to find the global minimum by using  $9 \times 9 \times 9$  different sets of starting parameters for the optimization in the ranges

$$\varrho_{\text{iso}} \in \left[ \varrho_{\text{iso},\text{min}}, \varrho_{\text{iso},\text{max}} \right], \quad (6.3a)$$

$$\alpha \in \left[ -100 \text{ meV \AA}^{-2}, 100 \text{ meV \AA}^{-2} \right], \quad (6.3b)$$

and

$$\beta \in \left[ -100 \text{ meV \AA}^{-3}, 100 \text{ meV \AA}^{-3} \right]. \quad (6.3c)$$

<sup>1</sup>We use a smoothing factor of  $s = 1$  for  $O$  and  $V$  (due to a limited accuracy of our 2D-projected Voronoi algorithm) and a strict interpolation, i.e.  $s = 0$ , for  $\Delta G_{\text{el}}$

Note that instead of (costly) DFT calculations only spline evaluations have to be performed during the numerical optimizations, each yielding a set of optimal parameters  $(\tilde{\varrho}_{\text{iso}}, \tilde{\alpha}, \tilde{\beta})$ . If—for any molecule in the fitting set— $\tilde{\varrho}_{\text{iso}}$  is too far away from the closest node (i.e. the absolute difference to the iso-density value of this node is larger than a given threshold, here e.g.  $0.1 \text{ me \AA}^{-3}$ ), then new nodes are obtained by performing additional DFT calculations for all molecules for  $\varrho_{\text{iso}} = \tilde{\varrho}_{\text{iso}}$ .

5. If any new nodes have been created in the last step, we repeat from step 2 to minimize approximation errors due to spline interpolation.
6. The set of obtained parameters  $(\tilde{\varrho}_{\text{iso}}, \tilde{\alpha}, \tilde{\beta})$  with the lowest corresponding value for  $D$  is the desired set of optimized parameters.

### 6.3 Computational Details

All DFT calculations are performed with FHI-aims employing collinear spin and an “atomic ZORA” scalar-relativistic correction [22]. Calculations are performed for different exchange-correlation functionals—PBE [36], RPBE [90], PBE0 [35], and HSE06 [37, 38]—and numerical settings. In FHI-aims the latter concern the employed numeric atomic orbital basis sets—which are organized in levels, or “tiers”—as well as the density and cutoff-radius of the employed radial integration grids that can be chosen from “light” to “tight” and “really tight” settings. These internal settings and the basis set are described in more detail by Blum et al. [22].

For the dielectric constant of water we use a value of  $\epsilon_b = 78.3553$ . The external potential  $\Phi_Q$  (Eq. (4.1b)) is expanded at the position of all atoms and the reaction field  $\Phi_R$  (Eq. (4.1a)) is expanded at the geometric center of the molecule, i.e. the arithmetic mean of all atoms’ coordinates. Suitable expansion orders for  $\Phi_Q$  and  $\Phi_R$  are derived from a convergence study on the basis of four randomly selected molecules from the test-set summarized in Fig. 4.2. The expansion order for  $\Phi_Q$ ,  $l_{\text{max},Q}$ , is chosen equal to the expansion order  $l_{\text{max},H}$  of the Hartree potential in FHI-aims (Eq. (4.44)), i.e. 4 for light, 6 for tight, and 8 for really tight integration grid settings.  $\Phi_R$  is expanded up to an order of  $l_{\text{max},R} = 8$  which is necessary to observe convergence within 10 % of the final result indicated by the shaded areas in Fig. 4.2. Note, however, that the observed convergence behavior is expected to be heavily influenced by the cavity’s size and shape and a much higher expansion order  $l_{\text{max},R}$  might be necessary for more complex systems than the small organic molecules investigated here.

In the following, two different ways of constructing the iso-density cavity are pursued, namely, either based on the converged electron density of the vacuum calculation or based on the superposition of free atom densities. In both cases, parameters listed in Tab. 5.1 are used, the cavity’s shape is fixed throughout the SCF cycle, and an eightfold over-determination of the MPE equations (cf. Eq. (4.6)) is targeted.

### 6.4 Parametrization Results

The results of the fitting for neutral and cationic components of the Minnesota solvation database are summarized in Tab. 6.1 which is a compilation of our most general parameter sets of Tab. D.1 optimized for neutral and unclustered cationic solutes (test-sets T2 and T3). These parameters should thus be suitable for the study of most neutral and cationic molecular solutes when the

Tab. 6.1: Proposed Parameter Sets for Neutral and Cationic Solutes<sup>a</sup>

| name of parameter set | xc    | $\rho_{\text{iso}}$<br>( $\text{me } \text{\AA}^{-3}$ ) | $\alpha$<br>( $\text{meV } \text{\AA}^{-2}$ ) | $\beta$<br>( $\text{meV } \text{\AA}^{-3}$ ) |
|-----------------------|-------|---|---|--|
|                       | PBE   | 12.5  | 2.80  | -2.23  |
|                       | PBE   | 12.0  | 0.761   | —  |
|                       | RPBE  | 12.2  | 2.65  | -2.11  |
|                       | RPBE  | 11.8  | 0.732   | —  |
|                       | PBE0  | 12.1  | 2.88  | -2.21  |
|                       | PBE0  | 11.6  | 0.848   | —  |
| SPANC                 | HSE06 | <b>12.1</b>   | <b>2.91</b>                                   | <b>-2.25</b>                                 |
| SPANC-surf            | HSE06 | 11.7  | 0.851   | —  |

<sup>a</sup> For each DFT exchange-correlation functional (xc), two parameter sets are given: one with a volume-dependent non-electrostatic contribution (determined by parameter  $\beta$ ), the other without. Reprinted with permission from Ref. [1]. © 2017 American Chemical Society.

“fixed” cavity approach, cf. section 5.3, is used. For reference, full results of the optimization procedure with this type of cavity for all test-sets, different DFT exchange-correlation functionals as well as different basis set and integration grid settings are given in appendix D. A much less extensive parametrization has also been conducted using the “free” cavity approach, i.e. the iso-density cavity is based on the superposition density of free atoms. The corresponding results are summarized in Tab. 6.4.

We observe a convergence of the optimization procedure after  $\leq 12$  DFT calculations for each molecule, nine of which are the starting nodes, indicating the high efficiency of this approach. As an observable we compare the calculated solvation free energy values to the experimental references of the test-set and calculate the difference  $d_M$  of the two for each molecule  $M$ , cf. Eq. (6.1). From these differences we calculate the mean absolute error (MAE),

$$\text{MAE} = \frac{1}{n_{\text{molecules}}} \sum_{M=1}^{n_{\text{molecules}}} |d_M|, \quad (6.4)$$

and the root-mean-square deviation (RMSD),

$$\text{RMSD} = \sqrt{\frac{1}{n_{\text{molecules}}} \sum_{M=1}^{n_{\text{molecules}}} d_M^2}, \quad (6.5)$$

of the whole test-set.

#### 6.4.1 Cavity from Converged Vacuum Density

Since the calculation of the solvation free energy requires a converged *in vacuo* calculation of the solute anyway, the natural choice is to create the cavity as an iso-surface of this converged density. This has been presented before in section 5.3 as the “fixed” cavity approach. With the reaction field depending strongly on the shape of the cavity, the parametrization results presented here should not be mixed with the later ones where the cavity is constructed from a superposition

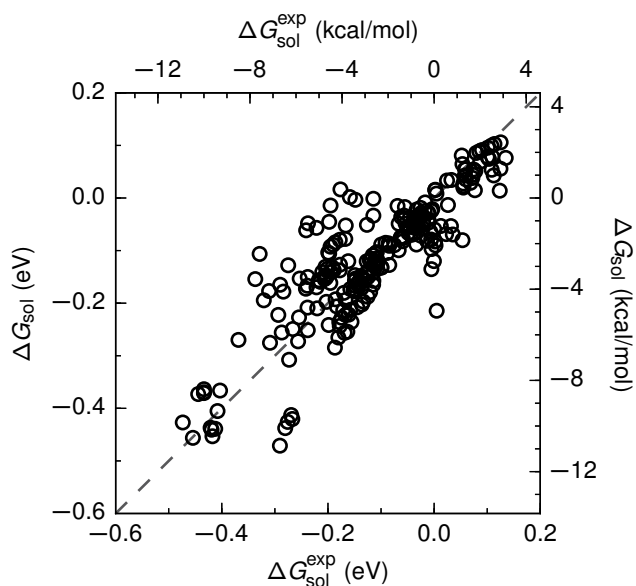


Fig. 6.1: Correlation between calculated ( $\Delta G_{\text{sol}}$ ) and experimentally measured ( $\Delta G_{\text{sol}}^{\text{exp}}$ ) free energies of solvation for the neutral test-set T1 of small organic molecules (see section 6.1). The dashed gray line represents an ideal correlation. Calculations are done using the “HSE06” functional and “tight” integration grid and basis settings (see text) and corresponding MPE parameters for set T1 as listed in Tab. D.1. Reprinted with permission from Ref. [1]. © 2017 American Chemical Society.

of free atom densities, cf. section 6.4.2.

We find that the choice of density functionals and basis sets used in the fitting procedure exerts considerable influence on the solvation parameters, partially due to the fitted solvation model compensating for errors in the functional (cf. Tab. D.1). Aiming for a generally applicable solvation model this is *per se* not ideal as it is often not possible to re-fit parameters for every eventuality. In order to determine the errors of using a parameter set fitted with a given functional to another one we therefore examine such cross-combinations of different parameters and DFT functionals for test set T1 in Tab. 6.3. While this study shows some deviations of the solvation free energies determined with one density functional and solvation parameters determined with another one, these deviations remain relatively small. As a best-practice approach Tab. 6.3 implies that parameters determined with highest computational settings and a high-accuracy hybrid functional perform best even for calculations with lower settings and cheaper GGA functionals.

Further focusing on the test-set T1, Fig. 6.1 illustrates the correlation of calculated and experimentally measured free energies of solvation for this test-set with the fitted solvation parameters for the PBE functional and “tight” integration grid and basis settings. The MAE of this correlation is 46.5 meV and the RMSD amounts to 64.9 meV. All combinations listed under “T1” in Tab. D.1 lead to very similar correlation graphs and error values with MAEs ranging from 47.4 to 50.1 meV and RMSDs from 66.3 to 70.7 meV. We checked the robustness of our fit by using different subsets of the full set T1 as training sets (see section 6.5) all of which result in similar MAE (45.3 to 51.4 meV) and RMSD values (64.9 to 68.4 meV) for the whole test-set.

Using test-set T2 as fit set yields slightly different parameters (cf. Tab. D.1) despite both being

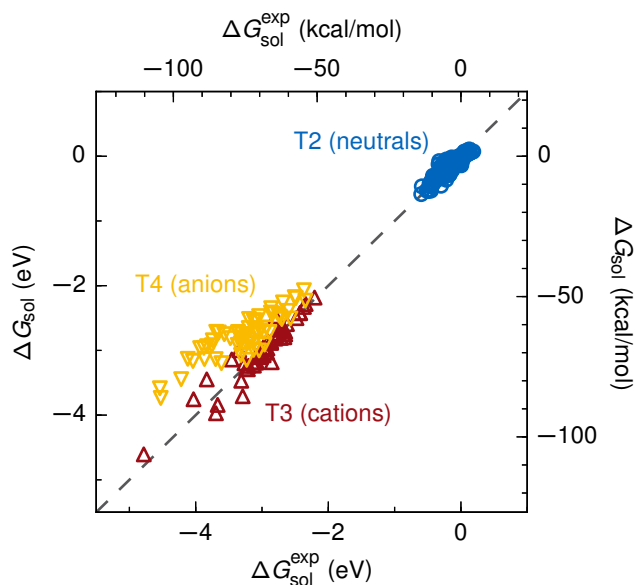


Fig. 6.2: Correlation between calculated ( $\Delta G_{\text{sol}}$ ) and experimentally measured ( $\Delta G_{\text{sol}}^{\text{exp}}$ ) free energies of solvation for the test-sets T2, T3, and T4 (see section 6.1). The dashed gray line represents an ideal correlation. Calculations are done using the “HSE06” functional and “tight” integration grid and basis settings (see text) and corresponding MPE parameters listed in Tab. 6.1 (printed in bold). Reprinted with permission from Ref. [1]. © 2017 American Chemical Society.

Tab. 6.2: Deviations in Hydration Free Energies from Experiment for an Optimized Set of MPE Parameters<sup>a</sup>

| test-set | charge ( $e$ ) | MAE <sup>b</sup> (meV) | RMSD <sup>c</sup> (meV) |
|----------|----------------|------------------------|-------------------------|
| T1       | 0              | 50.8                   | 69.2                    |
| T2       | 0              | 44.4                   | 60.0                    |
| T3       | +1             | 108.6                  | 159.7                   |
| T3c      | +1             | 85.4                   | 118.0                   |
| T4       | -1             | 493.1                  | 560.2                   |
| T4c      | -1             | 419.5                  | 459.5                   |

<sup>a</sup>  $\varrho_{\text{iso}} = 12.1 \text{ me } \text{\AA}^{-3}$ ,  $\alpha = 2.91 \text{ meV } \text{\AA}^{-2}$ ,  $\beta = -2.25 \text{ meV } \text{\AA}^{-3}$  (as listed in Tab. 6.1 for the HSE06 hybrid functional, printed in bold); <sup>b</sup> Mean absolute error; <sup>c</sup> Root-mean-square deviation. Reprinted with permission from Ref. [1]. © 2017 American Chemical Society.

Tab. 6.3: Mean Absolute Errors for Cross-Combination of Parameter Sets for Test Set T1<sup>a,b</sup>

| optimized for → |    | PBE  |      | RPBE | PBE0 | HSE06 |      |
|-----------------|----|------|------|------|------|-------|------|
| used with ↓     |    | l    | t    | rt   | t    | t     |      |
| PBE             | l  | 47.2 | 56.6 | 55.8 | 59.6 | 49.7  | 50.1 |
| PBE             | t  | 49.7 | 46.5 | 46.1 | 47.9 | 47.9  | 47.6 |
| PBE             | rt | 49.0 | 46.8 | 46.3 | 48.2 | 47.6  | 47.4 |
| RPBE            | t  | 52.7 | 46.7 | 46.5 | 47.5 | 50.2  | 49.8 |
| PBE0            | t  | 47.4 | 54.3 | 53.5 | 56.9 | 48.9  | 49.1 |
| HSE06           | t  | 47.4 | 53.7 | 52.9 | 56.2 | 48.7  | 48.9 |

<sup>a</sup> All energies are given in units of meV; <sup>b</sup> l=light, t=tight, and rt=really tight integration grid settings in FHI-aims. Reprinted with permission from Ref. [1]. © 2017 American Chemical Society.

sets of neutral, small, and mostly organic molecules. However, the obtained MAE (41.6 to 43.3 meV) and RMSD values (57.2 to 59.1 meV) are similar and said parameter differences are comparable to the ones observed when fitting on different subsets of T1 (cf. section 6.5).

Including singly charged cations in the fit—i.e. using test-sets T2 and T3—again changes the parameters. In Tab. 6.1 and Tab. D.1, only the MAEs of the whole training set are shown (54.6 to 57.2 meV; RMSDs in the range of 83.6 to 84.5 meV) which are larger than the ones found when using only T2 as training set (see above). Evaluating the deviations for the different subsets separately reveals that the MAE and RMSD values for T1 and T2 are very similar as representatively shown in Tab. 6.2 for the HSE06 hybrid functional and “tight” integration grid and basis settings. Although the major increase in deviations can be attributed to the cationic subset T3 which shows MAE values in the range of 108 to 111 meV and RMSD values from 157 to 162 meV—depending on DFT functional and basis settings—relative errors in the set T3 are typically lower than in T2 as the absolute free energies of hydration is significantly larger for T3 (2 to 5 eV) than for T2 (< 1 eV). The RMSDs on the same cations for the same parameters can even be decreased down to 84.2 to 85.6 meV by selectively clustering certain “problematic” ions with one explicit water molecule as done in test-set T3c. A specific fit including these selectively clustered cations, i.e. fitting to test-set T2+T3c, can only slightly decrease this deviation to 79.4 to 82.4 meV and in general yields very similar parameters and errors as fits to T2+T3.

Adding singly charged anions to the training set—i.e. using test-sets T2, T3, and T4—massively changes the non-electrostatic parameters  $\alpha$  and  $\beta$  and also yields significantly larger MAEs on the whole training set (134 to 152 meV) as well as on the subsets (65.8 to 71.0 meV for T2, 195 to 214 meV for T3, and 397 to 466 meV for T4) as listed in Tab. D.2. Similar observations are made for the RMSD values. This is consistent with the findings of previous work [80] employing an iso-density approach and the same non-electrostatic model where the authors conclude to propose two different parameter sets for neutral and cationic and for anionic molecules. Very recent investigations [69] reach a better description of ions by using soft-spheres around the atoms of a molecule as cavity instead of an iso-density cavity. Nonetheless, the authors still propose two different parameter sets indicating limitations of the very simple non-electrostatic model shared in this work to describe both types of ions simultaneously.

Note that fitting the model to test-set T4 alone is, of course, possible and yields acceptable accuracy compared to other implicit solvation models [48, 69, 91] with MAEs in the range of 161 to 178 meV. However, the obtained parameter sets (see Tab. D.2) differ strongly for different

functionals, basis sets and integration grid settings. This can partially be remedied by fitting again to a test-set of selectively clustered anions, T4c, yielding a more uniform set of parameters with respect to computational settings and lower MAEs (128 to 141 meV). All of the anionic fits lead to much larger iso-density values and mostly also to different signs in the non-electrostatic parameters compared to the neutral and cationic fits and such optimized parameters produce huge errors when applied to test-sets T1, T2, T3, or T3c.

Finding a general description of neutral, cationic, and anionic molecules using the same set of parameters could not be achieved in this work using the “fixed” cavity approach. Nevertheless can already a simultaneous description of neutral and cationic solutes be of great interest, e.g. in the fields of photo-electrocatalysis [92], for which common parameters can, in fact, be found. As the most general set of parameters we thus propose the settings for the high-accuracy HSE06 functional fitted to test-sets T2 and T3 (highlighted in bold in Tab. 6.1). For easier reference we term these the solvation parameters for neutrals and cations (SPANC).

Figure 6.2 shows the correlation of experimental versus calculated solvation free energies using the MPE-SPANC for test-sets T2, T3 and T4, illustrating again the good model performance for neutrals and cations.

The optimized MPE-SPANC for non-electrostatics,  $\alpha = 2.91 \text{ meV } \text{\AA}^{-2}$  and  $\beta = -2.25 \text{ meV } \text{\AA}^{-3}$ , agree well with the findings of previous work [21] (0.69 to  $3.12 \text{ meV } \text{\AA}^{-2}$  and  $-0.50$  to  $-2.18 \text{ meV } \text{\AA}^{-3}$  for the two-parameter model) which provided the model for non-electrostatic contributions employed in this work. The iso-density value  $\varrho_{\text{iso}}$  is more difficult to compare directly since Andreussi et al. [21] use a smooth dielectric function with an onset  $\rho^{\text{min}}$  and an offset parameter  $\rho^{\text{max}}$ . The optimized value of  $\varrho_{\text{iso}} = 12.1 \text{ me } \text{\AA}^{-3}$  lies between those two parameters or is at least close to the offset parameter  $\rho^{\text{max}}$  of approximately 10 to  $34 \text{ me } \text{\AA}^{-3}$ . Another previous study [79] suggests an optimal iso-density value of approximately  $3.4$  to  $13 \text{ me } \text{\AA}^{-3}$  which also compares well with our result.

Finally, inspired by ideas put forward by Fiscaro et al. [69] and as also previously employed by Andreussi et al. [21] we determined optimized parameter sets with the volume-dependent non-electrostatic term constrained to zero, i.e.  $\beta = 0$ , which is included in Tabs. D.1 and D.2. Compared to the three-parameter model ( $\varrho_{\text{iso}}, \alpha, \beta$ ), this two-parameter model ( $\varrho_{\text{iso}}, \alpha$ ) obviously shows less accurate results with MAEs increased by roughly 20 % for neutral solutes (test-sets T1 and T2), 10 % for neutral and cationic solutes (T2+T3 and T2+T3c), and less than 5 % for anionic solutes (T4 and T4c). Eliminating an explicit dependence on the cavity volume, however, serves as a crucial stepping stone for future calculations of solvation effects on extended surfaces of solids. In analogy to MPE-SPANC, we term the parameter set for the high-accuracy HSE06 functional fitted to test-sets T2 and T3 as listed in Tab. 6.1 MPE-SPANC-surf.

#### 6.4.2 Cavity from Superposition of Free Atom Densities

As mentioned before in section 5.3, the (converged) vacuum density is not the only choice available. Especially the superposition of free atoms exhibits some nice advantages:

- The density is at least as easy to evaluate in FHI-aims.
- All information needed for the cavity construction is available without memory of previous calculations such as e.g. the solute *in vacuo*.
- The cavity shape does not depend on the charge state of the molecule because the superposition is created from neutral atoms.

The reason why the last point is possibly advantageous deserves some explanation. Since the monopole moment is dominating for a charged system we can, for the moment, neglect all poles of higher order. Furthermore, we assume that the cavity is spherical such that we can use the simple Born model (cf. section 3.3.1) to analyze the situation. The Born model predicts the same electrostatic free energy of solvation for two oppositely charged ions when the same cavity radius is used for both. In case of an iso-density based cavity, however, the radius depends on the electron density distribution which is much diffuser in case of the anion than for the neutral species or even a cation. For the same iso-density value, the cavity of the anion is thus often considerably larger than the one of the cation. With the electrostatic solvation effect being inversely proportional to the cavity's size, the larger cavity leads to a less negative electrostatic solvation free energy. In order to compensate for this and obtain a similarly large effect for anions, the fitting procedure leads to an iso-density value that is by far larger than for cations (or neutral solutes)—as observed in Tab. D.2.

It should be noted here that the previously discussed charge-sign symmetry of the (electrostatic) solvation free energy—which is found for most continuum solvation models—is known to be unphysical and several correction schemes have been proposed [93–95]. However, this is an entirely different effect and probably insignificant compared to the large overestimation of the cavity size of anions with an inappropriate parameter set. Facing this problem, the superposition of neutral free atom densities constitutes a simple yet effective alternative because the cavity is then defined solely by the geometry of the solute (including the atoms' species) and not by its charge state. This effect can be studied by comparing results of both approaches (“fixed” *versus* “free” cavity) with correspondingly optimized parameters but otherwise identical computational settings. As an example, Fig. 6.3 shows this comparison for the PBE functional with “tight” integration grid and basis settings where—for both iso-density cavity approaches depicted in Figs. 6.3a and 6.3b, respectively—T2+T3 has been used as fitting set to determine the optimized parameter sets. The one for the “fixed” cavity is listed in Tab. 6.1 whereas the corresponding parameter set for the “fixed” cavity is tabulated in Tab. 6.4. Comparing Fig. 6.3a to Fig. 6.3b, one immediately can see that the correlation both for unclustered (T4) and selectively clustered anions (T4c) is significantly better for the “free” cavity approach. This can be inspected in more detail on the basis of the deviations tabulated in Tab. 6.5 which reveals a decrease of the MAE from 493.1 meV to 305.1 meV for test set T4 and from 419.5 meV to 262.5 meV for T4c. A similar trend holds for the RMSD values.

Furthermore, fitting to the big set T2+T3+T4 which includes cationic and anionic solutes also yields reasonable results in the “free” cavity approach in contrast to the “fixed” one, cf. Tab. D.2. In this case, the errors for cationic solutes stay relatively constant while the error on anionic solutes can be lowered at the cost of sacrificing accuracy in the description of neutrals where both the MAE and RMSD increase by approximately 40%. Bearing in mind that the total solvation free energy of neutral solutes is typically much smaller in magnitude than for charged species, this trade-off is most probably not desired. In summary, the “free” cavity approach is also not fully able to treat all kinds of solutes—neutral, cationic and anionic—on the same footing with the same accuracy. Nonetheless, it is still much better in this aspect than the “fixed” cavity approach based on the converged vacuum density and thus certainly deserves more attention in future works. Especially the fact, that the optimized iso-density value is very similar to the T2, T2+T3, and the T2+T3c fitting seems promising since this could mean that changing the (anyhow not very physical) non-electrostatic contribution might be enough to reach a simultaneous description.



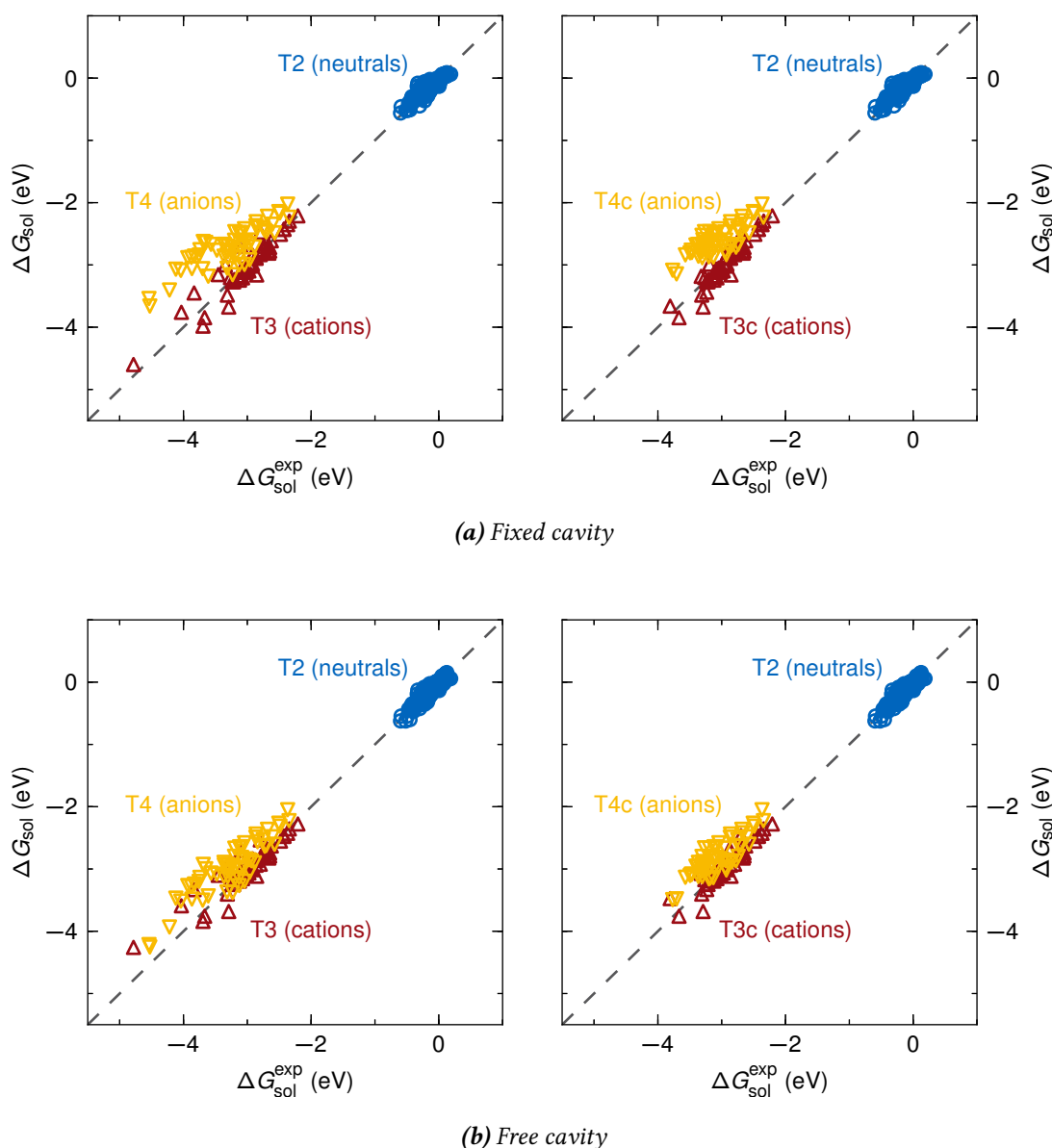


Fig. 6.3: Correlation between calculated ( $\Delta G_{\text{sol}}$ ) and experimentally measured ( $\Delta G_{\text{sol}}^{\text{exp}}$ ) free energies of solvation for different molecular test sets defined in section 6.1. For reference, results calculated with the “PBE” functional, “tight” integration grid and basis settings (see text), and corresponding MPE parameters optimized for neutral and cationic solutes (T2+T3) as listed in Tab. 6.1 are shown in the top, **(a)**, where the converged vacuum density is used to construct the iso-density cavity. In the bottom, **(b)**, the same computational settings are used except for the iso-density cavity—which is created from the superposition density of free atoms—and correspondingly optimized MPE parameters. In all panels, the dashed gray line represents an ideal correlation.

Tab. 6.4: Parameter Optimization Results For the “Free” Cavity Approach<sup>a</sup>

| $\text{xc}^b$            | set. <sup>c</sup> | $\rho_{\text{iso}}$<br>( $\text{me \AA}^{-3}$ ) | $\alpha$<br>( $\text{meV \AA}^{-2}$ ) | $\beta$<br>( $\text{meV \AA}^{-3}$ ) | MAE <sup>d</sup><br>(meV) |
|--------------------------|-------------------|---|---------------------------------------|--------------------------------------|---------------------------|
| T2 (274 solutes)         |                   |   |                                       |                                      |                           |
| PBE                      | t                 | 32.6  | 5.78                                  | -5.13                                | 41.6                      |
| PBE                      | t                 | 25.9  | 0.986                                 | 0                                    | 51.9                      |
| T2+T3 (326 solutes)      |                   |   |                                       |                                      |                           |
| PBE                      | t                 | 37.9  | 6.06                                  | -5.08                                | 54.5                      |
| PBE                      | t                 | 36.5  | 1.77                                  | 0                                    | 64.2                      |
| T2+T3c (326 solutes)     |                   |   |                                       |                                      |                           |
| PBE                      | t                 | 36.1  | 5.73                                  | -4.84                                | 49.1                      |
| PBE                      | t                 | 34.7  | 1.61                                  | 0                                    | 58.9                      |
| T2+T3+T4 (386 solutes)   |                   |   |                                       |                                      |                           |
| PBE                      | t                 | 36.3  | 1.75                                  | -0.339                               | 101.1                     |
| PBE                      | t                 | 36.2  | 1.47                                  | 0                                    | 101.8                     |
| T2+T3c+T4c (386 solutes) |                   |   |                                       |                                      |                           |
| PBE                      | t                 | 34.1  | 1.97                                  | -0.805                               | 88.1                      |
| PBE                      | t                 | 34.1  | 1.30                                  | 0                                    | 89.4                      |
| T4 (60 solutes)          |                   |   |                                       |                                      |                           |
| PBE                      | t                 | 94.2  | 4.02                                  | 1.28                                 | 154.0                     |
| PBE                      | t                 | 94.1  | 4.82                                  | 0                                    | 154.2                     |
| T4c (60 solutes)         |                   |   |                                       |                                      |                           |
| PBE                      | t                 | 68.1  | 10.7                                  | -12.5                                | 126.6                     |
| PBE                      | t                 | 49.4  | 0.448                                 | 0                                    | 129.2                     |

<sup>a</sup> For all computational settings, two parameter sets are given: one with a volume-dependent non-electrostatic contribution (determined by parameter  $\beta$ ), the other without; <sup>b</sup> DFT exchange-correlation functional; <sup>c</sup> FHI aims basis-set and integration grid settings with abbreviations l=light, t=tight, and rt=really tight; <sup>d</sup> Mean absolute error.

Tab. 6.5: Comparison of Deviations in Hydration Free Energies from Experiment for Sets of MPE Parameters Optimized for Two Different Test Sets in Combination with Two Different Isodensity Cavity Approaches

| T2+T3    |                |                           |                         |                          |                         |
|----------|----------------|---------------------------|-------------------------|--------------------------|-------------------------|
| test-set | charge ( $e$ ) | fixed cavity <sup>a</sup> |                         | free cavity <sup>b</sup> |                         |
|          |                | MAE <sup>c</sup> (meV)    | RMSD <sup>d</sup> (meV) | MAE <sup>c</sup> (meV)   | RMSD <sup>d</sup> (meV) |
| T2       | 0              | 44.4                      | 60.0                    | 43.2                     | 55.7                    |
| T3       | +1             | 108.6                     | 159.7                   | 113.8                    | 176.8                   |
| T3c      | +1             | 85.4                      | 118.0                   | 87.7                     | 123.9                   |
| T4       | -1             | 493.1                     | 560.2                   | 305.1                    | 359.4                   |
| T4c      | -1             | 419.5                     | 459.5                   | 262.5                    | 304.8                   |

| T2+T3+T4 |                |                           |                         |                          |                         |
|----------|----------------|---------------------------|-------------------------|--------------------------|-------------------------|
| test-set | charge ( $e$ ) | fixed cavity <sup>a</sup> |                         | free cavity <sup>b</sup> |                         |
|          |                | MAE <sup>c</sup> (meV)    | RMSD <sup>d</sup> (meV) | MAE <sup>c</sup> (meV)   | RMSD <sup>d</sup> (meV) |
| T2       | 0              | 69.6                      | 82.0                    | 61.2                     | 76.9                    |
| T3       | +1             | 209.7                     | 234.8                   | 119.1                    | 172.8                   |
| T3c      | +1             | 194.7                     | 225.9                   | 90.8                     | 120.2                   |
| T4       | -1             | 454.7                     | 528.6                   | 267.8                    | 320.7                   |
| T4c      | -1             | 378.6                     | 423.5                   | 224.6                    | 262.0                   |

<sup>a</sup>  $\rho_{\text{iso}}$ ,  $\alpha$ , and  $\beta$  as listed in Tab. 6.1 for the PBE functional; <sup>b</sup>  $\rho_{\text{iso}}$ ,  $\alpha$ , and  $\beta$  as listed in Tab. 6.4; <sup>c</sup> Mean absolute error; <sup>d</sup> Root-mean-square deviation.

## 6.5 Complementary Statistical Analysis

In order to test the robustness of the parametrization procedure (see section 6.2), we divide the whole test-set T1 of 240 small organic molecules in different ways, each time into a training set used to fit the MPE parameters ( $\rho_{\text{iso}}$ ,  $\alpha$ , and  $\beta$ ) and a validation set. The training sets thereby consist of 80, 120, or 160 molecules randomly drawn from the full test-set in 16 different ways each. For every individual training set the parameters are optimized as described above using the same computational settings. Representatively for all combinations of functional and integration grid/basis settings investigated above, we only consider “PBE tight” here. The results of all optimizations are illustrated in Fig. 6.4. Although the optimized parameter values can vary significantly—especially when only one third of the test-set is used as training set—the MAE and RMSD values on the total test-set vary only slightly: MAEs in the range of 45.3 to 51.4 meV for 80, 45.7 to 49.7 meV for 120, and 45.8 to 47.4 meV for 160 molecules in the training set; RMSDs in the range of 64.9 to 68.4 meV for 80, 64.9 to 66.5 meV for 120, and 64.9 to 65.3 meV for 160 molecules in the training set. Thus, a strong correlation seems to exist between all three parameters which has previously only been observed for the non-electrostatic parameters [21]. Due to this correlation, a wide range of parameter combinations can lead to similar accuracies, which means that any one of these combinations is comparatively robust. On the other hand, the results of Fig. 6.4 also show that no further improvement of the accuracy seems possible without modification of the electrostatic or non-electrostatic model, or both.

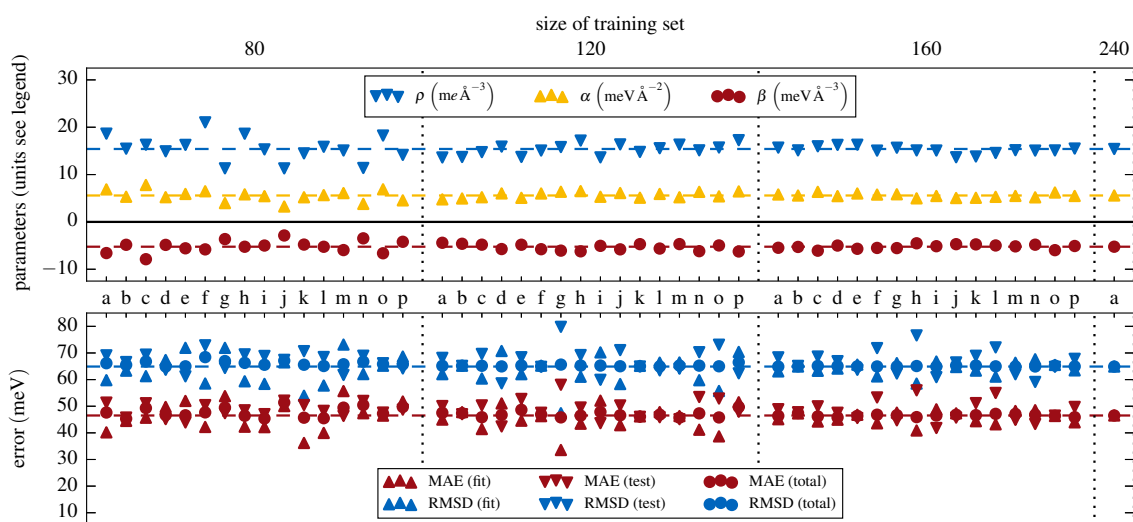


Fig. 6.4: From the full test-set T1 with 240 molecules, subsets consisting of 80, 120, and 160 molecules (top axis) are randomly drawn, 16 times each (labeled a-p on the center axis). Every set is individually used as training set in a parameter fitting procedure as described in section 6.2 with the same computational settings as previously used for the PBE functional and “tight” integration grid and basis settings (cf. section 6.3). The upper panel depicts the resulting parameter sets ( $\rho_{\text{iso}}$ ,  $\alpha$ ,  $\beta$ ). The lower panel shows the mean absolute error (MAE, in red) and the root-mean-square deviation (RMSD, in blue) of the calculated free energies of solvation with respect to the experimental values considering the full test-set (“total”, as circles), only the training set (“fit”, as triangles up), or only the validation set (“test”, as triangles down) which consists of all molecules of the full test-set that are not in the corresponding training set. Reprinted with permission from Ref. [1]. © 2017 American Chemical Society.

## 6.6 Timings

Having demonstrated the accuracy of our MPE scheme for a representative test-set, we now want to turn to the computational cost of the method. In summary, the overhead compared to a pure *in vacuo* calculation is due to cavity generation, solution of the SLE, and the construction of the reaction field on the integration grid of the DFT program FHI-aims. In Fig. 6.5, this relative overhead is shown for both the PBE and the HSE06 hybrid functional. Note that for both functionals, the relative overhead is only a fraction of the total cost of the respective vacuum calculation (approximately 10 to 20 % for PBE and 2 % for HSE06). While for the relatively cheap PBE functional the share of MPE on the total computing time with the number of atoms in the respective molecules stays relatively constant, for the significantly more accurate hybrid functional the relative computational cost even decreases with system size. The latter is due to a more favorable scaling of MPE with respect to system size in the size range of our test-set compared to the exact exchange part of the hybrid functional. It should be noted here that while usually the number of electrons or, more precisely, basis functions is the determining parameter for such scaling studies, the MPE method is very insensitive to this number. Instead, simply the number of nuclei is most significant as it directly influences the discretization level, cf. section 4.1, of the MPE method which is the key quantity that determines the required effort to create the cavity and solve the MPE equations. Furthermore, the size of the atom centered integration grid which is directly related to the number of reaction field evaluations also depends on the number of nuclei.

Overall, this implies that our MPE implementation adds only little to negligible cost to DFT calculations with production settings.

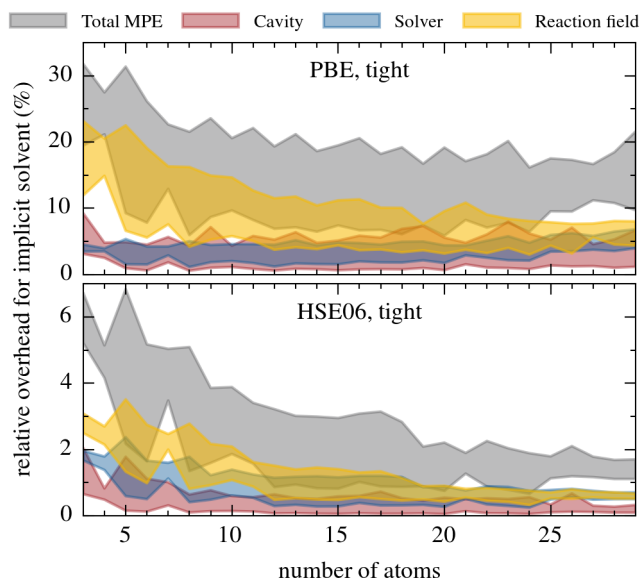


Fig. 6.5: Relative overhead cost of the MPE method for the PBE GGA (upper panel) and the HSE06 hybrid (lower panel) functional at default tight settings with respect to the underlying SCF cycle. Shown are the ranges of costs for the molecular test-set versus number of atoms from cheapest (lower edges) to computationally most costly (top edges). This accounts for differences in molecular complexity (e.g. number of electrons) at each respective number of atoms per molecule. For improved statistics, all DFT calculations performed during the fitting procedure in chapter 6 are considered which includes calculations with different iso-density values for each molecule. Along with the total overhead cost (“Total MPE”, depicted in gray), its three major contributions directly related to the determination of the sampling points on the implicit solvent cavity (“Cavity”, in red), the solution of the MPE equations (“Solver”, in blue), and the evaluation of the total solvent potential, i.e. reaction field, on the integration grid (“Reaction field”, in yellow) are shown. Reprinted with permission from Ref. [1]. © 2017 American Chemical Society.



## 7 Outlook: Extension to Two Dielectrics

---

Especially in the field of electrochemistry, reactions at the interface of two liquids, or of a liquid with air, recently experienced an increase in attention with the observation of high catalytic activities for the hydrogen evolution reaction at an interface of two immiscible electrolyte solutions [31, 32]. In this outlook, we will thus propose extensions and modifications to make the above presented MPE model suitable to treat similar systems.

The introduction of an interface, e.g. between two solvents, in a continuum solvation model is equivalent to lifting the assumption that the embedding dielectric is homogeneous—which has been introduced in section 3.1.2 as a central assumption in the derivation of the implicit solvation model. However, when certain approximations about the structure of such an interface can be made, the model is still applicable with only minor changes.

### 7.1 Definition of the Planar Interface

For the moment, we will put aside the concept of a solvation cavity and focus only on the interface between the two solvents which we assume to be perfectly planar. For the sake of simplicity and following common practice in slab calculation setups, we will align the interface with the  $xy$  plane such that the  $z$  coordinate axis is perpendicular to it. Due to the symmetry of the problem it is advantageous to introduce a cylindrical coordinate system with coordinates  $(\rho, \zeta)$  as used in appendix B.1 where the  $\zeta$  axis coincides with the  $z$  axis of the Cartesian coordinate system. Both axes intersect with the interface plane at a  $\zeta$ -value of  $\zeta_0$ . The next assumption is that the dielectric permittivity function, in analogy to Eq. (3.20), is constant within the two media and exhibits a step-like transition across the interface. In the cylindrical coordinate system this reads

$$\varepsilon_{\text{interface}}(\rho, \zeta) = \varepsilon_{b,(-)} + (\varepsilon_{b,(+)} - \varepsilon_{b,(-)}) \Theta(\zeta - \zeta_0), \quad (7.1)$$

where  $\varepsilon_{b,(-)}$  and  $\varepsilon_{b,(+)}$  are the bulk permittivities of the lower and upper dielectric medium, respectively, and  $\Theta$  is the Heaviside step function. In order to generalize this expression later on, we introduce the interface function  $\mathcal{L}$ ,

$$\mathcal{L}(\rho, \zeta) = \zeta - \zeta_0. \quad (7.2)$$

Similar to the cavity function  $\mathcal{C}$ , cf. Eq. (3.20), this function is positive in one dielectric region and negative in the other one. Assuming no specific form of this function, we can write

$$\varepsilon_{\text{interface}}(\rho, \zeta) = \varepsilon_{b,(-)} + (\varepsilon_{b,(+)} - \varepsilon_{b,(-)}) \Theta[\mathcal{L}(\rho, \zeta)]. \quad (7.3)$$

A point  $\mathbf{s}$  on the interface between the dielectrics is then simply characterized by  $\mathcal{L}(\mathbf{s}) = 0$ .



### 7.1.1 Image Charge Ansatz for a Single Monopole

For the simple example of a monopole, the electrostatic potential can easily be found analytically using the image charge method [41]. Assuming that  $\zeta_0 = 0$  and that the charge  $q$  is situated at the coordinates  $\mathbf{r}_q = (0, \zeta_q)$  in the cylindrical coordinate system, the resulting electrostatic potential can be described with a fictitious screening charge  $q_s$  at the same position, and a fictitious image charge  $q_i$  located at the point  $\mathbf{r}_o = (0, -\zeta_q)$ , i.e. at the mirrored position of the actual charge,

$$\Phi(\rho, \zeta) = \frac{q}{\sqrt{\rho^2 + (\zeta - \zeta_q)^2}} \begin{cases} \varepsilon_{b,(+)}^{-1} \\ \varepsilon_{b,(-)}^{-1} \end{cases} + \begin{cases} \frac{q_i}{\varepsilon_{b,(+)} \sqrt{\rho^2 + (\zeta + \zeta_q)^2}}, & \zeta > \zeta_0 = 0 \\ \frac{q_s}{\varepsilon_{b,(-)} \sqrt{\rho^2 + (\zeta - \zeta_q)^2}}, & \zeta < \zeta_0 = 0 \end{cases}. \quad (7.4)$$

The unknown charges  $q_i$  and  $q_s$  can be found by evaluation of the electrostatic boundary conditions at the interface, i.e.

$$\lim_{\zeta \rightarrow 0^+} \Phi(\rho, \zeta) = \lim_{\zeta \rightarrow 0^-} \Phi(\rho, \zeta), \quad (7.5a)$$

and

$$\lim_{\zeta \rightarrow 0^+} \left( \varepsilon_{\text{interface}}(\rho, \zeta) \frac{\partial \Phi}{\partial \zeta} \Big|_{\zeta} \right) = \lim_{\zeta \rightarrow 0^-} \left( \varepsilon_{\text{interface}}(\rho, \zeta) \frac{\partial \Phi}{\partial \zeta} \Big|_{\zeta} \right). \quad (7.5b)$$

Solving these equations yields

$$q_i = q \frac{\varepsilon_{b,(+)} - \varepsilon_{b,(-)}}{\varepsilon_{b,(+)} + \varepsilon_{b,(-)}}, \quad (7.6a)$$

and

$$q_s = q \frac{\varepsilon_{b,(-)} - \varepsilon_{b,(+)}}{\varepsilon_{b,(+)} + \varepsilon_{b,(-)}}, \quad (7.6b)$$

with which we have completely determined the electrostatic potential.

### 7.1.2 Return to Multipole Expansion

It is important to note that the boundary conditions in Eqs. (7.5a) and (7.5b) are completely equivalent to the previously encountered ones in Eqs. (3.22a) and (3.22b)—except that both sides of the interface can now have a dielectric permittivity different from 1. Furthermore, the ansatz, Eq. (7.4), is already written in a very similar form as Eq. (3.40) which suggests that the MPE model as derived above should almost directly be applicable to the present problem. To facilitate the analogy, we can rewrite Eq. (7.4) using a similar notation,

$$\Phi(\rho, \zeta) = \Phi_{\text{H}} \begin{cases} \varepsilon_{b,(+)}^{-1} \\ \varepsilon_{b,(-)}^{-1} \end{cases} + \begin{cases} \Phi_{\text{O}}, & \zeta > 0 \\ \Phi_{\text{Q}}, & \zeta < 0 \end{cases}, \quad (7.7)$$

where

$$\Phi_H(\mathbf{r}) = \frac{q}{\|\mathbf{r} - \mathbf{r}_q\|_2}. \quad (7.8)$$

Extending the above potential ansatz for  $\Phi_O$  and  $\Phi_Q$ , both are now represented using multipole expansions, cf. Eq. (4.1b), around the charge at  $\mathbf{r}_q$ ,

$$\Phi_Q(\mathbf{r}) = \sum_{l=0}^{l_{\max,Q}} \sum_{m=-l}^l Q^{(l,m)} \mathcal{I}_m^l(\mathbf{r} - \mathbf{r}_q), \quad (7.9a)$$

and the fictitious mirror charge at  $\mathbf{r}_o$ ,

$$\Phi_O(\mathbf{r}) = \sum_{l=0}^{l_{\max,O}} \sum_{m=-l}^l O^{(l,m)} \mathcal{I}_m^l(\mathbf{r} - \mathbf{r}_o). \quad (7.9b)$$

Equivalently to Eq. (4.3), the two branches of Eq. (7.7) can be evaluated at any point  $\mathbf{s}$  on the interface where they couple *via* the following equations,

$$\begin{aligned} \Phi_O(\mathbf{s}) - \Phi_Q(\mathbf{s}) &= (\varepsilon_{b,(+)}^{-1} - \varepsilon_{b,(-)}^{-1}) \Phi_H(\mathbf{s}), \\ \mathbf{n}_s \cdot \varepsilon_{b,(-)} \nabla \Phi_O(\mathbf{s}) - \mathbf{n}_s \cdot \varepsilon_{b,(+)} \nabla \Phi_Q(\mathbf{s}) &= 0 \end{aligned} \quad (7.10)$$

where  $\mathbf{n}_s$  is the normal vector on the interface—here, the unit vector in  $\zeta$ -direction. For the discretization of the interface in Cartesian coordinates as consistently used within the MPE model, a logarithmic polar grid is created which consists of  $n_{\text{shells}}$  circular shells of exponentially increasing radius with  $n_{\text{angular}}$  points each, i.e.

$$\mathbf{s}_{ik} = R_{\min} \cdot \left( \frac{R_{\max}}{R_{\min}} \right)^{\frac{i-1}{n_{\text{shells}}-1}} \cdot \begin{pmatrix} \cos\left(\frac{k-1}{n_{\text{angular}}} 2\pi\right) \\ \sin\left(\frac{k-1}{n_{\text{angular}}} 2\pi\right) \\ 0 \end{pmatrix}, \quad (7.11)$$

$$i \in \{1, 2, \dots, n_{\text{shells}}\}, \quad k \in \{1, 2, \dots, n_{\text{angular}}\},$$

where  $R_{\min}$  is the radius of the smallest circular shell and  $R_{\max}$  the one of the largest. For the sake of simplicity, these points are numbered consecutively from 1 to  $n_{\text{shells}} \times n_{\text{angular}}$ .

Tab. 7.1: Comparison of MPE Reaction Field Coefficients to Analytic Solution for a Monopole at the Interface of Two Dielectrics<sup>a</sup>

| $\epsilon_{b,(+)}$ | $\epsilon_{b,(-)}$ | $\epsilon_{b,(+)}^{-1}q_i$   | $\epsilon_{b,(+)}^{-1}q_s$  | $O^{(0,0)}$                  | $Q^{(0,0)}$                 |
|--------------------|--------------------|------------------------------|-----------------------------|------------------------------|-----------------------------|
| 1                  | 27                 | $-9.285\,714 \times 10^{-1}$ | $3.439\,153 \times 10^{-2}$ | $-9.285\,714 \times 10^{-1}$ | $3.439\,153 \times 10^{-2}$ |
| 1                  | 243                | $-9.918\,033 \times 10^{-1}$ | $4.081\,495 \times 10^{-3}$ | $-9.918\,033 \times 10^{-1}$ | $4.081\,495 \times 10^{-3}$ |
| 9                  | 243                | $-1.031\,746 \times 10^{-1}$ | $3.821\,282 \times 10^{-3}$ | $-1.031\,746 \times 10^{-1}$ | $3.821\,282 \times 10^{-3}$ |

<sup>a</sup> In the test setup, a charge is placed  $0.5 a_0$  in front of a planar interface between two dielectrics with a permittivity of  $\epsilon_{b,(+)}$  and  $\epsilon_{b,(-)}$ , respectively. For more details, see text. Agreement between the results is found up to numerical precision ( $1 \times 10^{-14}$ ).

The resulting system of equations is transformed into the linear algebra form of Eq. (4.9),

$$\begin{pmatrix}
 \mathcal{I}_0^0(\mathbf{s}_1 - \mathbf{r}_o) & \mathbf{n}_{\mathbf{s}_1} \cdot \epsilon_{b,(-)} \nabla \mathcal{I}_0^0(\mathbf{s}_1 - \mathbf{r}_o) & \dots \\
 \mathcal{I}_{-1}^1(\mathbf{s}_1 - \mathbf{r}_o) & \mathbf{n}_{\mathbf{s}_1} \cdot \epsilon_{b,(-)} \nabla \mathcal{I}_{-1}^1(\mathbf{s}_1 - \mathbf{r}_o) & \dots \\
 \mathcal{I}_0^1(\mathbf{s}_1 - \mathbf{r}_o) & \mathbf{n}_{\mathbf{s}_1} \cdot \epsilon_{b,(-)} \nabla \mathcal{I}_0^1(\mathbf{s}_1 - \mathbf{r}_o) & \dots \\
 \vdots & \vdots & \ddots \\
 -\mathcal{I}_0^0(\mathbf{s}_1 - \mathbf{r}_q) & -\mathbf{n}_{\mathbf{s}_1} \cdot \epsilon_{b,(+)} \nabla \mathcal{I}_0^0(\mathbf{s}_1 - \mathbf{r}_q) & \dots \\
 -\mathcal{I}_{-1}^1(\mathbf{s}_1 - \mathbf{r}_q) & -\mathbf{n}_{\mathbf{s}_1} \cdot \epsilon_{b,(+)} \nabla \mathcal{I}_{-1}^1(\mathbf{s}_1 - \mathbf{r}_q) & \dots \\
 \vdots & \vdots & \ddots
 \end{pmatrix}^T \cdot \begin{pmatrix}
 O^{(0,0)} \\
 O^{(1,-1)} \\
 O^{(1,0)} \\
 \vdots \\
 Q^{(0,0)} \\
 Q^{(1,-1)} \\
 \vdots
 \end{pmatrix} = \begin{pmatrix}
 (\epsilon_{b,(+)}^{-1} - \epsilon_{b,(-)}^{-1})\Phi_H(\mathbf{s}_1) & 0 & \dots
 \end{pmatrix}^T, \quad (7.12)$$

and can be solved using the same methods as previously introduced for the MPE method. In order to test this approach, we compare the obtained coefficients of the MPE model,  $O^{(l,m)}$  and  $Q^{(l,m)}$ , to the previously found analytical solution for the point charge at the dielectric interface. Although all expansion terms up to a quadrupolar moment ( $l_{\max,O} = l_{\max,Q} = 2$ ) have been considered, only the coefficients for the monopole terms are listed in Tab. 7.1 because all other coefficients are correctly determined to be (numerically) zero. For the MPE solution, a log-polar grid of 51 circles ( $R_{\min} = 0.1 a_0$ ,  $R_{\max} = 100.0 a_0$ ) with 50 points each is spanned on the interface, cf. Eq. (7.11), centered around the projection of the charge's position on the interface plane.

### 7.1.3 Comparison to FEM for Higher Order Multipoles

In principle, analytical expressions can also be found for point dipoles (or higher order multipoles) at the planar dielectric interface. The solutions, however, can become tedious and by the time a solvation cavity is reintroduced, it will be unavoidable to use another numerical method as reference. For this purpose, the previously employed FEM approach using the KARDOS solver has also been extended to include the planar interface between two dielectrics, cf. appendix B.2.2. The excellent agreement of both methods is illustrated in Fig. 7.1. Thereby, the same log-polar grid of points on the interface has been used for the MPE model as for the monopole setup before.

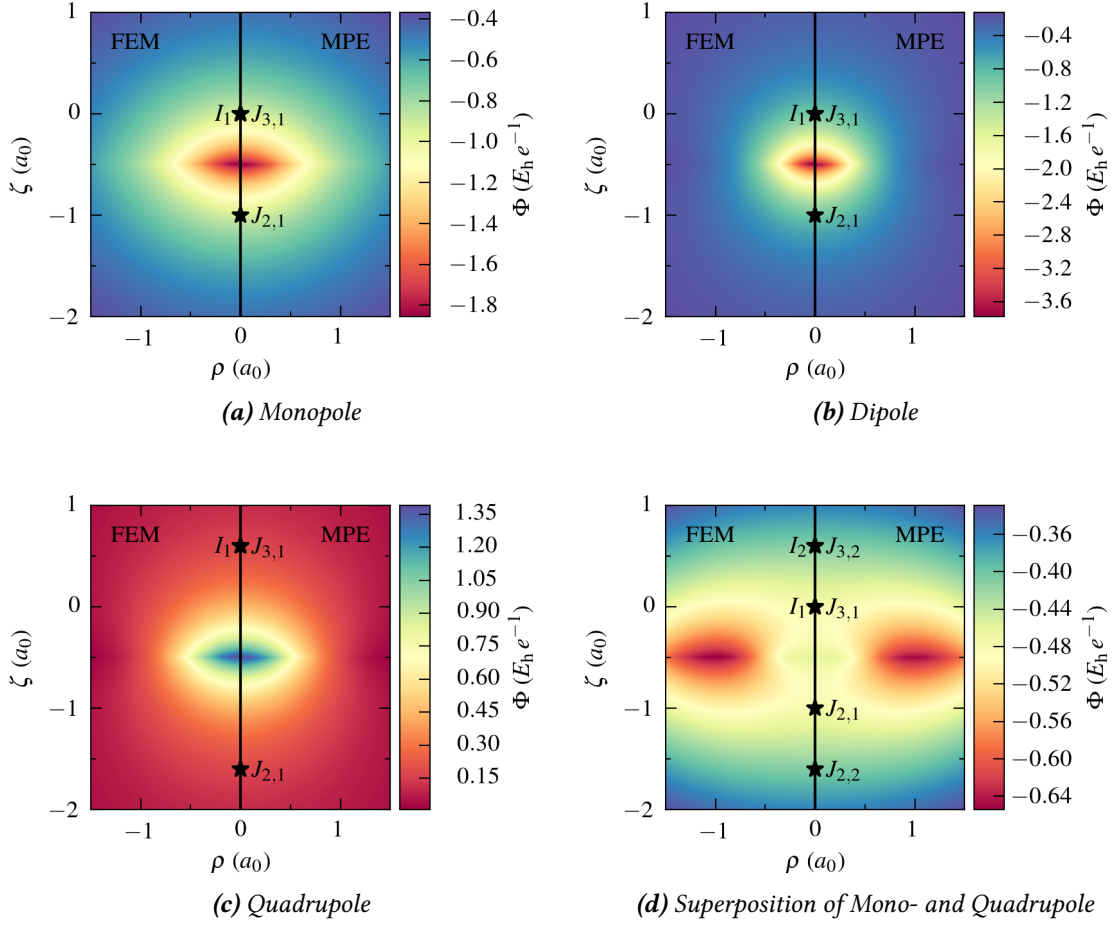


Fig. 7.1: Comparison of the reaction field calculated by the FEM and the MPE method for one or two point-multipoles at a planar interface ( $\zeta_0 = -0.5 a_0$ ) between vacuum ( $\epsilon_{b,(+)} = 1$  for  $\zeta > \zeta_0$ ) and a dielectric medium ( $\epsilon_{b,(-)} = 27.542$  for  $\zeta < \zeta_0$ ).

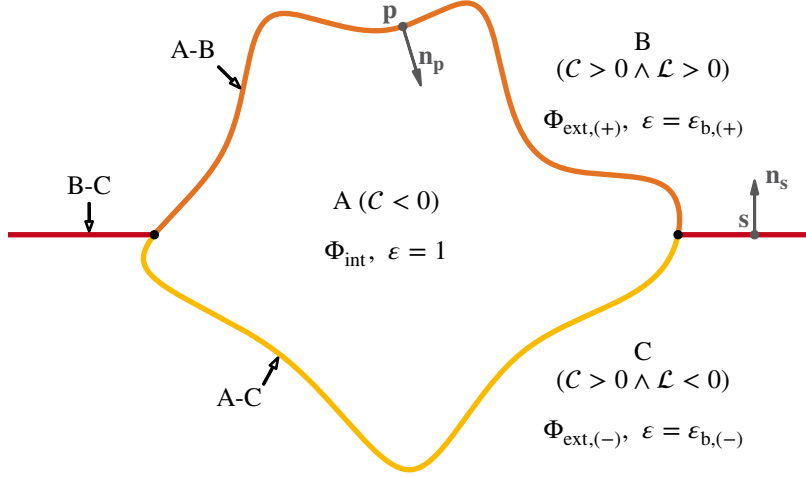


Fig. 7.2: Schematic picture of a solvation cavity at a planar interface between two dielectrics. The cavity function  $\mathcal{C}$  and the interface function  $\mathcal{L}$  define the three important regions, i.e., inside the cavity (A), in the upper dielectric (B), and in the lower one (C). The interfaces between these regions are labeled correspondingly and drawn in different colors.

## 7.2 Combination of Solvation Cavity with Planar Interface

Having demonstrated the applicability of the MPE model for charge distributions in a cavity surrounded by a homogeneous dielectric continuum in section 4.3 and for a charge at a planar interface between two dielectrics in section 7.1, we will now combine the two models to a situation illustrated in Fig. 7.2 where a solvation cavity hosting a charge distribution is in contact with two different dielectrics.

In such a case, we can define the three involved subspaces—using the previously introduced cavity and interface functions—as well as the electrostatic potential ansatz therein,

A Inside the cavity where the solute resides,

$$\Phi_{\text{int}}(\mathbf{r}) = \Phi_{\text{H}}(\mathbf{r}) + \Phi_{\text{R}}(\mathbf{r}), \quad \mathcal{C}(\mathbf{r}) < 0, \quad (7.13a)$$

B in the subspace of one dielectric,

$$\Phi_{\text{ext},(+)}(\mathbf{r}) = \varepsilon_{\text{b},(+)}^{-1} \Phi_{\text{H}}(\mathbf{r}) + \Phi_{\text{O}}(\mathbf{r}), \quad \mathcal{L}(\mathbf{r}) > 0 \wedge \mathcal{C}(\mathbf{r}) > 0, \quad (7.13b)$$

and

C in the subspace of the other one,

$$\Phi_{\text{ext},(-)}(\mathbf{r}) = \varepsilon_{\text{b},(-)}^{-1} \Phi_{\text{H}}(\mathbf{r}) + \Phi_{\text{Q}}(\mathbf{r}), \quad \mathcal{L}(\mathbf{r}) > 0 \wedge \mathcal{C}(\mathbf{r}) > 0. \quad (7.13c)$$

Since the dielectric permittivity function is constant within these regions, they are all labeled “continuum” in the following.

### 7.2.1 Multipole Expansion of Potentials

Concerning the multipole expansions of the electrostatic potentials, the exact same expressions can be used as for the case of a single homogeneous continuum—except that there are now two independent expansions for the potentials in the two different dielectrics. Thus, the potential expression in region A is chosen identical to Eq. (4.1a),

$$\Phi_R(\mathbf{r}) = \sum_{l=0}^{l_{\max,R}} \sum_{m=-l}^l R_K^{(l,m)} \mathcal{R}_m^l(\mathbf{r} - \mathbf{r}_K), \quad (7.14a)$$

while for the expansions in B,

$$\Phi_O(\mathbf{r}) = \sum_{J=1}^N \sum_{l=0}^{l_{\max,O}} \sum_{m=-l}^l O_J^{(l,m)} \mathcal{I}_m^l(\mathbf{r} - \mathbf{r}_J), \quad (7.14b)$$

and C,

$$\Phi_Q(\mathbf{r}) = \sum_{J=1}^N \sum_{l=0}^{l_{\max,Q}} \sum_{m=-l}^l Q_J^{(l,m)} \mathcal{I}_m^l(\mathbf{r} - \mathbf{r}_J), \quad (7.14c)$$

the same expression of Eq. (4.1b) is used. In contrast to Eqs. (7.9a) and (7.9b), the same expansion centers may be used in Eqs. (7.14b) and (7.14c) because all of these centers are situated in the cavity and not in one of the two dielectrics.

### 7.2.2 Discretization of the Interfaces

The continua A, B, and C share different interfaces which, in turn, can be characterized using the same functions, i.e.

A-B

$$\left\{ \mathbf{p} \mid \mathcal{C}(\mathbf{p}) = 0 \wedge \mathcal{L}(\mathbf{p}) > 0 \right\},$$

A-C

$$\left\{ \mathbf{p} \mid \mathcal{C}(\mathbf{p}) = 0 \wedge \mathcal{L}(\mathbf{p}) < 0 \right\},$$

and

B-C

$$\left\{ \mathbf{s} \mid \mathcal{L}(\mathbf{s}) = 0 \wedge \mathcal{C}(\mathbf{s}) > 0 \right\},$$

which is also illustrated in Fig. 7.2. In order to apply the MPE method, it is crucial to determine points on these interfaces. For this task, the same methods as previously discussed can be used. First, the implicit solvation cavity is created exactly as described in chapter 5. These points are then assigned to the corresponding interface A-B or A-C depending on the aforementioned conditions.

Then, a log-polar grid of points is spanned on the planar interface centered at the projection of the nuclei's mean position—or, alternatively, the mean position of all density walkers—on the interface plane. Thereby, the minimum and maximum radius, cf. Eq. (7.11), can be provided as an input with default values of  $1 a_0$  and  $100 a_0$ , respectively. The number of required points is chosen according to the desired degree of determination,  $d_{\text{det}}$ —a concept introduced in section 4.1.2.

It should be noted that the definition of  $d_{\text{det}}$  is here applied to parts of the full SLE belonging to the different interfaces, e.g. the ratio of the number of points on the interface A-B to the total number of coefficients in the multipole expansions for the potentials in the regions A and B should approximately be equal to  $d_{\text{det}}$ . From the initialized set of points on the interface, however, all points that would end up inside of the cavity, i.e. where  $\mathcal{C} < 0$ , need to be discarded. For the sake of simplicity, it is assumed that approximately the same number of points end up in the interfaces A-B and A-C and the fact that points on the interface are discarded is ignored. Depending on the shape and position of the cavity relative to the interface, these simplifications might be completely unjustified and lead to an ill-posed SLE. Thus, this aspect definitely requires further attention in the future but for the mere proof of concept of the method the current implementation should suffice—especially for large enough values for  $d_{\text{det}}$ .

### 7.2.3 MPE Equations

Evaluating the by now well-known boundary conditions for the electrostatic potentials Eqs. (7.13a) to (7.13c) with the corresponding multipole expansions, Eqs. (7.14a) to (7.14c), at suitable points leads to a similar but larger SLE than before which we will therefore display in the following, abbreviated form:

$$\begin{pmatrix} \underline{\mathbf{A}}_{A-B,R} & \underline{\mathbf{A}}_{A-B,O} & \underline{\mathbf{0}} \\ \underline{\mathbf{A}}_{A-C,R} & \underline{\mathbf{0}} & \underline{\mathbf{A}}_{A-C,Q} \\ \underline{\mathbf{0}} & \underline{\mathbf{A}}_{B-C,O} & \underline{\mathbf{A}}_{B-C,Q} \end{pmatrix} \begin{pmatrix} \mathbf{x}_R \\ \mathbf{x}_O \\ \mathbf{x}_Q \end{pmatrix} = \begin{pmatrix} \mathbf{b}_{A-B} \\ \mathbf{b}_{A-C} \\ \mathbf{b}_{B-C} \end{pmatrix} \quad (7.15)$$

The above equation consists of subproblems for each individual interface between two regions which themselves are virtually identical to Eq. (4.9) or Eq. (7.12)—e.g.

$$\begin{pmatrix} \underline{\mathbf{A}}_{A-C,R} & \underline{\mathbf{A}}_{A-C,Q} \end{pmatrix} \begin{pmatrix} \mathbf{x}_R \\ \mathbf{x}_Q \end{pmatrix} = \mathbf{b}_{A-C} \quad , \quad (7.16)$$

for the interface A-C. These subproblems, however, are coupled and thus need to be solved either together in one matrix equation or in an iterative procedure. Fortunately, the same numerical methods as presented in chapter 4 can be employed for the former approach such that we can directly test the method in a proof-of-concept application without further ado.

### 7.2.4 Heterogeneous 2D Model Systems: Comparison to FEM

Since the FEM solution has already served as a benchmark for the MPE method for the embedding of a cavity in a homogeneous dielectric, cf. section 4.3.2, as well as for the case of a charge at a planar dielectric interface, cf. section 7.1.3, it is obvious to compare the results of both methods also in this case—especially since all necessary modifications for the FEM to include the dielectric interface are already in place. To this end, we set up a similar test suite as in section 4.3.2 in which the spherical cavity of radius  $r_c = 1 a_0$  centered at the origin intersects with an interface plane

defined by the equation  $\zeta = \zeta_0$ . Note that the imposed cylindrical symmetry of the problem again implies that the electrostatic potential *in vacuo* is representable in the following expansion where only multipole terms with  $m = 0$  contribute,

$$\Phi_0(\rho, \zeta) = \sum_{i=1}^n M_i^{(l_i, 0)} \mathcal{I}_{(l_i, 0)}(\rho, \zeta - \zeta_i). \quad (7.17)$$

Here,  $n$  is the number of multipoles of order  $l_i$  and magnitude  $M_i$  positioned on the  $\zeta$  axis at a value of  $\zeta_i$ . The exact same model potentials as in section 4.3.2 are used, i.e.

$$\begin{aligned} n &\in \{1, 2, 3\}, \\ l_i &\in \{0, 1, 2\}, \\ M_i^{(l_i, 0)} &\in \{-1, 1\}, \end{aligned}$$

and

$$\zeta_i \in \{-0.6, -0.3, 0.0, 0.3, 0.6\}.$$

We allow the additional planar dielectric interfaces to be placed at three different positions,

$$\zeta_0 \in \{-0.5, 0.0, 0.5\},$$

to gauge the influence different symmetries and numbers of discretization points on the cavity have on the method's accuracy. The dielectric permittivities may assume the following values,

$$\begin{aligned} \varepsilon_{b,(+)} &\in \{10^{0.0}, 10^{0.4}, 10^{0.8}, 10^{1.2}, 10^{1.6}, 10^{2.0}\} \approx \{1, 2.51, 6.31, 15.8, 39.8, 100\}, \\ \varepsilon_{b,(-)} &\in \{10^{0.8}, 10^{1.6}, 10^{2.4}\} \approx \{6.31, 39.8, 251\}, \end{aligned}$$

under the additional constraint that  $\varepsilon_{b,(+)} \neq \varepsilon_{b,(-)}$ —which would simply be the case of a single, homogeneous dielectric.

In summary, 1339200 combinations can be formed out of which, for the moment, only a comparatively small and randomly selected sample of 5276 are investigated using the MPE and the FEM method. The comparison between the results is done completely analogously to section 4.3.2. Figure 7.3 illustrates the reaction field found by both methods for a randomly chosen model system. The correlation of the fictitious energy expressions, cf. Eq. (4.40), is displayed in Fig. 7.4. Studying these correlations one observes that the kind of fictitious charge density (homogeneously *versus* Gaussian distributed) has basically no influence on the results. Furthermore, there is a systematic improvement in the agreement between the two methods with increasing expansion order of the MPE potential. The same aspects have also been found for the correlations in Fig. 4.7. In the case of two dielectrics studied here, however, a much higher expansion order is required to obtain equally small deviations, e.g. the RMSD value  $\zeta$  for  $l_{\max, R} = 8$  is comparable to the one found for  $l_{\max, R} = 4$  in the case of an embedding in a single dielectric medium. Considering the number of expansion terms this means a significant increase from 25 to 81 to reach the same potential quality. Fortunately, the size of the total SLE is dominated with increasing number of expansion centers by the orders  $l_{\max, O}$  and  $l_{\max, Q}$ —to which our results again seem to be much less sensitive. Most probably, this increase is directly related to a more complex shape of the electrostatic potential



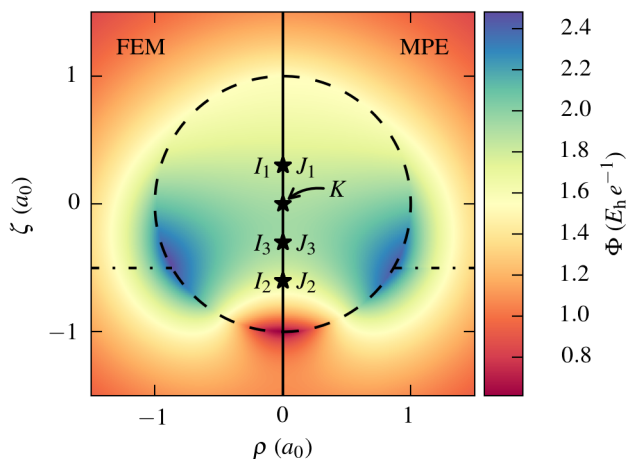


Fig. 7.3: Exemplary benchmark setup. The point multipoles are placed at centers  $I_i$  on the  $\zeta$  axis within a cavity of radius  $r_c$  (dashed circle). The interface between the two dielectrics (dashed and dotted line) is situated at  $\zeta = -0.5 a_0$ . The MPE expansion centers are placed at sites  $K$  and  $J_i$  with respective expansion orders of  $l_{\max,O} = 6$ ,  $l_{\max,Q} = 6$ , and  $l_{\max,R} = 6$ . The resulting potentials for FEM and MPE are shown in color-code on the left and right hand side of the plot.

inside the cavity due to the reduced symmetry of the outside medium. Since realistic systems like the small organic molecules presented in section 6.1 are intrinsically less symmetric than the idealized model systems used here, we may even hope that the corresponding increase in expansion order in such systems will also manifest itself less strongly.

### 7.2.5 Final Remarks

A final note about the heterogeneous MPE model concerns the shape of the interface between the two dielectrics. We want to stress here that the electrostatic equations at the interface, Eq. (7.12), which enter the full SLE, Eq. (7.15), by no means require this interface to be planar. Like in the case of the solvation cavity, any (smooth enough) surface can be treated given an appropriate set of points on it with corresponding normal vectors. Simply due to the lack of an analytical solution for arbitrary shapes and the imposed symmetry in the FEM calculations, we restricted ourselves to a planar geometry in the examples above.

For the non-electrostatic contributions presented in section 3.4, the situation is different. Since the non-electrostatic parameters may be different for the two dielectrics, the question is by what portions of the solvation cavity's total surface area and volume they are multiplied. Here, the previous assignment of the area elements to each point on the cavity, cf. section 5.4.3, is of great help to us. Summing up the contributions separately for the cavity interfaces, i.e. A-B and A-C, we can immediately identify the individual contact area between the solute and the dielectrics, i.e. B and C, to which then the corresponding parameter can be applied. An equivalent summation of the individual volume elements,  $A[B]$  and  $A[C]$ , is straightforward in the case of a planar interface between B and C when any point on this interface is used as the origin  $\mathbf{o}$  in Eq. (5.45). In the case of arbitrarily shaped interfaces, the procedure is more complicated yet still possible in a similar fashion if the interface is propagated through the cavity. Defining an internal boundary in the

cavity,

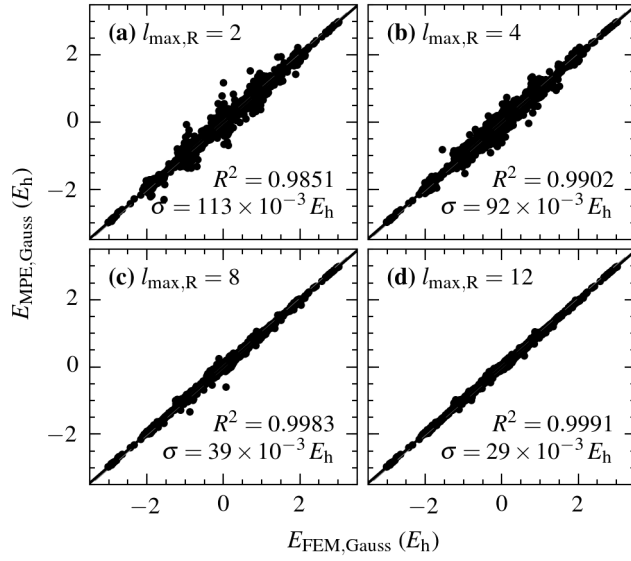
A[B]-A[C]

$$\{ \mathbf{s} \mid \mathcal{L}(\mathbf{s}) = 0 \wedge \mathcal{C}(\mathbf{s}) < 0 \},$$

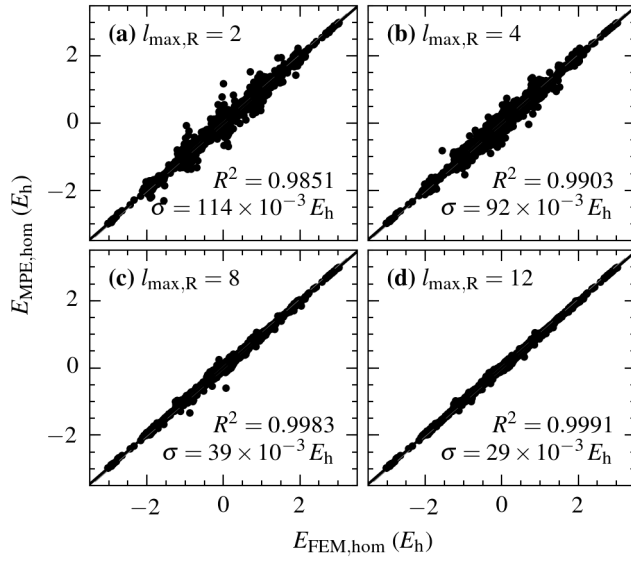
points on it can be used for a closure of both volume parts such that any point can be used again as the origin for the calculation of the volume elements<sup>1</sup>. Questions on whether this kind of non-electrostatic correction at the interface of two dielectrics is applicable at all, or whether a binary distribution of the area and volume elements is appropriate, are left to be answered in future works.

---

<sup>1</sup>Attention has to be paid to the sign definition of the normal vectors on the internal boundary. The normal directions need to be exactly opposite for the two sub-volumes.



(a) Gaussian charge density



(b) Homogeneous charge density

Fig. 7.4: Correlation graph for FEM and MPE interaction energies  $E$  of the polarization potential, as defined in Eq. (4.40), in the case of two dielectrics. MPE potential expansion orders are  $l_{\max,O} = 6$ ,  $l_{\max,Q} = 6$ , and  $l_{\max,R}$  as indicated in the different panels.

## 8 Conclusion ‡

---

Having set the stage with the necessary theoretical foundations in the earlier chapters, we introduced a re-formulation of the classic MPE model in chapter 3 and thereby established an outlying-charge-error free electrostatic implicit solvation model based on a sufficiently accurate knowledge of the solute’s Hartree potential, i.e. its electrostatic potential *in vacuo*. As we pointed out, this formulation could also be transferred to an ASC-like model which, contrary to all currently available implementations, would need to employ an apparent surface *dipole* distribution.

The implementation of this model in the all-electron electronic structure code FHI-aims, demonstrated in chapter 4, partially focuses on some specifics of this code such as the localized basis set or the multi-polar expansion of density and electrostatic potential. For example, we readily exploit FHI-aims’ efficient way of evaluating the Hartree potential at arbitrary points in real-space in its standard SCF cycle, thus greatly reducing the overhead necessary to perform implicit solvation calculations. Nonetheless, it should be pointed out that an efficient implementation of the presented method could be realized in any classical or quantum mechanical framework that allows for an efficient evaluation of the Hartree potential (and the electron density for creation of the iso-density cavity) at arbitrary points in real space.

In chapter 5, we presented a novel method of finding an evenly distributed set of points at the solvation cavity surface based on a damped molecular dynamics scheme of cavity point walkers which are propagated on a fictitious potential energy surface that is designed to yield fast convergence of the procedure. Given such a set of points, we also put forward a trivially parallel way to determine surface area and volume of the point cloud using a local Voronoi-tessellation which is found to be in excellent agreement with more involved algorithms in dedicated reference codes. The number of points at the solvation cavity surface is thereby chosen such that the resulting system of linear equations exhibits a certain degree of determination, i.e., an excess of conditions with respect to variables. We carefully gauged the degree of determination necessary to maximize the rank of the MPE coefficient matrix while at the same time keeping the computational cost low, to find that the optimal accuracy and efficiency is already reached at a threefold over-determination.

The reliability and accuracy of the implementation was tested in two main stages. First, we assessed the quality of the improved, outlying-charge-error free electrostatic model by comparing our implementation to the analytical solution of the Born point-charge model—finding near perfect agreement—and, on the basis of  $\approx 140000$  2D model cases, to a high-accuracy FEM method. More specifically, we compared the solvent response potentials calculated by both methods which again show very good correlation and very small standard deviations already at low multipole moment expansion orders of the MPE approach.

Afterwards, the general applicability of the full MPE model, i.e. the electrostatic model combined with a simple established non-electrostatic contribution [21], to realistic systems was demonstrated for different molecular test-sets (neutral and singly charged) all of which have already been

---

‡Reprinted in parts with permission from Ref. [1]. © 2017 American Chemical Society.

included in other implicit solvation studies. Based on a fit to a combination of test-sets, we presented an optimized parameter set (MPE-SPANC) for use with an iso-density cavity based on a converged vacuum density which showed very good accuracy for both neutral and cationic solutes. A variant of MPE-SPANC without non-electrostatic volume term (MPE-SPANC-surf) was also given to facilitate the model's use in future work. For all combinations of density functionals and optimized parameter sets, our method showed mean absolute errors with respect to experimentally measured free energies of hydration below 49 meV for neutral molecules and 111 meV for cations (85 meV for the selectively clustered set). These numbers compare very well to the performance of other implicit solvation models with a similar non-electrostatic model [21, 42, 69, 80]. For neutral molecules in water, a better description can be achieved by the so-called "SMx" models (with reported MAEs of 24 meV for SM8 [46], 26 to 41 meV for SMD [47], 25 to 36 meV for SM12 [48]) or by CMIRS [91] (with a reported MAE of 34 meV) and other models that employ more elaborate descriptions of the non-electrostatic terms. All of these models, however, rely on at least a few up to many more tunable parameters.

Similar to the findings of others using the same very simple non-electrostatic model used here together with an iso-density [80] or with a soft-sphere cavity [69], we were unable to determine a single set of parameters within this model to describe neutral, cationic and anionic molecules at the same time even remotely as accurately as neutrals/cations and anions separately. A parameter fit exclusively for anions showed mean absolute errors below 178 meV (141 meV for the selectively clustered set) which is also in good agreement with the performance of other implicit solvation methods [48, 69, 80, 91]. Subsequently, we proposed a first and easily realizable measure to overcome this problem, namely to use the superposition of neutral free atom densities as a basis for the iso-density cavity.

As finally observed in section 6.6, the dominating computational effort in applying the MPE solvation model could be attributed to three separate tasks, i.e. finding a set of points on the cavity surface, determining the numerical solution of an over-determined system of linear equations arising from electrostatic boundary conditions at the interface, and evaluating the reaction field on the integration grid of the DFT code. The relative overhead cost of a single-point DFT energy calculation of our method over the respective vacuum calculations only amounts to approximately 20 % for a GGA or less than 5 % for hybrid functionals in total for the here considered small organic solutes. For larger systems, the overhead is estimated to be even lower due to the favorable scaling of our approach.

At this low cost the presented DFT+MPE implicit solvation method constitutes an appealing approach to effectively treat solvation effects in first-principles calculations. Another positive aspect is the minimal invasion into the regular SCF procedure in FHI-aims which merely amounts to evaluating the reaction field after the integration of the Hartree potential and adding them up on the integration grid. The employed non-electrostatic contributions are then only a final post-correction on the total energy. It should be noted here that no modifications of core functionalities, such as e.g. the Poisson solver, were conducted except for said routine that sums up the total electrostatic potential on the integration grid. A combination with other existing or in the future developed features is clearly facilitated by the simplicity of this approach.

Indisputably, the current implementation still needs to be amended by important features such as analytic force evaluation. In contrast to the latter, however, we do not consider the correct treatment of periodic boundary conditions to be an urgent extension to the model—although periodicity is in fact also very important in the context of continuum embedding, e.g., at the surface of a solid in contact with a liquid. In this case, QM/MM embedding [12] can be a viable

approach to circumvent the explicit treatment of the solid surface's 2D periodicity and represent the QM system with a non-periodic cluster. As a first step in the direction of treating such systems, we presented a modification of the MPE model that allows us to include an interface of two liquids or of a liquid and air in our simulations. The proposed extension has successfully passed the presented proof-of-concept benchmark tests for a spherical cavity at a planar interface between two dielectrics. Therefore, we are confident about the potential of the presented method and look forward to seeing its performance in more realistic applications such as, e.g., molecular catalysis at liquid-liquid interfaces.



## *Acknowledgments / Danksagung*

---

First and foremost I want to thank Karsten Reuter for supporting me during my thesis and giving advice when needed. Even more so, thank you for your relentless effort to prepare your students for a life after the PhD by teaching us much more than just science.

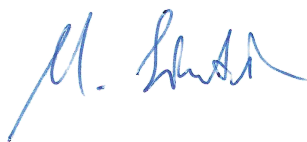
Likewise, I want to express my gratitude to my second supervisor and mentor, Harald Oberhofer, for always lending his ear to me in need and motivating me in times of frustration.

I am also indebted to many other (also former) colleagues in the group who supported me during this time. In particular, I would like to thank Christoph Scheurer and Sebastian Matera for sharing with me their profound knowledge about linear algebra and numerical methods. I highly appreciated the invaluable effort of Ruth Mösch who keeps the wheel turning despite all administrative barriers, as well as the work of our IT crew: Georg Michelitsch, Christoph II Schober, Matthias Kick, Max Hoffmann, Juan Manuel Lorenzi, Christoph III Muschielok, and Christian Kunkel. Furthermore, little of our group workshops and outings would have been possible without organizational talents in our group as Vanessa Jane Bukas, Georg Michelitsch, Simone Köcher, David Egger, and Hendrik Helge Heenen, to mention just a few. Lastly, I owe a big thanks to my officemate Simon Rittmeyer who helped me in many cases with his unmistakable sense of style and his impressive skill set concerning the production of plots and figures. Thank you all for creating, through your devotion and kindness, such a warm and friendly atmosphere that makes going to work feel a little like coming home.

Moreover, I want to thank Volker Blum for inviting me to his group at Duke twice and for the many enlightening discussions that we had. I am deeply grateful for him and his family hosting me several times and taking me on an unforgettable Easter trip to the Outer Banks. I also want to particularly thank Raul Laasner, Victor Yu, Will Huhn, Tong Zhu, and Björn Lange for the lovely time we shared during my visits playing board games, drinking, and talking about science and all sorts of things. On this occasion, the TUM Graduate School's financial travel support is gratefully acknowledged.

Besonderer Dank gilt meiner Lebensgefährtin, die mich viele Male aufgebaut und motiviert hat. Danke, Sandra, für deine Geduld, deine Ehrlichkeit und dafür, dass du mir immer wieder auch eine andere Sicht der Dinge ermöglichst. Zuletzt, aber am meisten, möchte ich mich bei meinen Eltern bedanken für die bedingungslose Unterstützung und Liebe, die sie mir all die Jahre zuteil werden ließen, auch wenn ich meine eigenen Wege ging.

Ismaning, January 2018







# Bibliography

---

- [1] M. Sinstein, C. Scheurer, S. Matera, V. Blum, K. Reuter, and H. Oberhofer, *J. Chem. Theory Comput.* **13**, 5582 (2017) (cit. on pp. i, 16, 27–29, 31, 41, 44, 51, 58, 59, 61, 63, 65, 68–71, 77, 79, 93).
- [2] V. Tripkovic, M. E. Björketun, E. Skúlason, and J. Rossmeisl, *Phys. Rev. B* **84**, 115452 (2011) (cit. on p. 1).
- [3] M. Sprik, J. Hutter, and M. Parrinello, *J. Chem. Phys.* **105**, 1142 (1996) (cit. on p. 1).
- [4] A. P. Gaiduk, F. Gygi, and G. Galli, *J. Phys. Chem. Lett.* **6**, 2902 (2015) (cit. on p. 1).
- [5] A. P. Gaiduk and G. Galli, *J. Phys. Chem. Lett.* **8**, 1496 (2017) (cit. on p. 1).
- [6] S. Schnur and A. Groß, *Catal. Today* **165**, 129 (2011) (cit. on p. 1).
- [7] J. F. Ouyang and R. P. A. Bettens, *Chimia* **69**, 104 (2015) (cit. on p. 1).
- [8] B. Guillot, *J. Mol. Liq.* **101**, 219 (2002) (cit. on p. 1).
- [9] A. P. Seitsonen and T. Bryk, *Phys. Rev. B* **94**, 184111 (2016) (cit. on p. 1).
- [10] M. Chen, H.-Y. Ko, R. C. Remsing, M. F. Calegari Andrade, B. Santra, Z. Sun, A. Selloni, R. Car, M. L. Klein, J. P. Perdew, and X. Wu, *Proc. Natl. Acad. Sci. U.S.A.* **114**, 10846 (2017) (cit. on p. 1).
- [11] J. Sun, A. Ruzsinszky, and J. P. Perdew, *Phys. Rev. Lett.* **115**, 036402 (2015) (cit. on p. 1).
- [12] D. Berger, A. J. Logsdail, H. Oberhofer, M. R. Farrow, C. R. A. Catlow, P. Sherwood, A. A. Sokol, V. Blum, and K. Reuter, *J. Chem. Phys.* **141**, 024105 (2014) (cit. on pp. 1, 94).
- [13] H. J. Kulik, J. Zhang, J. P. Klinman, and T. J. Martínez, *J. Phys. Chem. B* **120**, 11381 (2016) (cit. on p. 1).
- [14] T. Stecher, K. Reuter, and H. Oberhofer, *Phys. Rev. Lett.* **117**, 276001 (2016) (cit. on p. 1).
- [15] H. Lin and D. Truhlar, *Theor. Chem. Acc.* **117**, 185 (2007) (cit. on p. 1).
- [16] J. Tomasi, B. Mennucci, and R. Cammi, *Chem. Rev.* **105**, 2999 (2005) (cit. on pp. 2, 11, 13, 18–20, 23, 48).
- [17] S. Ringe, “First-Principles Modeling in Poisson-Boltzmann Electrolytes,” Dissertation (Technische Universität München, München, 2017) (cit. on pp. 2, 13).
- [18] J. Mayer, K. Khairy, and J. Howard, *Am. J. Phys.* **78**, 648 (2010) (cit. on p. 2).
- [19] J. G. Kirkwood, *J. Chem. Phys.* **2**, 351 (1934) (cit. on pp. 2, 20, 40, 51).
- [20] D. Rinaldi, A. Bouchy, J.-L. Rivail, and V. Dillet, *J. Chem. Phys.* **120**, 2343 (2004) (cit. on pp. 2, 20, 45, 48, 51).
- [21] O. Andreussi, I. Dabo, and N. Marzari, *J. Chem. Phys.* **136**, 064102 (2012) (cit. on pp. 2, 15, 23, 51, 60, 65, 72, 76, 93, 94).

- [22] V. Blum, R. Gehrke, F. Hanke, P. Havu, V. Havu, X. Ren, K. Reuter, and M. Scheffler, *Comp. Phys. Commun.* **180**, 2175 (2009) (cit. on pp. 2, 45, 58, 67).
- [23] V. Havu, V. Blum, P. Havu, and M. Scheffler, *J. Comput. Phys.* **228**, 8367 (2009) (cit. on p. 2).
- [24] X. Ren, P. Rinke, V. Blum, J. Wieferink, A. Tkatchenko, A. Sanfilippo, K. Reuter, and M. Scheffler, *New J. Phys.* **14**, 053020 (2012) (cit. on p. 2).
- [25] A. C. Ihrig, J. Wieferink, I. Y. Zhang, M. Ropo, X. Ren, P. Rinke, M. Scheffler, and V. Blum, *New J. Phys.* **17**, 093020 (2015) (cit. on p. 2).
- [26] H. Hoshi, M. Sakurai, Y. Inoue, and R. Chûjô, *J. Chem. Phys.* **87**, 1107 (1987) (cit. on p. 3).
- [27] R. Bonaccorsi, E. Ojalvo, P. Palla, and J. Tomasi, *Chem. Phys.* **143**, 245 (1990) (cit. on p. 3).
- [28] H. Houjou, M. Sakurai, and Y. Inoue, *J. Chem. Phys.* **107**, 5652 (1997) (cit. on p. 3).
- [29] S. Aono, T. Hosoya, and S. Sakaki, *Phys. Chem. Chem. Phys.* **15**, 6368 (2013) (cit. on p. 3).
- [30] M. H. Abraham, J. Liszi, and L. Mészáros, *J. Chem. Phys.* **70**, 2491 (1979) (cit. on p. 3).
- [31] P. Ge, M. D. Scanlon, P. Peljo, X. Bian, H. Vubrel, A. O'Neill, J. N. Coleman, M. Cantoni, X. Hu, K. Kontturi, B. Liu, and H. H. Girault, *Chem. Commun.* **48**, 6484 (2012) (cit. on pp. 3, 81).
- [32] X. Bian, M. D. Scanlon, S. Wang, L. Liao, Y. Tang, B. Liu, and H. H. Girault, *Chem. Sci.* **4**, 3432 (2013) (cit. on pp. 3, 81).
- [33] F. Jensen, *Introduction to Computational Chemistry*, 2nd ed. (John Wiley & Sons, 2006) (cit. on p. 5).
- [34] A. Szabo and N. Ostlund, *Modern Quantum Chemistry: Introduction to Advanced Electronic Structure Theory*, Dover Books on Chemistry (Dover Publications, 1989) (cit. on p. 5).
- [35] C. Adamo and V. Barone, *J. Chem. Phys.* **110**, 6158 (1999) (cit. on pp. 10, 67).
- [36] J. P. Perdew, K. Burke, and M. Ernzerhof, *Phys. Rev. Lett.* **77**, 3865 (1996) (cit. on pp. 10, 67).
- [37] J. Heyd, G. E. Scuseria, and M. Ernzerhof, *J. Chem. Phys.* **118**, 8207 (2003) (cit. on pp. 10, 67).
- [38] J. Heyd, G. E. Scuseria, and M. Ernzerhof, *J. Chem. Phys.* **124**, 219906 (2006) (cit. on pp. 10, 67).
- [39] J. P. Perdew, A. Ruzsinszky, J. Tao, V. N. Staroverov, G. E. Scuseria, and G. I. Csonka, *J. Chem. Phys.* **123**, 062201 (2005) (cit. on p. 10).
- [40] F. Booth, *J. Chem. Phys.* **19**, 391 (1951) (cit. on p. 13).
- [41] W. H. Hayt, Jr and J. A. Buck, *Engineering Electromagnetics*, 6th ed. (McGraw-Hill, 2001) (cit. on pp. 14, 16, 82).
- [42] S. Ringe, H. Oberhofer, C. Hille, S. Matera, and K. Reuter, *J. Chem. Theory Comput.* **12**, 4052 (2016) (cit. on pp. 15, 51, 65, 94).
- [43] M. Born, *Z. Physik* **1**, 45 (1920) (cit. on pp. 17, 40).
- [44] O. D. Kellogg, *Foundations of Potential Theory*, edited by R. Courant, W. Blaschke, M. Born, and C. Runge, 1st ed., 1929, *Grundlehren der mathematischen Wissenschaften 31* (Springer, 1967) (cit. on pp. 17, 18).
- [45] W. C. Still, A. Tempczyk, R. C. Hawley, and T. Hendrickson, *J. Am. Chem. Soc.* **112**, 6127 (1990) (cit. on p. 18).

- [46] C. J. Cramer and D. G. Truhlar, *Acc. Chem. Res.* **41**, 760 (2008) (cit. on pp. 18, 94).
- [47] A. V. Marenich, C. J. Cramer, and D. G. Truhlar, *J. Phys. Chem. B* **113**, 6378 (2009) (cit. on pp. 18, 94).
- [48] A. V. Marenich, C. J. Cramer, and D. G. Truhlar, *J. Chem. Theory Comput.* **9**, 609 (2013) (cit. on pp. 18, 65, 71, 94).
- [49] D. M. Chipman, *J. Chem. Phys.* **106**, 10194 (1997) (cit. on pp. 19, 20).
- [50] C.-G. Zhan, J. Bentley, and D. M. Chipman, *J. Chem. Phys.* **108**, 177 (1998) (cit. on pp. 19, 51).
- [51] D. M. Chipman, *J. Chem. Phys.* **110**, 8012 (1999) (cit. on p. 19).
- [52] S. Miertuš, E. Scrocco, and J. Tomasi, *Chem. Phys.* **55**, 117 (1981) (cit. on p. 19).
- [53] D. M. Chipman, *J. Chem. Phys.* **112**, 5558 (2000) (cit. on p. 20).
- [54] E. Cancès and B. Mennucci, *J. Chem. Phys.* **115**, 6130 (2001) (cit. on p. 20).
- [55] A. Klamt and G. Schuurmann, *J. Chem. Soc., Perkin Trans. 2* **2**, 799 (1993) (cit. on p. 20).
- [56] L. Onsager, *J. Am. Chem. Soc.* **58**, 1486 (1936) (cit. on pp. 20, 51).
- [57] J.-L. Rivail and D. Rinaldi, *Chem. Phys.* **18**, 233 (1976) (cit. on pp. 20, 51).
- [58] D. Rinaldi, M. F. Ruiz-Lopez, and J.-L. Rivail, *J. Chem. Phys.* **78**, 834 (1983) (cit. on p. 20).
- [59] V. Dillet, D. Rinaldi, J. G. Ángyán, and J.-L. Rivail, *Chem. Phys. Lett.* **202**, 18 (1993) (cit. on pp. 20, 45).
- [60] E. Cancès, in *Continuum Solvation Models in Chemical Physics: From Theory to Applications*, edited by B. Mennucci and R. Cammi (John Wiley & Sons, 2008), p. 29 (cit. on p. 22).
- [61] J. Tomasi and M. Persico, *Chem. Rev.* **94**, 2027 (1994) (cit. on p. 23).
- [62] D. A. Scherlis, J.-L. Fattebert, F. Gygi, M. Cococcioni, and N. Marzari, *J. Chem. Phys.* **124**, 074103 (2006) (cit. on pp. 23, 24, 51).
- [63] A. Bondi, *J. Phys. Chem.* **68**, 441 (1964) (cit. on p. 24).
- [64] L. Pauling, *The Nature of the Chemical Bond*, 3rd ed. (Cornell University Press, 1960) (cit. on p. 24).
- [65] D. Qiu, P. S. Shenkin, F. P. Hollinger, and W. C. Still, *J. Phys. Chem. A* **101**, 3005 (1997) (cit. on p. 24).
- [66] M. L. Connolly, *J. Appl. Crystallogr.* **16**, 548 (1983) (cit. on p. 24).
- [67] J. L. Pascual-Ahuir, E. Silla, and I. Tuñón, *J. Comput. Chem.* **15**, 1127 (1994) (cit. on p. 24).
- [68] J.-L. Fattebert and F. Gygi, *J. Comput. Chem.* **23**, 662 (2002) (cit. on pp. 24, 51, 60).
- [69] G. Fiscaro, L. Genovese, O. Andreussi, S. Mandal, N. N. Nair, N. Marzari, and S. Goedecker, *J. Chem. Theory Comput.* **13**, 3829 (2017) (cit. on pp. 25, 71, 72, 94).
- [70] E. O. Steinborn and K. Ruedenberg, in *Advances in Quantum Chemistry*, Vol. 7, edited by P.-O. Löwdin (Academic Press, 1973), pp. 46–51 (cit. on pp. 27, 48).
- [71] A. Capelli and G. Garbieri, *Corso di analisi algebrica*, 1st ed. (F. Sacchetto, 1886) Chap. 5, pp. 373–390 (cit. on p. 30).
- [72] Å. Björck, *Numerical Methods for Least Squares Problems*, Other Titles in Applied Mathematics (Society for Industrial and Applied Mathematics, Jan. 1996) (cit. on pp. 34, 35, 39).

- [73] E. Anderson, Z. Bai, C. Bischof, S. Blackford, J. Demmel, J. Dongarra, J. Du Croz, A. Greenbaum, S. Hammarling, A. McKenney, and D. Sorensen, *LAPACK users' guide*, 3rd ed. (Society for Industrial and Applied Mathematics, Philadelphia, PA, 1999) (cit. on pp. 35, 36).
- [74] L. S. Blackford, J. Choi, A. Cleary, E. D'Azevedo, J. Demmel, I. Dhillon, J. Dongarra, S. Hammarling, G. Henry, A. Petitet, K. Stanley, D. Walker, and R. C. Whaley, *ScaLAPACK users' guide* (Society for Industrial and Applied Mathematics, Philadelphia, PA, 1997) (cit. on p. 36).
- [75] B. Erdmann, J. Lang, and R. Roitzsch, *KARDOS–User's Guide*, Konrad-Zuse-Zentrum für Informationstechnik (Berlin, 2002) (cit. on p. 40).
- [76] Y.-F. Li, Z.-P. Liu, L. Liu, and W. Gao, *J. Am. Chem. Soc.* **132**, 13008 (2010) (cit. on p. 40).
- [77] M. F. Ruiz-López, in *Solvation effects on molecules and biomolecules* (Springer, 2008), pp. 23–38 (cit. on p. 45).
- [78] D. M. Chipman, *Theor. Chem. Acc.* **107**, 80 (2002) (cit. on p. 51).
- [79] C.-G. Zhan and D. M. Chipman, *J. Chem. Phys.* **109**, 10543 (1998) (cit. on pp. 51, 72).
- [80] C. Dupont, O. Andreussi, and N. Marzari, *J. Chem. Phys.* **139**, 214110 (2013) (cit. on pp. 51, 71, 94).
- [81] V. I. Lebedev and D. N. Laikov, *Dokl. Math.* **59**, 477 (1999) (cit. on p. 52).
- [82] D. Frenkel and B. Smit, *Understanding Molecular Simulation*, 2nd ed. (Academic Press, Inc., Orlando, FL, USA, 2001) (cit. on p. 60).
- [83] P. Cignoni, M. Corsini, and G. Ranzuglia, *ERCIM News* **73**, 6 (2008) (cit. on p. 63).
- [84] D. Shivakumar, Y. Deng, and B. Roux, *J. Chem. Theory Comput.* **5**, 919 (2009) (cit. on p. 65).
- [85] D. R. Lide, ed., *CRC handbook of chemistry and physics: a ready-reference book of chemical and physical data*, 82. ed., 2001-2002 (CRC Press, 2001) Chap. 5, p. 2 (cit. on p. 65).
- [86] A. V. Marenich, C. P. Kelly, J. D. Thompson, G. D. Hawkins, C. C. Chambers, D. J. Giesen, P. Winget, C. J. Cramer, and D. G. Truhlar, *Minnesota solvation database – version 2012*, Minneapolis: University of Minnesota, 2012 (cit. on p. 65).
- [87] E. Jones, T. Oliphant, P. Peterson, et al., *SciPy: Open source scientific tools for Python*, [Online; accessed 2017-01-06], 2001– (cit. on p. 66).
- [88] R. H. Byrd, P. Lu, J. Nocedal, and C. Zhu, *SIAM J. Sci. Comput.* **16**, 1190 (1995) (cit. on p. 66).
- [89] C. Zhu, R. H. Byrd, P. Lu, and J. Nocedal, *ACM Trans. Math. Softw.* **23**, 550 (1997) (cit. on p. 66).
- [90] B. Hammer, L. B. Hansen, and J. K. Nørskov, *Phys. Rev. B* **59**, 7413 (1999) (cit. on p. 67).
- [91] Z.-Q. You and J. M. Herbert, *J. Chem. Theory Comput.* **12**, 4338 (2016) (cit. on pp. 71, 94).
- [92] H. Oberhofer and K. Reuter, *J. Chem. Phys.* **139**, 044710 (2013) (cit. on p. 72).
- [93] W. M. Latimer, K. S. Pitzer, and C. M. Slansky, *J. Chem. Phys.* **7**, 108 (1939) (cit. on p. 73).
- [94] D. L. Mobley, A. E. Barber, C. J. Fennell, and K. A. Dill, *J. Phys. Chem. B* **112**, 2405 (2008) (cit. on p. 73).
- [95] J. P. Bardhan and M. G. Knepley, *J. Chem. Phys.* **141**, 131103 (2014) (cit. on p. 73).

# Appendices

---

|          |   |            |
|----------|---|------------|
| <b>A</b> | <b>Calculation of Real Cartesian Solid Harmonic Functions in FHI-aims</b> | <b>105</b> |
| A.1      | Real Valued Cartesian Polynomials . . . . .                               | 105        |
| A.2      | Cartesian Regular Solid Harmonics . . . . .                               | 108        |
| A.2.1    | Gradient . . . . .  | 108        |
| A.2.2    | Scaled Function . . . . .   | 108        |
| A.2.3    | Gradient of Scaled Function . . . . .                                     | 108        |
| A.3      | Cartesian Irregular Solid Harmonics . . . . .                             | 109        |
| A.3.1    | Gradient . . . . .  | 109        |
| A.3.2    | Scaled Function . . . . .   | 109        |
| A.3.3    | Gradient of Scaled Function . . . . .                                     | 110        |
| <b>B</b> | <b>Solving the Generalized Poisson Equation Using Finite Elements</b>     | <b>111</b> |
| B.1      | Generalized Poisson Equation in Cylindrical Coordinates . . . . .         | 111        |
| B.2      | Spherical Cavity and Smoothing of Dielectric Function . . . . .           | 111        |
| B.2.1    | Gradient . . . . .  | 113        |
| B.2.2    | Outlook: Interface Between Two Dielectrics . . . . .                      | 113        |
| B.3      | Regularization of the Potential . . . . .                                 | 114        |
| B.3.1    | Analytical Expressions for Point Multipoles . . . . .                     | 115        |
| B.4      | Integration Weights on Triangular Grid . . . . .                          | 117        |
| B.5      | Computational Details for the Finite Element Solver . . . . .             | 117        |
| <b>C</b> | <b>Derivations Related to the Isodensity Cavity</b>                       | <b>119</b> |
| C.1      | Calculation of the Intersection Point of Two Lines in 2D . . . . .        | 119        |
| C.2      | Distance Scaling for Density-Walkers . . . . .                            | 120        |
| C.3      | Surface Area Curvature Correction Factor . . . . .                        | 121        |
| <b>D</b> | <b>Tables of Optimized Parameter Sets</b>                                 | <b>123</b> |
|          | <b>Appendix Bibliography</b>  | <b>127</b> |



# ***A Calculation of Real Cartesian Solid Harmonic Functions in FHI-aims***

---

For certain applications—e.g. when Cartesian gradients are needed—it is advantageous to express the spherical harmonics (which are functions of polar and azimuthal angles) in terms of Cartesian coordinates,  $(x, y, z)$ . Despite their name, this representation takes the very simple form

$$Y_m^l(x, y, z) = \sum_{l_x+l_y+l_z=l} c(m, l_x, l_y, l_z) \frac{x^{l_x} y^{l_y} z^{l_z}}{\left(\sqrt{x^2 + y^2 + z^2}\right)^l}. \quad (\text{A.1})$$

The scalar, real-valued coefficients  $c$  are thereby responsible to combine all possible Cartesian polynomials in such a way that the correct symmetry is obtained. Especially for large expansion orders  $l$ , many coefficients need to be 0 since there are

$$\frac{(l+1)(l+2)}{2}$$

possible combinations for the polynomial orders,  $(l_x, l_y, l_z)$ , such that

$$l_x + l_y + l_z = l,$$

whereas only  $2l + 1$  spherical harmonics of the same order  $l$  exist.

## ***A.1 Real Valued Cartesian Polynomials***

A method to calculate corresponding coefficients  $\tilde{c}$  for the complex valued Cartesian spherical harmonic functions  $\tilde{Y}_m^l$ ,

$$r^l \tilde{Y}_m^l = \sum_{l_x+l_y+l_z=l} \tilde{c}(m, l_x, l_y, l_z) x^{l_x} y^{l_y} z^{l_z}, \quad (\text{A.2})$$

where

$$r = \sqrt{x^2 + y^2 + z^2},$$



has been presented by Schlegel and Frisch [1],

$$\tilde{c}(m, l_x, l_y, l_z) = \sqrt{\frac{(2l+1)(l-|m|)!}{4\pi(l+|m|)!}} \times \frac{1}{2^l l!} \sum_{i=0}^{(l-|m|)/2} \binom{l}{i} \binom{i}{j} \frac{(-1)^i (2l-2i)!}{(l-|m|-2i)!} \times \sigma_{\pm} \sum_{k=0}^j (-1)^k \binom{j}{k} \binom{|m|}{l_x-2k}, \quad (\text{A.3})$$

with

$$l = l_x + l_y + l_z, \quad j = \frac{l_x + l_y - |m|}{2}, \quad \sigma_{\pm} = (-1)^{\pm \frac{(|m|-l_x)}{2}}.$$

As noted again by Schlegel and Frisch [1], the coefficient is zero if  $j$  is not an integer. While  $\tilde{c}(0, l_x, l_y, l_z)$  is always real, i.e. when  $m = 0$ , the other coefficients are not necessarily real due to the factor  $\sigma_{\pm}$  in Eq. (A.3). Nonetheless, real spherical harmonics are obtained by linear combinations of pairs of complex valued spherical harmonics  $\tilde{Y}_m^l$  and  $\tilde{Y}_{-m}^l$  [1], namely

$$\begin{aligned} \frac{1}{\sqrt{\pm 2}} (r^l \tilde{Y}_m^l \pm r^l \tilde{Y}_{-m}^l) &= \frac{1}{\sqrt{\pm 2}} \left[ \sum_{l_x+l_y+l_z=l} \tilde{c}(m, l_x, l_y, l_z) x^{l_x} y^{l_y} z^{l_z} \right. \\ &\quad \left. \pm \sum_{l_x+l_y+l_z=l} \tilde{c}(-m, l_x, l_y, l_z) x^{l_x} y^{l_y} z^{l_z} \right] \\ &= \sum_{l_x+l_y+l_z=l} \frac{1}{\sqrt{\pm 2}} [\tilde{c}(m, l_x, l_y, l_z) \pm \tilde{c}(-m, l_x, l_y, l_z)] x^{l_x} y^{l_y} z^{l_z}. \end{aligned} \quad (\text{A.4})$$

Since  $\tilde{c}(m, l_x, l_y, l_z)$  is in principle the same as  $\tilde{c}(-m, l_x, l_y, l_z)$ , only linear combinations with different signs in  $\sigma$  are non-vanishing, i.e.

$$\sigma_+ \pm \sigma_- = (-1)^{\frac{(|m|-l_x)}{2}} \pm (-1)^{-\frac{(|m|-l_x)}{2}} = (-1)^{\frac{(|m|-l_x)}{2}} [1 \pm (-1)^{|m|-l_x}]. \quad (\text{A.5})$$

We define

$$p = \begin{cases} \frac{(|m|-l_x)}{2}, & |m| - l_x = 2\lambda \\ \frac{(|m|-l_x-1)}{2}, & |m| - l_x = 2\lambda + 1 \end{cases}, \quad \lambda \in \mathbb{Z}. \quad (\text{A.6})$$

With this,

$$\sigma_+ \pm \sigma_- = \begin{cases} (-1)^p [1 \pm (-1)^{2p}], & |m| - l_x = 2\lambda \\ \sqrt{-1} \cdot (-1)^p [1 \pm (-1)^{2p+1}], & |m| - l_x = 2\lambda + 1 \end{cases}, \quad \lambda \in \mathbb{Z}. \quad (\text{A.7})$$

Since  $p$  is an integer number, the above expression can be simplified,

$$\sigma_+ \pm \sigma_- = \begin{cases} (-1)^p [1 \pm 1], & |m| - l_x = 2\lambda \\ \sqrt{-1} \cdot (-1)^p [1 \pm (-1)], & |m| - l_x = 2\lambda + 1 \end{cases}, \quad \lambda \in \mathbb{Z}. \quad (\text{A.8})$$

Following common conventions, we assign the positive linear combination to positive  $m$  values and the negative linear combination to negative  $m$  values. Including the factor  $\frac{1}{\sqrt{\pm 2}}$  from Eq. (A.4), we obtain

$m > 0$ :

$$\frac{1}{\sqrt{+2}} (\sigma_+ + \sigma_-) = \begin{cases} \sqrt{2} \cdot (-1)^p, & |m| - l_x = 2\lambda \\ 0, & |m| - l_x = 2\lambda - 1 \end{cases}, \quad \lambda \in \mathbb{Z}, \quad (\text{A.9})$$

$m < 0$ :

$$\frac{1}{\sqrt{-2}} (\sigma_+ - \sigma_-) = \begin{cases} 0, & |m| - l_x = 2\lambda \\ \sqrt{2} \cdot (-1)^p, & |m| - l_x = 2\lambda - 1 \end{cases}, \quad \lambda \in \mathbb{Z}. \quad (\text{A.10})$$

Summarized, if

$$(j = 2\mu + 1) \vee (m \geq 0 \wedge |m| - l_x = 2\lambda + 1) \\ \vee (m < 0 \wedge |m| - l_x = 2\lambda), \quad \mu, \lambda \in \mathbb{Z},$$

then

$$c(m, l_x, l_y, l_z) = 0, \quad (\text{A.11a})$$

else,

$$c(m, l_x, l_y, l_z) = \sqrt{\frac{(2l+1)(l-|m|)!}{4\pi(l+|m|)!}} \times \frac{1}{2^l l!} \sum_{i=0}^{(l-|m|)/2} \binom{l}{i} \binom{i}{j} \frac{(-1)^i (2l-2i)!}{(l-|m|-2i)!} \\ \times (-1)^p \sum_{k=0}^j (-1)^k \binom{j}{k} \binom{|m|}{l_x - 2k} \begin{cases} 1, & m = 0 \\ \sqrt{2}, & m \neq 0 \end{cases}, \quad (\text{A.11b})$$

where

$$l = l_x + l_y + l_z, \quad j = \frac{l_x + l_y - |m|}{2},$$

and

$$p = \begin{cases} \frac{(|m|-l_x)}{2}, & |m| - l_x = 2\lambda \\ \frac{(|m|-l_x-1)}{2}, & |m| - l_x = 2\lambda + 1 \end{cases}, \quad \lambda \in \mathbb{Z}.$$

For practical applications, these Cartesian coefficients can be evaluated once up to a given maximum order  $l$  and stored which is done by the “cartesian\_ylm” module in FHI-aims. It should be pointed out, however, that the implementation of real valued spherical harmonics in FHI-aims follows none (!) of the usual sign conventions.

## A.2 Cartesian Regular Solid Harmonics

With the knowledge of the Cartesian coefficients,  $c(m, l_x, l_y, l_z)$ , we can express the regular solid harmonics—as previously defined in Eq. (3.38a)—simply as

$$\mathcal{R}_m^l(x, y, z) = \sqrt{\frac{4\pi}{2l+1}} \sum_{l_x+l_y+l_z=l} c(m, l_x, l_y, l_z) x^{l_x} y^{l_y} z^{l_z}. \quad (\text{A.12})$$

### A.2.1 Gradient

Calculating the Cartesian gradient of the regular solid harmonics in the above expression is also straightforward,

$$\begin{aligned} \begin{pmatrix} \frac{\partial}{\partial x} \\ \frac{\partial}{\partial y} \\ \frac{\partial}{\partial z} \end{pmatrix} \mathcal{R}_m^l(x, y, z) &= \sqrt{\frac{4\pi}{2l+1}} \sum_{l_x+l_y+l_z=l} c(m, l_x, l_y, l_z) \begin{pmatrix} \frac{\partial}{\partial x} \\ \frac{\partial}{\partial y} \\ \frac{\partial}{\partial z} \end{pmatrix} x^{l_x} y^{l_y} z^{l_z} \\ &= \sqrt{\frac{4\pi}{2l+1}} \sum_{l_x+l_y+l_z=l} c(m, l_x, l_y, l_z) \begin{pmatrix} l_x \cdot x^{l_x-1} y^{l_y} z^{l_z} \\ l_y \cdot y^{l_y-1} x^{l_x} z^{l_z} \\ l_z \cdot z^{l_z-1} x^{l_x} y^{l_y} \end{pmatrix}. \end{aligned} \quad (\text{A.13})$$

### A.2.2 Scaled Function

For the use in the MPE model, the solid harmonics also need to be evaluated for a uniformly scaled coordinates—as presented in section 4.2.3. Given the positive real valued, scalar factor  $\gamma$ , we can easily factorize it out,

$$\begin{aligned} \mathcal{R}_m^l(\gamma x, \gamma y, \gamma z) &= \sqrt{\frac{4\pi}{2l+1}} \sum_{l_x+l_y+l_z=l} c(m, l_x, l_y, l_z) (\gamma x)^{l_x} (\gamma y)^{l_y} (\gamma z)^{l_z} \\ &= \sqrt{\frac{4\pi}{2l+1}} \sum_{l_x+l_y+l_z=l} c(m, l_x, l_y, l_z) \gamma^{l_x+l_y+l_z} x^{l_x} y^{l_y} z^{l_z} = \gamma^l \mathcal{R}_m^l(x, y, z). \end{aligned} \quad (\text{A.14})$$

### A.2.3 Gradient of Scaled Function

The gradient of the scaled function can be captured by the chain rule of derivation,

$$\begin{pmatrix} \frac{\partial}{\partial x} \\ \frac{\partial}{\partial y} \\ \frac{\partial}{\partial z} \end{pmatrix} \mathcal{R}_m^l(\gamma x, \gamma y, \gamma z) = \begin{pmatrix} \frac{\partial(\gamma x)}{\partial x} \frac{\partial}{\partial(\gamma x)} \\ \frac{\partial(\gamma y)}{\partial y} \frac{\partial}{\partial(\gamma y)} \\ \frac{\partial(\gamma z)}{\partial z} \frac{\partial}{\partial(\gamma z)} \end{pmatrix} \mathcal{R}_m^l(\gamma x, \gamma y, \gamma z) = \gamma \begin{pmatrix} \frac{\partial}{\partial(\gamma x)} \\ \frac{\partial}{\partial(\gamma y)} \\ \frac{\partial}{\partial(\gamma z)} \end{pmatrix} \mathcal{R}_m^l(\gamma x, \gamma y, \gamma z), \quad (\text{A.15})$$

and thereby transformed into the known form of the gradient of the unscaled regular harmonics, Eq. (A.13).

### A.3 Cartesian Irregular Solid Harmonics

Irregular solid harmonics, cf. Eq. (3.38b), can easily be calculated from the regular ones derived above,

$$\mathcal{I}_m^l(x, y, z) = r^{-2l-1} \mathcal{R}_m^l(x, y, z), \quad (\text{A.16})$$

with

$$r = \sqrt{x^2 + y^2 + z^2}. \quad (\text{A.17})$$

#### A.3.1 Gradient

Similarly, we also derive the irregular solid harmonics' gradient from the one of the regular solid harmonics,

$$\begin{pmatrix} \frac{\partial}{\partial x} \\ \frac{\partial}{\partial y} \\ \frac{\partial}{\partial z} \end{pmatrix} \mathcal{I}_m^l(x, y, z) = \begin{pmatrix} \frac{\partial}{\partial x} \\ \frac{\partial}{\partial y} \\ \frac{\partial}{\partial z} \end{pmatrix} r^{-2l-1} \mathcal{R}_m^l(x, y, z), \quad (\text{A.18})$$

through evaluation of the gradient of  $r^{-2l-1}$  which is symmetric in the coordinates and thus only evaluated for the  $x$  coordinate here,

$$\frac{\partial}{\partial x} (x^2 + y^2 + z^2)^{-l-\frac{1}{2}} = \left(-l - \frac{1}{2}\right) 2x (x^2 + y^2 + z^2)^{-l-\frac{3}{2}} = -(2l+1)r^{-2l-3}x. \quad (\text{A.19})$$

In summary, we find

$$\begin{pmatrix} \frac{\partial}{\partial x} \\ \frac{\partial}{\partial y} \\ \frac{\partial}{\partial z} \end{pmatrix} \mathcal{I}_m^l(x, y, z) = r^{-2l-1} \left[ \begin{pmatrix} \frac{\partial}{\partial x} \\ \frac{\partial}{\partial y} \\ \frac{\partial}{\partial z} \end{pmatrix} \mathcal{R}_m^l(x, y, z) - \frac{2l+1}{r^2} \begin{pmatrix} x \\ y \\ z \end{pmatrix} \mathcal{R}_m^l(x, y, z) \right], \quad (\text{A.20})$$

where the regular solid harmonic functions and their gradient is known, cf. Eqs. (A.12) and (A.13).

#### A.3.2 Scaled Function

Using Eq. (A.14), the uniform scaling of the irregular solid harmonics can be expressed as

$$\begin{aligned} \mathcal{I}_m^l(\gamma x, \gamma y, \gamma z) &= (\gamma r)^{-2l-1} \mathcal{R}_m^l(\gamma x, \gamma y, \gamma z) = (\gamma r)^{-2l-1} \gamma^l \mathcal{R}_m^l(x, y, z) \\ &= \gamma^{-l-1} r^{-2l-1} \mathcal{R}_m^l(x, y, z) = \gamma^{-l-1} \mathcal{I}_m^l(x, y, z). \end{aligned} \quad (\text{A.21})$$

### A.3.3 Gradient of Scaled Function

Finally, the derivative of the scaled functions is again transformed *via* the chain rule of derivation,

$$\begin{pmatrix} \frac{\partial}{\partial x} \\ \frac{\partial}{\partial y} \\ \frac{\partial}{\partial z} \end{pmatrix} \mathcal{I}_m^l(\gamma x, \gamma y, \gamma z) = \gamma \begin{pmatrix} \frac{\partial}{\partial(\gamma x)} \\ \frac{\partial}{\partial(\gamma y)} \\ \frac{\partial}{\partial(\gamma z)} \end{pmatrix} \mathcal{I}_m^l(\gamma x, \gamma y, \gamma z) \quad (\text{A.22})$$

and using the formula of the unscaled gradient, Eq. (A.20). In summary, one finds

$$\begin{pmatrix} \frac{\partial}{\partial x} \\ \frac{\partial}{\partial y} \\ \frac{\partial}{\partial z} \end{pmatrix} \mathcal{I}_m^l(\gamma x, \gamma y, \gamma z) = (\gamma r)^{-2l-1} \left[ \gamma \begin{pmatrix} \frac{\partial}{\partial(\gamma x)} \\ \frac{\partial}{\partial(\gamma y)} \\ \frac{\partial}{\partial(\gamma z)} \end{pmatrix} \mathcal{R}_m^l(\gamma x, \gamma y, \gamma z) - \gamma \frac{2l+1}{(\gamma r)^2} \begin{pmatrix} \gamma x \\ \gamma y \\ \gamma z \end{pmatrix} \mathcal{R}_m^l(\gamma x, \gamma y, \gamma z) \right]. \quad (\text{A.23})$$

# ***B Solving the Generalized Poisson Equation Using Finite Elements*** ‡

---

## ***B.1 Generalized Poisson Equation in Cylindrical Coordinates***

For performance reasons we restrict ourselves here to systems of axial symmetry and thus use cylindrical coordinates denoted as  $(\rho, \zeta)$ , where any dependency on the rotation angle  $\varphi$  is dropped due to symmetry. In order to check for finite size errors within the same simulation box, a scaled coordinate system  $(r, z)$  is introduced,

$$\rho = l_r r, \quad (\text{B.1a})$$

$$\zeta = l_z z, \quad (\text{B.1b})$$

with corresponding scaling factors  $l_r$  and  $l_z$ . The scalar field gradient in these coordinates reads

$$\nabla = \frac{1}{l_r} \frac{\partial}{\partial r} \hat{\mathbf{r}} + \frac{1}{l_z} \frac{\partial}{\partial z} \hat{\mathbf{z}}. \quad (\text{B.2})$$

The divergence of a vector field  $\mathbf{U}$  is given by

$$\nabla \cdot \mathbf{U} = \frac{1}{l_r} \frac{\partial(r\mathbf{U} \cdot \hat{\mathbf{r}})}{\partial r} + \frac{1}{l_z} \frac{\partial(\mathbf{U} \cdot \hat{\mathbf{z}})}{\partial z}. \quad (\text{B.3})$$

Using Eqs. (B.2) and (B.3), we can express Eq. (3.15) in coordinates of  $(r, z)$ ,

$$\frac{\partial}{\partial r} \left( \frac{r\varepsilon(l_r r, l_z z)}{l_r^2} \frac{\partial \Phi}{\partial r} \right) + \frac{\partial}{\partial z} \left( \frac{r\varepsilon(l_r r, l_z z)}{l_z^2} \frac{\partial \Phi}{\partial z} \right) = -4\pi \cdot r\rho(l_r r, l_z z). \quad (\text{B.4})$$

In the following, we will first find an expression for the relative dielectric function  $\varepsilon(\rho, \zeta)$ . Thereafter, Eq. (B.4) will be revisited and further simplified.

## ***B.2 Spherical Cavity and Smoothing of Dielectric Function***

For the sake of simplicity, the spherical cavity of radius  $r_c$  in the model case studied here is centered at the origin of the coordinate system. Analogously to Eq. (3.20), it is defined by the function  $\mathcal{C}(\rho, \zeta)$  which is negative inside of the cavity and positive outside. An appropriate form for this

---

‡Reprinted in parts with permission from Ref. [2]. © 2017 American Chemical Society.

function is

$$\mathcal{C}(\rho, \zeta) = \sqrt{\rho^2 + \zeta^2} - r_c . \quad (\text{B.5})$$

For the MPE model, the dielectric function is directly given by Eq. (3.20) with the function  $\mathcal{C}(\rho, \zeta)$  defined above,

$$\varepsilon_{\text{MPE}}(\rho, \zeta) = \varepsilon_b \Theta [\mathcal{C}(\rho, \zeta)] + \left( 1 - \Theta [\mathcal{C}(\rho, \zeta)] \right) , \quad (\text{B.6})$$

where the relative dielectric permittivity is constant inside,  $\varepsilon_{\text{MPE}} = 1$ , and outside,  $\varepsilon_{\text{MPE}} = \varepsilon_b$ , of the cavity.

The Heaviside step function  $\Theta$  in Eq. (B.6), however, is numerically problematic in the FEM approach. Thus, we introduce a (one-dimensional) smooth switching function  $\Lambda$  with the generic form of

$$\Lambda_a(\sigma) = \begin{cases} 0, & \sigma < -a \\ 0.5 + 0.75 \frac{\sigma}{a} - 0.25 \left( \frac{\sigma}{a} \right)^3, & \sigma \in [-a, a] \\ 1, & \sigma > a \end{cases} , \quad (\text{B.7})$$

and the derivative

$$\frac{d\Lambda_a}{d\sigma} = \begin{cases} \frac{0.75}{a} \left[ 1 - \left( \frac{\sigma}{a} \right)^2 \right], & \sigma \in [-a, a] \\ 0, & \text{else} \end{cases} , \quad (\text{B.8})$$

with the real positive parameter  $a$  that defines the width of the switching region. This function switches smoothly from  $\Lambda_a(-a) = 0$  to  $\Lambda_a(a) = 1$  and its derivative is continuous at the domain boundaries.

Replacing the step function  $\Theta$  in Eq. (B.6) by  $\Lambda$ , a corresponding smooth dielectric function suitable for the finite element solver is obtained,

$$\varepsilon_{\text{FEM}}(\rho, \zeta; a) = \varepsilon_b \Lambda_a [\mathcal{C}(\rho, \zeta)] + \left( 1 - \Lambda_a [\mathcal{C}(\rho, \zeta)] \right) . \quad (\text{B.9})$$

The two dielectric functions are exactly the same when the width of the smooth switching region goes to zero, i.e.

$$\varepsilon_{\text{MPE}}(\rho, \zeta) = \lim_{a \rightarrow 0} \varepsilon_{\text{FEM}}(\rho, \zeta; a) . \quad (\text{B.10})$$

Of course,  $a$  needs to be greater than zero in order to obtain the desired smoothness of the dielectric function. Thus, Eq. (B.9) and Eq. (B.6) are not identical which causes an intrinsic discrepancy between the MPE and FEM results. The adaptivity of the integration grid used in KARDOS, however, allows for an efficient way of minimizing this error. Starting the calculations with a relatively broad switching region and then gradually narrowing it down leads to a very refined integration grid at the cavity surface whereas the rest of the domain can be sampled on a much coarser level. The parameter  $a$  is then reduced until convergence of the FEM result is observed.

### B.2.1 Gradient

As can be seen later on in Eq. (B.24), not the dielectric function but its gradient is needed. With  $\varepsilon_{\text{FEM}}$  being symmetric with respect to the coordinates  $\rho$  and  $\zeta$ , cf. Eq. (B.9), we will only show the derivation of one term,

$$\begin{aligned} \frac{\partial \varepsilon_{\text{FEM}}}{\partial \rho} &= \frac{\partial \varepsilon_{\text{FEM}}}{\partial \Lambda_a} \cdot \frac{\partial \Lambda_a}{\partial \mathcal{C}} \cdot \frac{\partial \mathcal{C}}{\partial \rho} \\ &= (\varepsilon_b - 1) \cdot \frac{\partial \Lambda_a}{\partial \mathcal{C}} \cdot \frac{\rho}{\sqrt{\rho^2 + \zeta^2}}. \end{aligned} \quad (\text{B.11})$$

The remaining derivative is simply the one shown in Eq. (B.8), thus

$$\nabla_{\varepsilon_{\text{FEM}}}(\rho, \zeta) = \frac{\varepsilon_b - 1}{\sqrt{\rho^2 + \zeta^2}} \cdot \frac{\partial \Lambda_a}{\partial \mathcal{C}} \cdot \begin{pmatrix} \rho \\ \zeta \end{pmatrix}. \quad (\text{B.12})$$

### B.2.2 Outlook: Interface Between Two Dielectrics

As presented in the first part of chapter 7, we assume a planar interface between the two dielectric media. Due to the symmetry of the employed coordinate system, it is natural that this plane  $\mathbb{L}$  is perpendicular to the rotation axis. We define it *via* its (signed) distance  $\zeta_0$  to the origin,

$$L : \zeta = \zeta_0. \quad (\text{B.13})$$

Similar to the cavity function  $\mathcal{C}$ , the interface function  $\mathcal{L}$ , cf. Eq. (7.2) is positive for a point in the upper dielectric medium ( $\zeta > \zeta_0$ ) with a permittivity  $\varepsilon_{\text{b,u}}$  and negative in the lower one with  $\varepsilon_{\text{b,l}}$ . The dielectric function is then expressed in terms of the switching function  $\Lambda$  defined above,

$$\varepsilon_{\text{FEM}}^L(\rho, \zeta; a') = \varepsilon_{\text{b,l}} + (\varepsilon_{\text{b,u}} - \varepsilon_{\text{b,l}}) \Lambda_{a'} \left[ \mathcal{L}(\rho, \zeta) \right], \quad (\text{B.14})$$

where  $a'$  is the width of the switching region.

The gradient of this function is 0 in  $\rho$  and takes the following form in  $\zeta$ ,

$$\frac{\partial \varepsilon_{\text{FEM}}^L}{\partial \zeta} = \frac{\partial \varepsilon_{\text{FEM}}^L}{\partial \Lambda_{a'}} \cdot \frac{\partial \Lambda_{a'}}{\partial \mathcal{L}} \cdot \frac{\partial \mathcal{L}}{\partial \zeta} = (\varepsilon_{\text{b,u}} - \varepsilon_{\text{b,l}}) \frac{\partial \Lambda_{a'}}{\partial \mathcal{L}}, \quad (\text{B.15})$$

where the unresolved gradient is again simply given by Eq. (B.8).

In order to describe the problem of a charge distribution within a spherical cavity at a dielectric interface, one needs to combine the two approaches. The full dielectric function is then

$$\varepsilon_{\text{FEM}}^{\mathcal{C},L}(\rho, \zeta; a, a') = 1 + \Lambda_a \left[ \mathcal{C}(\rho, \zeta) \right] \left( \varepsilon_{\text{b,l}} - 1 + (\varepsilon_{\text{b,u}} - \varepsilon_{\text{b,l}}) \Lambda_{a'} \left[ \mathcal{L}(\rho, \zeta) \right] \right). \quad (\text{B.16})$$



Its derivative with respect to  $\zeta$  is

$$\begin{aligned}\frac{\partial \varepsilon_{\text{FEM}}^{C,L}}{\partial \rho} &= \frac{\partial \varepsilon_{\text{FEM}}^{C,L}}{\partial \Lambda_a} \cdot \frac{\partial \Lambda_a}{\partial \mathcal{C}} \cdot \frac{\partial \mathcal{C}}{\partial \rho} \\ &= \left( \varepsilon_{b,l} - 1 + (\varepsilon_{b,u} - \varepsilon_{b,l}) \Lambda_{a'} \left[ \mathcal{L}(\rho, \zeta) \right] \right) \cdot \frac{\partial \Lambda_a}{\partial \mathcal{C}} \cdot \frac{\rho}{\sqrt{\rho^2 + \zeta^2}},\end{aligned}\quad (\text{B.17a})$$

whereas in the one with respect to  $\zeta$ , the derivative of  $\mathcal{L}$  also needs to be included,

$$\begin{aligned}\frac{\partial \varepsilon_{\text{FEM}}^{C,L}}{\partial \zeta} &= \frac{\partial \varepsilon_{\text{FEM}}^{C,L}}{\partial \Lambda_a} \cdot \frac{\partial \Lambda_a}{\partial \mathcal{C}} \cdot \frac{\partial \mathcal{C}}{\partial \zeta} + \frac{\partial \varepsilon_{\text{FEM}}^{C,L}}{\partial \Lambda_{a'}} \cdot \frac{\partial \Lambda_{a'}}{\partial \mathcal{L}} \cdot \frac{\partial \mathcal{L}}{\partial \zeta} \\ &= \left( \varepsilon_{b,l} - 1 + (\varepsilon_{b,u} - \varepsilon_{b,l}) \Lambda_{a'} \left[ \mathcal{L}(\rho, \zeta) \right] \right) \cdot \frac{\partial \Lambda_a}{\partial \mathcal{C}} \cdot \frac{\zeta}{\sqrt{\rho^2 + \zeta^2}} \\ &\quad + (\varepsilon_{b,u} - \varepsilon_{b,l}) \Lambda_a \left[ \mathcal{C}(\rho, \zeta) \right] \cdot \frac{\partial \Lambda_{a'}}{\partial \mathcal{L}}.\end{aligned}\quad (\text{B.17b})$$

In the above expressions, Eqs. (B.16), (B.17a) and (B.17b), also the simpler cases discussed before are included.

- The absence of a cavity can simply be simulated by picking a negative radius such that the switching function  $\Lambda_a \left[ \mathcal{C}(\rho, \zeta) \right]$  always assumes a value of 1, i.e.

$$r_c \leq -a.$$

- When both dielectric media have the same permittivity, i.e.

$$\varepsilon_{b,u} = \varepsilon_{b,l},$$

all terms introduced for the dielectric interface exactly cancel out and the previously derived equations for the solvation cavity in a homogeneous dielectric environment are recovered.

### B.3 Regularization of the Potential

In the model systems studied here, the source term  $\varrho$  in the generalized Poisson equation, cf. Eq. (B.4), consists of one or several electric poles  $p_i$  (monopole, dipole, etc.) located at positions  $\mathbf{r}_i = (\rho_i, \zeta_i)$ ,

$$\varrho(\mathbf{r}) = \sum_i p_i \delta(\mathbf{r} - \mathbf{r}_i). \quad (\text{B.18})$$

Regularization of Eq. (B.4) with a source term  $\varrho_0$  for which we know the solution  $\Phi_0$  to Poisson's equation,

$$\Delta \Phi_0 = -4\pi \varrho_0, \quad (\text{B.19})$$

serves to cure the numerical problems in the finite element method connected with the  $\delta$  function in the source term, Eq. (B.18), and the resulting pole in the potential. This is done by splitting the

full potential in two contributions,  $\Phi_0$  and  $\Phi'$ ,

$$\Phi = \Phi_0 + \Phi'. \quad (\text{B.20})$$

The linearity of Poisson's equation and the relation

$$\nabla \cdot (\tau \mathbf{U}) = \mathbf{U} \cdot \nabla \tau + \tau \nabla \cdot \mathbf{U}, \quad (\text{B.21})$$

allow us to rewrite Eq. (3.15) in the following way,

$$\nabla \cdot (\varepsilon \nabla \Phi') + (\nabla \Phi_0) \cdot (\nabla \varepsilon) + \varepsilon \Delta \Phi_0 + 4\pi \varrho = 0. \quad (\text{B.22})$$

When we assume that all of the (classical) electric poles are located within the cavity where the dielectric function is exactly 1, inserting Eq. (B.19) into Eq. (B.22) reveals that a good choice for the regularization source  $\varrho_0$  is simply

$$\varrho_0 = \varrho. \quad (\text{B.23})$$

This way, the last two terms on the left-hand side of Eq. (B.22) cancel and we arrive at a tailored equation for our model systems,

$$\nabla \cdot (\varepsilon \nabla \Phi') - \mathbf{E}_0 \cdot \nabla \varepsilon = 0. \quad (\text{B.24})$$

The regularization scheme used here is identical to the one used for the ASC models, cf. section 3.3.2. Here, however, the source terms are classical point charges or higher electrostatic poles without spatial extent. Thus, it is straightforward to restrict the source to the cavity's interior region and the previously discussed outlying charge problem of the ASC methods as such does not exist in this case. The regularization method of the MPE model, on the other hand, is slightly different—cf. Eq. (3.41) and note the scaling of the Hartree potential. Thus,  $\Phi'$  cannot directly be compared to  $\Phi_\delta$  but to the slightly modified

$$\Phi'_\delta = \Phi_\delta + (\varepsilon_b^{-1} - 1) \Phi_H. \quad (\text{B.25})$$

### ***B.3.1 Analytical Expressions for Point Multipoles***

In order to efficiently evaluate Eq. (B.24), it is vital to derive an analytical expression for  $\mathbf{E}_0 = -\nabla \Phi_0$ , i.e., the electrostatic potential of the charge distribution  $\varrho_0$  in vacuum (cf. Eq. (B.18)). According to the superposition principle, the contributions of different electric poles  $p_i$  to  $\mathbf{E}_0$  can thereby be treated independently. In the following, we will derive expressions for  $\mathbf{E}_0$  only—but without loss of generality—up to a quadrupolar moment, i.e.  $l \leq 2$ . It should be noted here that the potential (and electrostatic field) of these point multipoles can, of course, be represented by (irregular) solid harmonic functions, cf. Eq. (3.38b). Due to the rotational symmetry around the  $\zeta$ -axis in the coordinate system  $(\rho, \zeta)$  introduced above, however, only solid harmonics with a quantum number  $m = 0$  can contribute which reduces the problem to finding the expansion coefficients  $M^{(l,0)}$ .

### **Monopole**

The electrostatic potential of a point charge  $M^{(0,0)}$  at the origin of the coordinate system in vacuum is given by

$$\Phi_0 = M^{(0,0)} \frac{1}{\sqrt{\rho^2 + \zeta^2}}, \quad (\text{B.26})$$

and the electric field is simply

$$\mathbf{E}_0 = -\nabla\Phi_0 = M^{(0,0)} c^{(0)} \begin{pmatrix} \rho \\ \zeta \end{pmatrix}, \quad c^{(0)} = (\rho^2 + \zeta^2)^{-\frac{3}{2}}. \quad (\text{B.27})$$

### **Dipole**

The electrostatic potential of a point dipole of magnitude  $M^{(1,0)}$  at the origin of the coordinate system is

$$\Phi_0 = M^{(1,0)} \frac{\zeta}{\left(\sqrt{\rho^2 + \zeta^2}\right)^3}, \quad (\text{B.28})$$

and thus

$$\mathbf{E}_0 = M^{(1,0)} c_1^{(1)} \begin{pmatrix} c_2^{(1)} \rho \\ c_2^{(1)} \zeta - 1 \end{pmatrix}, \quad c_1^{(1)} = (\rho^2 + \zeta^2)^{-\frac{3}{2}}, \quad c_2^{(1)} = \frac{3\zeta}{\rho^2 + \zeta^2}. \quad (\text{B.29})$$

### **Quadrupole**

The electrostatic potential of a point quadrupole of magnitude  $M^{(2,0)}$  at the origin of the coordinate system is

$$\Phi_0 = M^{(2,0)} \frac{\zeta^2 - \frac{1}{2}\rho^2}{\left(\sqrt{\rho^2 + \zeta^2}\right)^5}. \quad (\text{B.30})$$

Again, we can calculate the field *via*

$$-\frac{\partial\Phi_0}{\partial\rho} = -\frac{\partial(\rho^2)}{\partial\rho} \cdot \frac{\partial\Phi_0}{\partial(\rho^2)} = \rho \cdot M^{(2,0)} \left( \frac{1}{\left(\sqrt{\rho^2 + \zeta^2}\right)^5} + 5 \frac{\zeta^2 - \frac{1}{2}\rho^2}{\left(\sqrt{\rho^2 + \zeta^2}\right)^7} \right), \quad (\text{B.31})$$

and

$$-\frac{\partial\Phi_0}{\partial\zeta} = -\frac{\partial(\zeta^2)}{\partial\zeta} \cdot \frac{\partial\Phi_0}{\partial(\zeta^2)} = \zeta \cdot M^{(2,0)} \left( \frac{-2}{\left(\sqrt{\rho^2 + \zeta^2}\right)^5} + 5 \frac{\zeta^2 - \frac{1}{2}\rho^2}{\left(\sqrt{\rho^2 + \zeta^2}\right)^7} \right), \quad (\text{B.32})$$

to obtain the final result,

$$\mathbf{E}_0 = M^{(2,0)} c_1^{(2)} \begin{pmatrix} (c_2^{(2)} + 1) \rho \\ (c_2^{(2)} - 2) \zeta \end{pmatrix}, \quad c_1^{(2)} = (\rho^2 + \zeta^2)^{-\frac{5}{2}}, \quad c_2^{(2)} = 5 \frac{\zeta^2 - \frac{1}{2} \rho^2}{\rho^2 + \zeta^2}. \quad (\text{B.33})$$

## B.4 Integration Weights on Triangular Grid

The adaptive sparse triangular grid created by the finite element solver consists of non-overlapping triangles defined by the function  $t(i, j, k)$

$$t(i, j, k) = \begin{cases} 1, & \mathbf{r}_i, \mathbf{r}_j, \mathbf{r}_k \text{ form a triangle} \\ 0, & \text{otherwise} \end{cases} \quad (\text{B.34})$$

where  $\mathbf{r}_i, \mathbf{r}_j, \mathbf{r}_k$  are points on the integration grid. This triangulation information is used to assign an area element  $dA_i$  in cylindrical coordinates to each integration grid point  $\mathbf{r}_i$  with coordinates  $(\rho_i \ \zeta_i)^T$  equal to one third of the area of all triangles it contributes to form

$$dA_i = \sum_{j,k} \frac{1}{6} \left\| (\mathbf{r}_j - \mathbf{r}_i) \times (\mathbf{r}_k - \mathbf{r}_i) \right\|_2 \quad (\text{B.35})$$

The three-dimensional volume element  $dV_i$  in cylindrical coordinates is then simply

$$dV_i = 2\pi \rho_i dA_i \quad (\text{B.36})$$

## B.5 Computational Details for the Finite Element Solver

In all FEM calculations, we consider a rectangular domain with  $r \in [0, 1]$  and  $z \in [-1, 1]$  employing the scaling factors  $l_r = l_z = 50$ . We impose Dirichlet boundary conditions except for the symmetry axis where Neumann boundary conditions are used. The Dirichlet boundary values for monopole terms used in the regularization of the potential for the FEM are calculated analytically while the higher order terms (dipoles and quadrupoles) are assumed to be zero.

We employ an initial mesh of  $5 \times 9$  equidistant regular grid points and linear finite elements. The adaptive refinement is controlled with a hierarchical basis error estimator [3] for which we choose a tolerance of  $1 \times 10^{-6} E_h e^{-1}$ . We restrict the refinement procedure such that the grid gets at most 12 times refined and we do not exceed 5000000 grid points in total. This results in an effective spatial resolution of  $3 \times 10^{-3} a_0$  and estimated errors below  $1 \times 10^{-4} E_h e^{-1}$ .

The initial grid is too coarse to resolve the cavity. We therefore start with a broad smoothing function  $\Lambda$  with  $a = 1$  to solve this problem. We then reduce  $a$  stepwise to the targeted value of 0.01, always employing the resulting mesh and solution of the previous step as initial guess.



## C Derivations Related to the Isodensity Cavity ‡

---

### C.1 Calculation of the Intersection Point of Two Lines in 2D

In order to determine the intersection point  $\tilde{\mathbf{z}}_{ij}$  of two lines (cf. Eqs. (5.37) and (5.38)),

$$\tilde{l}_i : \quad \tilde{\mathbf{I}}(\lambda_i) = \frac{1}{2}\tilde{\mathbf{q}}_i + \lambda_i\tilde{\mathbf{v}}_i = \frac{1}{2}\begin{pmatrix} \tilde{q}_{i,1} \\ \tilde{q}_{i,2} \end{pmatrix} + \lambda_i\begin{pmatrix} -\tilde{q}_{i,2} \\ \tilde{q}_{i,1} \end{pmatrix}, \quad (\text{C.1a})$$

and

$$\tilde{l}_j : \quad \tilde{\mathbf{I}}(\lambda_j) = \frac{1}{2}\tilde{\mathbf{q}}_j + \lambda_j\tilde{\mathbf{v}}_j = \frac{1}{2}\begin{pmatrix} \tilde{q}_{j,1} \\ \tilde{q}_{j,2} \end{pmatrix} + \lambda_j\begin{pmatrix} -\tilde{q}_{j,2} \\ \tilde{q}_{j,1} \end{pmatrix}, \quad (\text{C.1b})$$

with given point vectors  $\tilde{\mathbf{q}}_{i/j}$  and non-collinear direction vectors  $\tilde{\mathbf{v}}_{i/j}$ , we have to solve the equation

$$\tilde{\mathbf{I}}(\lambda_i) = \tilde{\mathbf{I}}(\lambda_j) \quad (\text{C.2})$$

which leads to the following system of equations:

$$\frac{1}{2}\tilde{q}_{i,1} - \lambda_i\tilde{q}_{i,2} = \frac{1}{2}\tilde{q}_{j,1} - \lambda_j\tilde{q}_{j,2}, \quad (\text{C.3a})$$

$$\frac{1}{2}\tilde{q}_{i,2} + \lambda_i\tilde{q}_{i,1} = \frac{1}{2}\tilde{q}_{j,2} + \lambda_j\tilde{q}_{j,1}. \quad (\text{C.3b})$$

Note here, that only the solution to either  $\lambda_i$  or  $\lambda_j$  is required to determine the intersection point *via* Eq. (C.1a) or Eq. (C.1b), respectively.

Without loss of generality—as we will see later on—we can assume that  $\tilde{q}_{j,1} \neq 0$ . This allows us to express  $\lambda_j$  in terms of  $\lambda_i$  using Eq. (C.3b),

$$\lambda_j = \lambda_i \frac{\tilde{q}_{i,1}}{\tilde{q}_{j,1}} + \frac{1}{2} \frac{\tilde{q}_{i,2} - \tilde{q}_{j,2}}{\tilde{q}_{j,1}}. \quad (\text{C.4})$$

Inserting Eq. (C.4) into Eq. (C.3a) and solving for  $\lambda_i$  yields

$$\lambda_i = \frac{1}{2} \frac{\tilde{q}_{j,2}(\tilde{q}_{j,2} - \tilde{q}_{i,2}) + \tilde{q}_{j,1}(\tilde{q}_{j,1} - \tilde{q}_{i,1})}{\tilde{q}_{i,1}\tilde{q}_{j,2} - \tilde{q}_{j,1}\tilde{q}_{i,2}}. \quad (\text{C.5})$$

Note that the absolute value of the denominator is simply the area of a parallelogram spanned

---

‡Reprinted in parts with permission from Ref. [2]. © 2017 American Chemical Society.

by  $\tilde{\mathbf{v}}_i$  and  $\tilde{\mathbf{v}}_j$  which is only zero if the two lines are collinear—a case which we have excluded beforehand. The solution in the case of  $\tilde{q}_{j,1} = 0$  is also covered in the expression of Eq. (C.5) which can easily be verified by inserting  $\tilde{q}_{j,1} = 0$  into Eq. (C.3b) and solving for  $\lambda_i$ .

The general expression for the intersection point  $\tilde{\mathbf{z}}_{ij}$  in Eq. (5.39) is obtained by inserting Eq. (C.5) into Eq. (C.1a).

## C.2 Distance Scaling for Density-Walkers

The distance scaling factor is derived from the following considerations: Given two points  $i$  and  $j$  on a circle, the ratio of the length of the arc,  $s_{ij}^{\text{arc}}$ , and a straight line,  $s_{ij}^{\text{line}}$ , between them is given by

$$\frac{s_{ij}^{\text{arc}}}{s_{ij}^{\text{line}}} = \frac{\frac{\theta_{ij}}{2}}{\sin(\frac{\theta_{ij}}{2})}, \quad (\text{C.6})$$

where  $\theta_{ij}$  is the angle between the two position vectors. Squaring Eq. (C.6) and using a trigonometric half angle formula, we straightforwardly obtain the following relation:

$$\left(\frac{s_{ij}^{\text{arc}}}{s_{ij}^{\text{line}}}\right)^2 = \frac{\theta_{ij}^2}{2(1 - \cos \theta_{ij})}. \quad (\text{C.7})$$

Since  $\cos \theta_{ij}$  can easily be calculated from the normal vectors on those points, cf. Eq. (5.27), we express  $\theta_{ij}^2$  as a function of  $\cos \theta_{ij}$ ,

$$\theta_{ij}^2 = \left(\arccos(\cos \theta_{ij})\right)^2, \quad (\text{C.8})$$

and expand this function in a Taylor series at  $\cos \theta_{ij} = 1$ , i.e. for small angles  $\theta$ ,

$$\theta_{ij}^2 = 2(1 - \cos \theta_{ij}) + \frac{(1 - \cos \theta_{ij})^2}{3} + \frac{(1 - \cos \theta_{ij})^3}{11.25} + \mathcal{O}\left((1 - \cos \theta_{ij})^4\right). \quad (\text{C.9})$$

Truncating this series at third order, we obtain the following distance ratio,

$$\frac{s_{ij}^{\text{arc}}}{s_{ij}^{\text{line}}} = \sqrt{1 + \frac{(1 - \cos \theta_{ij})^2}{6} + \frac{(1 - \cos \theta_{ij})^3}{22.5}}, \quad (\text{C.10})$$

which is equal to the employed scaling factor.

### C.3 Surface Area Curvature Correction Factor

The correction factor is derived from the surface area ratio of a spherical cap versus a flat circle of same segment radius,

$$\frac{O_{\text{cap}}}{O_{\text{circle}}} = \frac{2\pi Rh}{\pi a^2} = 1 + \frac{h^2}{a^2}, \quad (\text{C.11})$$

where  $R$  is the radius of the sphere,  $a$  the segment radius, and  $h$  the height of the cap. Using Pythagoras' theorem,

$$(R - h)^2 + a^2 = R^2, \quad (\text{C.12})$$

and the cosine of the opening angle  $\theta$ ,

$$\cos \theta = \frac{R - h}{h}, \quad (\text{C.13})$$

one obtains

$$\frac{a^2}{h^2} = \frac{1 + \cos \theta}{1 - \cos \theta}. \quad (\text{C.14})$$

This is inserted into Eq. (C.11),

$$\frac{O_{\text{cap}}}{O_{\text{circle}}} = \frac{2}{1 + \cos \theta}. \quad (\text{C.15})$$

We calculate an approximation for  $\cos(2\theta)$  from the average projection of the normal vectors on the involved neighbors,  $\mathbf{q}_{i_1}$  to  $\mathbf{q}_{i_4}$ , onto the normal vector on point  $\mathbf{p}$ ,

$$\cos(2\theta) \approx \mathbf{n}_{\mathbf{p}} \cdot \frac{1}{4} \sum_{k=1}^4 \mathbf{n}_{\mathbf{q}_{i_k}}, \quad (\text{C.16})$$

and use a trigonometric half angle formula to obtain Eq. (5.42).





## ***D Tables of Optimized Parameter Sets*** ‡

---

The parametrization results for neutral and cationic solutes are summarized in Tab. D.1 whereas the ones involving anionic solutes are shown in Tab. D.2. In all cases presented here, the solvation cavity is created from the converged vacuum density and fixed throughout the SCF cycle.

---

‡Reprinted in parts with permission from Ref. [2]. © 2017 American Chemical Society.

Tab. D.1: Parameter Optimization Results For Neutral and Cationic Molecules Only<sup>a</sup>

| xc <sup>b</sup> | set. <sup>c</sup> | $\varrho_{\text{iso}}$<br>(me Å <sup>-3</sup> ) | $\alpha$<br>(meV Å <sup>-2</sup> ) | $\beta$<br>(meV Å <sup>-3</sup> ) | MAE <sup>d</sup><br>(meV) | $\varrho_{\text{iso}}$<br>(me Å <sup>-3</sup> ) | $\alpha$<br>(meV Å <sup>-2</sup> ) | $\beta$<br>(meV Å <sup>-3</sup> ) | MAE <sup>d</sup><br>(meV) |
|-----------------|-------------------|---|------------------------------------|-----------------------------------|---------------------------|---|------------------------------------|-----------------------------------|---------------------------|
|                 |                   | T1 (240 solutes)                                |                                    |                                   |                           | T2 (274 solutes)                                |                                    |                                   |                           |
| PBE             | l                 | 13.5  | 4.56                               | -3.98                             | 47.2                      | 14.6  | 3.63                               | -2.78                             | 42.8                      |
| PBE             | l                 | 11.0  | 0.869                              | 0                                 | 53.6                      | 12.8  | 0.999                              | 0                                 | 48.7                      |
| PBE             | t                 | 15.4  | 5.58                               | -5.24                             | 46.5                      | 16.3  | 4.08                               | -3.35                             | 41.9                      |
| PBE             | t                 | 12.0  | 0.815                              | 0                                 | 56.3                      | 14.2  | 0.989                              | 0                                 | 49.8                      |
| PBE             | rt                | 15.6  | 5.76                               | -5.42                             | 46.3                      | 16.5  | 4.28                               | -3.56                             | 41.6                      |
| PBE             | rt                | 12.0  | 0.818                              | 0                                 | 56.3                      | 14.1  | 0.989                              | 0                                 | 49.9                      |
| RPBE            | t                 | 15.7  | 5.70                               | -5.42                             | 47.5                      | 16.6  | 4.08                               | -3.36                             | 43.3                      |
| RPBE            | t                 | 12.1  | 0.798                              | 0                                 | 57.9                      | 14.4  | 0.999                              | 0                                 | 51.0                      |
| PBE0            | t                 | 12.5  | 4.81                               | -4.40                             | 48.9                      | 14.1  | 3.77                               | -3.04                             | 42.8                      |
| PBE0            | t                 | 10.0  | 0.744                              | 0                                 | 56.8                      | 12.2  | 0.920                              | 0                                 | 50.2                      |
| HSE06           | t                 | 12.5  | 4.83                               | -4.42                             | 48.9                      | 14.1  | 3.76                               | -3.04                             | 42.9                      |
| HSE06           | t                 | 10.0  | 0.733                              | 0                                 | 57.0                      | 12.2  | 0.908                              | 0                                 | 50.3                      |
|                 |                   | T2+T3 (326 solutes)                             |                                    |                                   |                           | T2+T3c (326 solutes)                            |                                    |                                   |                           |
| PBE             | l                 | 12.4  | 2.73                               | -1.97                             | 54.9                      | 11.6  | 2.65                               | -1.97                             | 50.7                      |
| PBE             | l                 | 11.9  | 0.908                              | 0                                 | 58.9                      | 11.2  | 0.818                              | 0                                 | 54.7                      |
| PBE             | t                 | 12.5  | 2.80                               | -2.23                             | 55.4                      | 11.8  | 2.70                               | -2.18                             | 51.8                      |
| PBE             | t                 | 12.0  | 0.761                              | 0                                 | 60.3                      | 11.4  | 0.692                              | 0                                 | 56.4                      |
| PBE             | rt                | 12.3  | 2.79                               | -2.23                             | 55.6                      | 11.7  | 2.68                               | -2.17                             | 52.1                      |
| PBE             | rt                | 11.8  | 0.746                              | 0                                 | 60.4                      | 11.2  | 0.675                              | 0                                 | 56.6                      |
| RPBE            | t                 | 12.2  | 2.65                               | -2.11                             | 57.2                      | 11.6  | 2.53                               | -2.03                             | 53.4                      |
| RPBE            | t                 | 11.8  | 0.732                              | 0                                 | 61.4                      | 11.2  | 0.654                              | 0                                 | 57.5                      |
| PBE0            | t                 | 12.1  | 2.88                               | -2.21                             | 54.7                      | 11.4  | 2.75                               | -2.14                             | 51.4                      |
| PBE0            | t                 | 11.6  | 0.848                              | 0                                 | 59.9                      | 11.0  | 0.778                              | 0                                 | 56.2                      |
| HSE06           | t                 | 12.1  | 2.91                               | -2.25                             | 54.6                      | 11.5  | 2.77                               | -2.17                             | 51.3                      |
| HSE06           | t                 | 11.7  | 0.851                              | 0                                 | 60.0                      | 11.0  | 0.772                              | 0                                 | 56.3                      |

<sup>a</sup> For all computational settings, two parameter sets are given: one with a volume-dependent non-electrostatic contribution (determined by parameter  $\beta$ ), the other without; <sup>b</sup> DFT exchange-correlation functional; <sup>c</sup> FHI aims basis-set and integration grid settings with abbreviations l=light, t=tight, and rt=really tight; <sup>d</sup> Mean absolute error. Adapted with permission from Ref. [2]. © 2017 American Chemical Society.

Tab. D.2: Parameter Optimization Results Including Anionic Molecules<sup>a</sup>

| xc <sup>b</sup> | set. <sup>c</sup> | $\varrho_{\text{iso}}$ | $\alpha$               | $\beta$                | MAE <sup>d</sup> | $\varrho_{\text{iso}}$   | $\alpha$              | $\beta$                | MAE <sup>d</sup> |
|-----------------|-------------------|------------------------|------------------------|------------------------|------------------|--------------------------|-----------------------|------------------------|------------------|
|                 |                   | (me Å <sup>-3</sup> )  | (meV Å <sup>-2</sup> ) | (meV Å <sup>-3</sup> ) |                  | (meV)                    | (me Å <sup>-3</sup> ) | (meV Å <sup>-2</sup> ) |                  |
|                 |                   | T2+T3+T4 (386 solutes) |                        |                        |                  | T2+T3c+T4c (386 solutes) |                       |                        |                  |
| PBE             | l                 | 15.1                   | 0.750                  | 0.221                  | 134.5            | 13.6                     | 0.927                 | -0.185                 | 118.2            |
| PBE             | l                 | 15.1                   | 0.943                  | 0                      | 134.2            | 13.6                     | 0.760                 | 0                      | 118.4            |
| PBE             | t                 | 15.6                   | 0.347                  | 0.497                  | 148.3            | 13.9                     | 0.512                 | 0.078                  | 130.4            |
| PBE             | t                 | 15.6                   | 0.778                  | 0                      | 147.7            | 13.9                     | 0.581                 | 0                      | 130.3            |
| PBE             | rt                | 15.6                   | 0.225                  | 0.649                  | 149.1            | 13.9                     | 0.406                 | 0.206                  | 131.1            |
| PBE             | rt                | 15.5                   | 0.773                  | 0                      | 148.1            | 13.9                     | 0.591                 | 0                      | 130.9            |
| RPBE            | t                 | 15.4                   | 0.159                  | 0.659                  | 151.8            | 13.8                     | 0.435                 | 0.137                  | 133.8            |
| RPBE            | t                 | 15.4                   | 0.733                  | 0                      | 150.8            | 13.9                     | 0.556                 | 0                      | 133.7            |
| PBE0            | t                 | 15.4                   | 0.866                  | 0.109                  | 137.2            | 13.8                     | 1.08                  | -0.351                 | 120.1            |
| PBE0            | t                 | 15.4                   | 0.961                  | 0                      | 136.9            | 13.8                     | 0.769                 | 0                      | 120.5            |
| HSE06           | t                 | 15.4                   | 0.861                  | 0.104                  | 137.8            | 13.8                     | 1.05                  | -0.332                 | 120.5            |
| HSE06           | t                 | 15.4                   | 0.952                  | 0                      | 137.6            | 13.8                     | 0.754                 | 0                      | 120.9            |
|                 |                   | T4 (60 solutes)        |                        |                        |                  | T4c (60 solutes)         |                       |                        |                  |
| PBE             | l                 | 64.4                   | 2.89                   | 1.73                   | 161.1            | 45.9                     | 11.02                 | -12.59                 | 132.2            |
| PBE             | l                 | 64.5                   | 4.03                   | 0                      | 161.5            | 31.6                     | 0.323                 | 0                      | 133.9            |
| PBE             | t                 | 73.5                   | -6.05                  | 16.40                  | 172.7            | 48.0                     | 6.82                  | -7.68                  | 137.1            |
| PBE             | t                 | 70.4                   | 3.83                   | 0                      | 181.4            | 39.5                     | 0.450                 | 0                      | 136.6            |
| PBE             | rt                | 72.9                   | -6.20                  | 16.43                  | 172.5            | 48.1                     | 6.77                  | -7.62                  | 137.2            |
| PBE             | rt                | 72.7                   | 4.18                   | 0                      | 181.5            | 36.9                     | 0.117                 | 0                      | 138.1            |
| RPBE            | t                 | 71.8                   | -7.04                  | 17.02                  | 177.9            | 46.7                     | 5.92                  | -6.91                  | 141.2            |
| RPBE            | t                 | 71.8                   | 3.77                   | 0                      | 187.1            | 37.4                     | 0.004                 | 0                      | 141.9            |
| PBE0            | t                 | 67.3                   | -0.547                 | 8.01                   | 160.6            | 44.8                     | 8.84                  | -9.63                  | 127.6            |
| PBE0            | t                 | 67.3                   | 4.63                   | 0                      | 163.7            | 34.1                     | 0.685                 | 0                      | 127.2            |
| HSE06           | t                 | 67.3                   | -0.773                 | 8.25                   | 161.5            | 45.4                     | 9.02                  | -9.87                  | 127.9            |
| HSE06           | t                 | 66.2                   | 4.38                   | 0                      | 164.8            | 33.9                     | 0.592                 | 0                      | 128.0            |

<sup>a</sup> For all computational settings, two parameter sets are given: one with a volume-dependent non-electrostatic contribution (determined by parameter  $\beta$ ), the other without; <sup>b</sup> DFT exchange-correlation functional; <sup>c</sup> FHI aims basis-set and integration grid settings with abbreviations l=light, t=tight, and rt=really tight; <sup>d</sup> Mean absolute error. Adapted with permission from Ref. [2]. © 2017 American Chemical Society.



## ***Appendix Bibliography***

---

- [1] H. B. Schlegel and M. J. Frisch, *Int. J. Quantum Chem.* **54**, 83 (1995) (cit. on p. 106).
- [2] M. Sinstein, C. Scheurer, S. Matera, V. Blum, K. Reuter, and H. Oberhofer, *J. Chem. Theory Comput.* **13**, 5582 (2017) (cit. on pp. 111, 119, 123–125).
- [3] J. Lang, *Adaptive Multilevel Solution of Nonlinear Parabolic PDE Systems*, Vol. 16, Lecture Notes in Computational Science and Engineering (Springer Berlin Heidelberg, 2001) (cit. on p. 117).